POLITECNICO DI MILANO

Dipartimento di Energia

DOCTORAL PROGRAMME IN

ENERGY AND NUCLEAR SCIENCE AND TECHNOLOGY

Functional Properties Control of Doped TiO_2 for Transparent Electrodes and Photoanodes

Doctoral Dissertation of:

Piero Mazzolini

Supervisors:

Prof. Andrea Li Bassi

Prof. Carlo S. Casari

Tutor and Chair of the Doctoral Programme:

Prof. Carlo E. Bottani

Year 2015 – Cycle XXVIII

Abstract

In this thesis a deep investigation on the electrical and optical properties control of Ta-doped TiO_2 (TaTO) thin films is presented, with the aim of shedding light on the open issues concerning this material which has been recently proposed as a novel transparent conducting oxide.

In the field of new generation photovoltaic devices, undoped TiO_2 already plays a major role. In this framework, it is possible to take advantage of its peculiar properties in the form of an high surface area porous layer (photoanode), as well as in a compact morphology (selective layer) for controlling electron separation / transport mechanisms in the device. Nonetheless, the ability to add to the intrinsic transparency of TiO_2 a significant electrical conductivity via extrinsic doping with group V elements, like Nb or Ta, opens the way to its possible implementation as the front transparent conducting electrode in a possibly all TiO_2-based photovoltaic architecture.

Here, TaTO as well as TiO_2 thin films are synthesized by room temperature Pulsed Laser Deposition on glass substrates followed by thermal treatment. The high control level achieved for these processes allows to obtain compact and nanoporous morphologies with the proven ability of finely tuning conductivity and transparency, making this material suitable for several applications. This capability is thoroughly investigated with different experimental techniques, trying to shed light on the relationship between the material structure / morphology and the corresponding functional properties, and on the ruling physical mechanisms. This study can represent an important step further not only for the future implementation of TaTO in novel solar

cell or other optoelectronic devices, but also for a deeper comprehension of the behavior and defect chemistry of TiO_2-based materials.

Sinossi

In questa tesi viene presentata un'indagine approfondita sul controllo delle proprietà elettriche ed ottiche di film sottili di TiO_2 drogato con Ta (TaTO), cercando in particolare di indagare sulle potenzilità di questo materiale recentemente proposto come ossido trasparente conduttore.

Il TiO_2 non drogato è un materiale molto conosciuto ed ampiamente utilizzato nel campo dei dispositivi fotovoltaici di nuova generazione, risultando al giorno d'oggi uno dei componenti fondamentali nell'architettura di molti tipi di celle solari. Questo è dovuto alle proprietà peculiari della titania che possono essere sfruttate per i meccanismi di separazione e trasporto degli elettroni all'interno del dispositivo sia nella forma di uno strato poroso ad alta area superficiale (il cosiddetto fotoanodo), così come in una morfologia compatta (denominato strato selettivo). Tuttavia, è stato recentemente dimostrato come il drogaggio estrinseco del TiO_2 con elementi quali Ta o Nb renda possibile l'ottenimento di una elevata conducibilità elettrica in un materiale altrimenti isolante, aprendo la strada ad un suo possibile utilizzo come elettrodo trasparente e conduttore all'interno di un'innovativa architettura di cella.

Nell'ambito di questo lavoro, film sottili di TaTO e TiO_2 sono stati depositati a temperatura ambiente mediante la tecnica di deposizione a laser pulsato (PLD) su substrati di vetro, ed in seguito trattati termicamente. L'elevato livello di controllo raggiunto sui processi di sintesi del materiale ha reso possibile l'ottenimento di film caratterizzati da una diversa morfologia (compatti e porosi), dimostrando la capacità di poterne controllare in maniera accurata la trasparenza e la conducibilità elettrica, rendendo questo materiale adatto per diverse applicazioni. Inoltre, molteplici tecniche

sperimentali di caratterizzazione sono state utilizzate per cercare di comprendere i meccanismi fisici che regolano il rapporto tra struttura e morfologia del materiale e le sue proprietà funzionali. Questo studio può risultare fondamentale per la futura implementazione del TaTO nelle celle solari di nuova generazione e per una più profonda comprensione della sua chimica dei difetti.

Contents

1. Introduction

The energetic supply and its sustainability are becoming nowadays a major issue. Several energy sources should be considered and exploited in order to fulfill the development of a globally sustainable society; among them, renewable sources should play an increasingly important role in the near future. In particular, big efforts have been made in the photovoltaic field, since it represents one of the energy-conversion technologies with the highest potential due to the possible exploitation of the sun as an almost infinite energetic source. Up to now the market is basically dominated by crystalline Si-based solar cells, while new generation photovoltaic technologies are still trying to emerge [1]. Nevertheless, in the last few years, the discovery of a new branch of solar cells based on organometal perovskite light absorbers are literally conquering the scene in the scientific community because of the exceptional progress rate at which they are being developed [2].

In perovskite-based solar cells (and more in general in the class of dye-sensitized or quantum-dot-sensitized solar cells) the role of interfaces among the different materials constituting the cell is essential in order to achieve an efficient charge carrier separation [3]. Titanium oxide, due to its intrinsic transparency and favorable energy level alignment with respect to the most employed light absorbing materials, represents so far the most efficient electron transporter / hole blocking material for several solar cell architectures [4]; it is establishing a sort of a selective bridge for the electron path between the photoactive material (which generates the hole-electron couple as a photon-absorption response) and the electrode (which finally collects the electrons at the anode). For the working principle of a solar cell device, photons have to reach the

photoactive material; consequently, both TiO_2 and the electrode have to allow the transmission of the largest fraction of the solar spectrum. In addition to a high transparency to visible light, the electrode at the anode side has to be able to combine as well a low electrical resistivity. The technological demand in the photovoltaic field for a material able to conjugate these two properties stimulated the scientific interest in the class of Transparent Conducting Oxides (TCOs).

Semiconducting oxides with a wide band gap (E_g > 3 eV), are usually characterized by a good transmittance to visible light and a poor electrical conductivity. Some of them can obtain a metal-like conductivity via extrinsic doping (e.g. the substitution of a certain amount of metal ions in the crystalline structure), constituting the TCO's family. Nevertheless, as we already pointed out, the combination of transparency and conductivity is not the only requirement for a TCO, since the development of new generation solar cell devices requires an accurate control of the material interfaces throughout the device. Up to now, the most employed TCO in dye sensitized or perovskite-based solar cell devices is fluorine-doped tin oxide (FTO). Nonetheless, it was demonstrated that the FTO – TiO_2 interface at the photoanode can create an energy barrier which could affect the photogenerated electron collection efficiency [5]. In this framework, the recent discovery of donor-doped TiO_2 as a new family of TCOs, can open the way to a better suited interface engineering at the anode side of the device [6]. Moreover, the peculiar properties of donor-doped TiO_2 as a TCO could be potentially highly interesting also in the field of organic light-emitting diodes (OLEDs), as well as blue GaN-based LEDs [7]. Furthermore, the possibility to tune the functional properties of TiO_2 via extrinsic doping together with the ability of obtaining TiO_2 in a highly surface area nanostructured form (e.g. nanoparticles, nanotubes, nanowires, nanotrees), could be of great advantage for several applications like photoanodes for solar cell devices, gas sensing and water splitting processes [8-10].

In this work we try to unveil the full potentialities of Ta-doped TiO_2 (TaTO) particularly aiming on its possible future implementation in new generation solar cell devices. We focus on the obtainment of a fine control of the functional properties of the material and on the understanding of the physical mechanisms ruling the material behavior. We investigate the material not only as a TCO, but we discuss also its potential appealing as a selective layer / nanostructured photoanode for the obtainment

of an all TiO_2-based TCO – selective layer – photoanode to be possibly applied in solid state solar cell devices (e.g. dye sensitized / perovskite-based solar cells).

The thesis work is structured as follows: we first discuss the fundamental properties of doped and undoped TiO_2 for energy related applications (Chapter 2), mainly focusing on its fundamental role in the photovoltaic field. We then discuss the main aspects related to the pulsed laser deposition technique applied to the synthesis of doped oxides thin films in general, and in particular to Ta-doped TiO_2 (Chapter 3). In Chapter 4 we show our experimental results on the functional properties control obtained for TaTO films characterized by a compact as well as a high surface / volume ratio morphology (e.g. tree-like shaped morphology [11]); we present the possibility of combining the two different morphologies in a multiple-layer structured thin film and the possible related advantages for a future implementation in solar cell device. In Chapter 5 we focus on the physical reasons behind the evidenced possibility to control and tune both transmittance and conductivity of TiO_2-based films; the involved point defects are disclosed and discussed based on experimental evidences collected adopting several experimental techniques. In Chapter 6 we show how the understanding of the material behavior and its fundamental aspects provide the possibility of overcoming the limits imposed by a traditional crystallization process (e.g. annealing atmosphere), with an ultra-fast temperature cycle applicable for both doped and undoped TiO_2 thin films.

The experimental work presented in this thesis was personally carried out by the author, with the exception of X-Ray Diffraction (the presented results are based on the collaboration with D. Chrastina, L-NESS, Dipartimento di Fisica, Politecnico di Milano, Italy), Positron Annihilation Spectroscopy (the results presented in Section 5.3 are based on the collaboration with R. O. Ferragut, L-NESS, Dipartimento di Fisica, Politecnico di Milano, Italy) and Secondary Ion Mass Spectroscopy (the results presented in Section 6.3.2 are based on the collaboration with T. Acartürk and U. Starke, Max Planck Institute for Solid State Research, Stuttgart, Germany).

The experimental data of the contactless resistance measurements reported in Section 4.3.3 were collected at the synchrotron light source of Elettra (Sincrotrone Trieste S.C.p.A., Trieste, Italy).

The ultra-fast annealing treatments (discussed in Chapter 6) were performed in a home-made fast annealing furnace designed and built personally by the author in collaboration with U. Klock during the 3 + 2 months spent abroad during the PhD (Max Planck Institute for Solid State Research – department of Physical Chemistry of Solids – Stuttgart, Germany).

The work carried out during the PhD activity had led to the active contribution in the following international conferences:

- FisMat 2013 (Milan, Italy, september 09-13, 2013); title of oral contribution: "Structural, electrical and optical properties of nanostructured Ta-doped TiO_2 produced by PLD"
- MRS Spring Meeting & Exhibit 2014 (San Francisco, California, USA, April 21-25, 2014); title of oral contribution: "Nanostructured Ta-doped TiO_2 as a highly conducting transparent electrode / functional photoanode"
- CIMTEC 2014 - 6^{th} Forum on New Materials (Montecatini Terme, Italy, June 15-20, 2014); title of oral contribution: "Structural, electrical and optical properties of nanostructured Ta-doped TiO_2"
- TCM 2014 – 5th international symposium on transparent conductive materials (Chania, Crete, Greece, 12-17 October); title of oral contribution: "Nanoengineered Ta-doped TiO_2 as a highly conducting transparent electrode / functional photoanode"
- Max Planck Institute, Joachim Maier Department Workshop 2015 (Schloss Ringberg, Rottach-Egern, Germany, January 12-14, 2015); title of oral

contribution: “Tuning structural and functional properties of transparent conducting Ta-doped TiO_2”

- SSI 2015 - 20th International Conference on Solid State Ionics (Keystone, Colorado, USA June 14-19, 2015); title of oral contribution: “Tuning of electrical and optical properties of TiO2-based polycrystalline films”

and to the publication of the following peer-reviewed papers, ordered by year:

- P. Gondoni, P. Mazzolini, A. M. Pillado Pérez, V. Russo, A. Li Bassi, C. S. Casari, “Morphology-driven electrical and optical properties in graded hierarchical transparent conducting Al:ZnO”, *Materials Research Society Symposium Proceedings*, 1699E., in press, 2014, doi:10.1557/opl.2014.424 (*)
- P. Gondoni, P. Mazzolini, V. Russo, A. Petrozza, A. K. Srivastava, A. Li Bassi, C. S. Casari, “Enhancing Light Harvesting by Hierarchical Functionally Graded Transparent Conducting Al-Doped ZnO Nano- and Mesoarchitectures”, *Solar Energy Materials & Solar Cells*, 128, 2014, pp 248–253 (*)
- P. Mazzolini, P. Gondoni, V. Russo, D. Chrastina, C.S. Casari, A. Li Bassi, “Tuning of Electrical and Optical Properties of Highly Conducting and Transparent Ta-Doped TiO_2 Polycrystalline Films”, *The Journal of Physical Chemistry C*, 119, 2015, pp 6988–6997
- P. Gondoni, P. Mazzolini, V. Russo, M. Diani, M. Amati, L. Gregoratti, V. De Renzi, G. Gazzadi, J. Marti-Rujas, C. Casari, A. Li Bassi, “Tuning electrical properties of hierarchically assembled Al-doped ZnO nanoforests by room temperature Pulsed Laser Deposition", *Thin Solid Films*, 594, Part-A, 2015, pp 12-17 (*)
- P. Mazzolini, T. Acartürk, D. Chrastina, U. Starke, C.S. Casari, G. Gregori and A. Li Bassi, “Controlling the Electrical Properties of Undoped and Ta-doped TiO_2 Polycrystalline Films Via Ultra-Fast Annealing Treatments”, *Advanced Electronic Materials*, forthcoming, 2015 (arXiv:1509.02744)
- P. Mazzolini, V. Russo, C.S. Casari, P. Gondoni, S. Nakao, T. Hitosugi, A. Li Bassi “Direct Connection Between Structural/Vibrational and Transport Properties in Transparent Conducting Ta-Doped TiO_2 Films”, in preparation.

(*) The author was also involved on the study of Al-doped ZnO films during the PhD, but the results obtained in this framework are not discussed in this dissertation. For

further details please refer to the PhD thesis of P. Gondoni “Nanostructured transparent conducting oxides for advanced photovoltaic applications”, 2014, Politecnico di Milano.

2. TiO_2 for energy related applications

TiO_2 is an abundant and low cost material which can be found mainly in three different crystalline forms: the stable rutile, and the metastable phases anatase and brookite. Among them, the most important polymorphs for several applications are rutile and anatase [12]; they are both characterized by a tetragonal symmetry, and can be represented by a network of TiO_6 octahedron building blocks (see Figure 1 *(a)* and *(b)* [13]). Both these two crystalline structures are characterized by a wide energy bandgap in the electronic density of states (E_g ~ 3 eV for rutile and E_g ~ 3.2 eV for anatase).

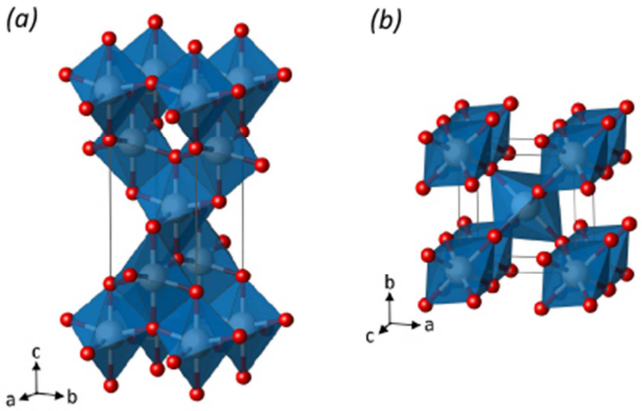

Figure 1 Crystalline structure of TiO_2 anatase *(a)* and rutile *(b)* phase, with evidenced TiO_6-octahedra networks; Ti and O atoms are represented in white and red respectively. Picture reproduced from [13] and modified.

TiO_2 is employed or considered for several energy related applications [14], and usually both anatase and rutile polymorphs are suitable, especially in presence of phase

mixtures [15]. The first energy-related peculiar property of TiO_2 which makes it widely investigated is its high photocatalytic activity which could be exploited in water splitting processes when exposed to UV-light, firstly discovered in 1972 [16]; it is worth to mention that after more than 40 years, TiO_2 still remains one of the most investigated materials as a photocatalyst [17]. Other properties like its high resistance to acids and alkalis coupled with the possibility to obtain TiO_2 in nanostructured form characterized by a large surface area (e.g. nanoparticles, nanotubes and nanotrees [18, 19]) have attracted wide interest also for applications in the fields of lithium ion batteries and fuel cells [20, 21].

Among the above cited energy fields in which this material is employed, one of the most intriguing and studied ones is photovoltaics. TiO_2 forcefully entered in 1991 as a major player in this research field due to the breakthrough discovery made by B. O'Regan and M. Grätzel of a mixed organic – inorganic solar cell device with a 7.1% efficiency, belonging to the class of Dye Sensitized Solar cells (DSSCs) [22]. The working principle of DSSCs is linked to the possibility to obtain an efficient separation between the photogenerated charge carriers (electrons and holes) thanks to a proper engineering of the interfaces among the several materials which constitutes the device [3]. Titanium dioxide represents the perfect material in order to efficiently separate and collect the electrons at the anode size of the cell. Differently from the other applications discussed so far, in DSSCs TiO_2 has to be employed in pure anatase phase; this is because of a higher electron mobility of this crystalline phase with respect to rutile, coupled with a wider bandgap and a better suited energy level position [1]. Because of the wide scientific interest aroused by the discovery of DSSCs, several advancements have been made in the understanding of the physical mechanisms behind its working principles in the following two decades. Nevertheless, the efficiency improvements were not as effective than initially foreseen; this until the rise of the most recent revolution in the photovoltaic field: the discovery of organometal halide perovskites as visible-light sensitizers for photovoltaic cells [23].

2.1 Solar cell devices

In order to fully understand the basic role played by TiO_2 in these solar cell devices, the main physical characteristics and the most important solar cell

configurations in dye sensitized and perovskite-based solar cells are presented. We then particularly focus on one of the key components of these devices, which constitutes a crucial interface with TiO_2 for the electron collection: the transparent conducting electrode.

2.1.1 Dye sensitized solar cells

The general structure (reported Figure 2 *(a)*) and the basic steps involved in the working principle of a DSSC (represented in Figure 2 *(a)*) can be summarized as follows: an organic molecule, called dye, is actively converting the energy of the incoming incident light in the formation of electron-hole couples (step 1). In the solar cell architecture, the dye molecules are adsorbed at the surface of nanocrystalline TiO_2 sintered particles (the photoanode); the intimate contact between them and the proper TiO_2 conduction band position are ensuring the possibility to sensitize the photoanode, i.e. to efficiently extract the photogenerated electrons (step 2). The extracted electrons are then collected by the electrode (step 4), which is constituted by a thin film of a Transparent Conducting Oxide (TCO, usually F-doped tin oxide – FTO). Being transparent to the visible region of the solar spectrum because of their wide bandgap, both the anatase particles and the TCO are ensuring the biggest part of the incoming radiation to reach and be converted by the dye. On the cathode side of the cell a liquid electrolyte (usually containing a I_3^-/I^- redox couple) is acting as a redox shuttle between the oxidized dye (which is regenerated via the photogenerated hole transfer, step 3) and the metallic counter electrode (which is reducing the electrolyte, step 6). It is important to mention that the dye regeneration itself in the case of I_3^-/I^- redox couple is a two-step process which involves the formation of an intermediate product (I_2^-); this is strongly decreasing the possibility to have hole-recombination processes which could mainly occur at the interface with the transparent electrode due to the large amount of free electrons populating the conduction band of the TCO [24].

A crucial point for these device is related to the stability in time; this issue mainly drove the necessity to shift from a liquid electrolyte to an all solid-state DSSC. Here the hole transfer occurs from the dye to a solid – organic layer (usually the spiro-MeOTAD) which has to be infiltrated inside the TiO_2 pores in order to obtain an intimate contact with the dye [25].

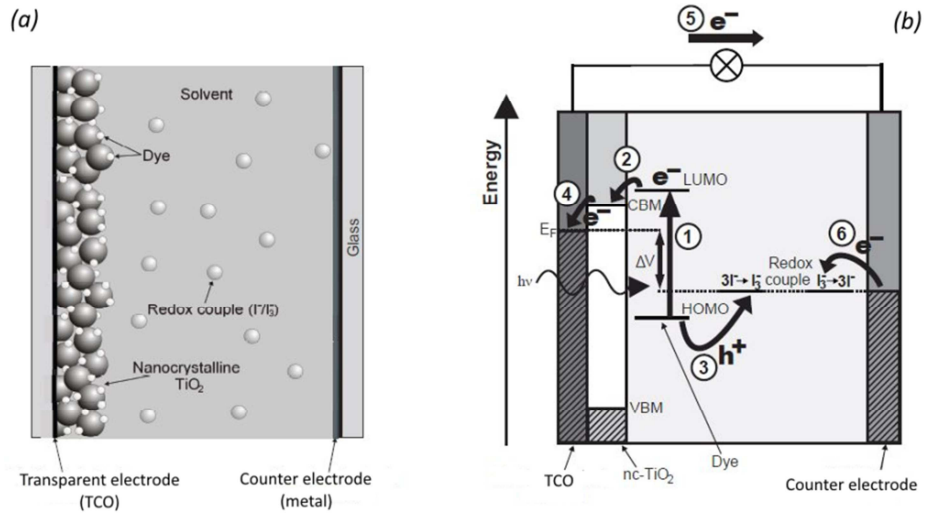

Figure 2 Structure of a liquid electrolyte DSSC *(a)*; in *(b)* a schematic representation of the basic steps for the device functioning are reported. Picture reproduced from [24] and modified.

Nevertheless, the charge separation / collection in these devices is an efficient process because of the accurate choice of the materials and of the interfaces among them; these are ruling the kinetics of the electron hole separation (i.e. the typical transfer – recombination times associated to the charge transfer steps presented above) [26]. The employment of a hole transport material (HTM) results in a single-step electron-hole recombination mechanism, considerably faster with respect to the double-step recombination process of the I_3^-/I^- liquid electrolyte. It became thus fundamental for the device performances the utilization in the cell architecture of a compact TiO_2 layer beneath the nanoporous TiO_2 photoanode in order to avoid an intimate contact between the HTM and the TCO: the so called electron selective layer / hole blocking layer [25]. Despite the big achievements in the know-how of the DSSC working principles, the most stable solid state architecture just reached a record efficiency of 7.2% in 2011 [27] (basically the same value reached by the first high efficiency DSSC with liquid electrolyte which opened up the research in this field in 1991 [22]).

2.1.2 Perovskite-based solar cells

The real breakthrough discovery in solid state DSSC came in 2012, with a solar cell with a perovskite light absorber with an overall efficiency next to 10% [28]. As it is possible to appreciate from Figure 3, the only change in the device configuration was the substitution of the dye with a lead halide perovskite as a light absorber material.

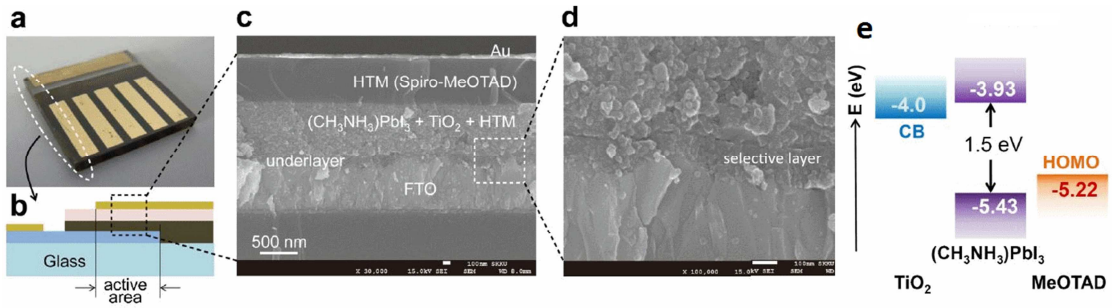

Figure 3 Solid-state device and its cross-sectional meso-structure; (a) real solid-state device; (b) cross-sectional structure; (c) cross-section SEM image; (d) selective layer (compact TiO_2) – FTO interface magnification; (e) schematic energy level diagram of TiO_2, $(CH_3NH_3)PbI_3$, and spiro-MeOTAD. Modified picture from [28].

This was just the starting point of a steep increase in the power conversion efficiency of the perovskite-based solar cells, which up to know already broke the limit of 20% in less than 3 years of scientific research, and is thus becoming a serious competitor of Si-based solar cells for the next future [29]. The physical reasons behind these advancements are related to several peculiar properties of this new light absorber, like its excellent light harvesting performances, the favorable match of conduction and valence band with hole and electron transport materials (spiro-MeOTAD and TiO_2 respectively) and an unusually large exciton diffusion length coupled with a high mobility of the charge carriers [30]. Among them, the possibility to add to an efficient exciton generation the ability to transport the photogenerated charges before their effective separation gave rise to the ability of obtaining several new solar cell configurations [31]. The most important architectures are reported in Figure 4.

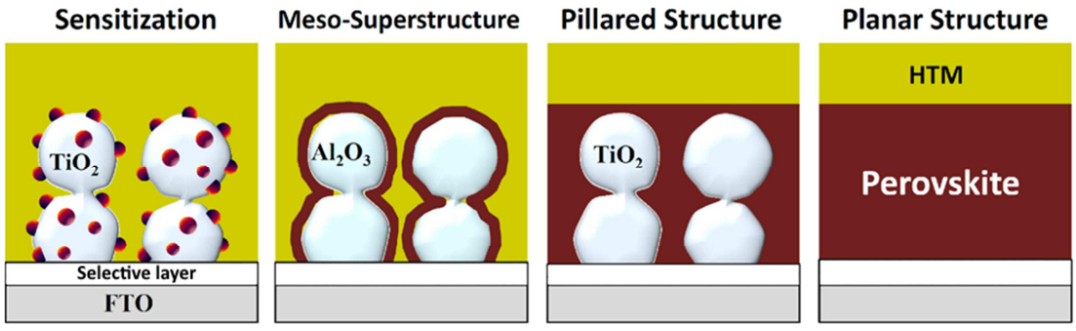

Figure 4 Comparison of different perovskite-based solar cell architectures. Modified picture from [32].

In particular, it is worth to mention that thanks to the above discussed peculiar properties of perovskites, it is possible to obtain solar cell architectures without the

employment of sensitized TiO_2 nanoparticles [33], resulting in the possibility to achieve an efficient planar structure (*p*/*n* junction). However, what is still always needed in all of these configurations is the presence of a compact TiO_2 electron selective layer on top of the TCO in order to reduce the recombination rate and so to obtain an efficient electron collection.

2.1.3 *TCO – TiO_2 interface*

As already pointed out, the presence of a compact TiO_2 layer on top of the transparent electrode at the anode side is essential in order to preserve the device efficiency. Nevertheless, the choice of the TCO is limited by the process temperature needed to synthesize and/or crystallize TiO_2. The deposition of the compact TiO_2 selective layer is made on top of the TCO by aerosol spray pyrolysis using oxygen as a carrier gas at a temperature of 450-500 °C, or by spin coating followed by a post annealing treatment performed in air at 500 °C [28, 33]. If the device configuration includes the employment of a mesoporous TiO_2 photoanode on top of the already crystallized selective layer, the process usually requires the spin coating or the doctor blade application of a nanoparticle-sized paste followed again by a heating treatment performed in air in which the temperature is gradually raised up to 500-550 °C [34]. The overall time needed to complete these temperature cycles is in general in the order of hours. The need to reach (and to maintain) TiO_2 at high temperatures in presence of oxygen is an extremely demanding condition for a *n*-type TCO. As a matter of fact, up to now FTO is the only TCO which is not severely affected by such temperature cycles in presence of oxygen [26]. FTO is one of the most important TCOs not only for its ability to tolerate oxygen at high temperatures, but also for its low resistivity (in the order of 10^{-4} Ωcm) and transmittance to the visible region (T_{VIS} exceeding 80%) which are basically comparable to the ones of the most famous indium-tin oxide (ITO) [35].

Nevertheless, the excellent functional properties of FTO are not a sufficient condition for the device, since the interface with TiO_2 has to be carefully considered as well. When a TCO is brought to contact with an organic or inorganic semiconductor, the coupling between the work functions of the two materials could result in the formation of an energy barrier for the electron transfer at the electrode interface [36, 37].

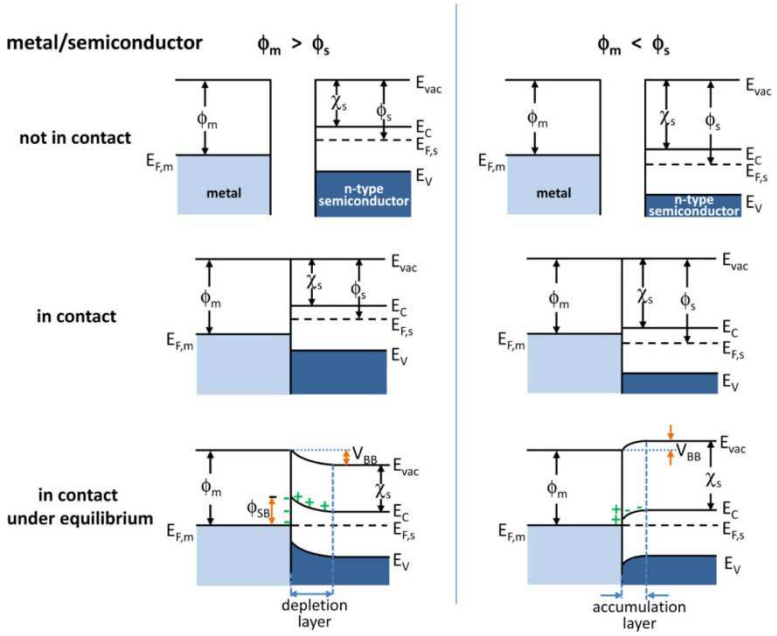

Figure 5 Energy band diagrams of metal and n-type semiconductor contacts. $\boldsymbol{E_{F,m}}$, Fermi level of the metal; $\boldsymbol{E_{vac}}$, vacuum energy; $\boldsymbol{E_C}$, energy of conduction band minimum; $\boldsymbol{E_V}$, energy of valence band maximum; $\boldsymbol{\phi_m}$, metal work function; $\boldsymbol{\phi_s}$, semiconductor work function; $\boldsymbol{\chi_s}$, electron affinity of the semiconductor. Picture reproduced from [38].

Being a TCO a degenerate semiconductor, *i.e.* the Fermi level E_F is laying above the conduction band, it can be considered as a metal: its work function ϕ_m is defined as the energy difference between the $E_{F,m}$ and the vacuum level E_{vac} (Figure 5). If a metal is brought in contact with a semiconductor with a lower work function ($\phi_m > \phi_s$), the electrons in the semiconductor conduction band can lower their energy by flowing into the metal, which leads to a depletion layer near this interface. Such a layer constitutes an energy barrier (Schottky barrier) for the electrons injection from the semiconductor [39]. Although we are not facing this aspect, it should be mentioned that together with the coupling of the work functions, the height and width of the energy barrier could be affected by the presence of surface states at the semiconductor-metal interface [38]. When the metal-semiconductor interface is considered inside a solar cell device, the presence of a Schottky energy barrier has to be carefully considered not only at thermal equilibrium (*i.e.* pure device interface in dark conditions), but also when the cell is illuminated: in such a condition, for the working principle already explained in this chapter, the photogenerated electrons are injected in TiO_2 (in both selective layer and photoanode if present). This causes the formation of a quasi-Fermi level E_{Fn} next to the conduction band level E_C, i.e. the intrinsic E_F is "pumped up" by the electron injection.

Consequently, the electron collection efficiency at the anode side could be affected by an energy barrier at the interface semiconductor-TCO which should become more severe as the illumination intensity is increased [5]. Nevertheless, it should be pointed out that it is difficult to give an exact and absolute value of the energy levels (*i.e.* work function, electron affinity) of a material, since they are known to be strictly related to synthesis, annealing and working conditions [36].

Because of the almost forced choice of FTO and TiO_2 as anode materials in several solar cell devices, the presence of an energy barrier at this interface has already been discussed in some works [40, 41]. In 2006 H. J. Snaith and M. Grätzel [5] demonstrated the presence of a Schottky barrier for the electron collection at the compact TiO_2 (selective layer) – FTO interface in solid state DSSCs; this barrier was able to affect even severely the efficiency of the devices. It was shown how it could be possible to limit the detrimental effect of this energetic barrier by lowering the concentration of the *n*-type defects in TiO_2 (the oxygen vacancies), i.e tuning its E_F level. However, the most efficient approach would be to choose a better matched electrode material.

Nevertheless, up to now this implies the necessity to find another highly performing TCO able to resist at high temperatures in presence of oxygen, or to drastically decrease the temperature needed to synthesize the TiO_2 layers in the cell. Recently a lot of efforts have been made towards an overall reduction of the temperatures needed in the realization of the solar cell devices, and thus the ability to obtain TiO_2 layers in a less demanding temperature cycle is widely investigated. J. T. W. Wang *et al.* [42] demonstrated the possibility of reducing the temperature down to 150 °C for a graphene-TiO_2 composite selective layer synthesized on top of the FTO electrode. Surprisingly, the effect of this composite material leads to a superior charge collection in the tested perovskite-based devices; it was proposed that as graphene should have a work function between that of FTO and TiO_2, it may reduce the energy barrier which was shown to be present at the material interface [5, 42].

Moreover, in 2014 Zhou *et al.* reported in a Science paper [43] the possibility to increase the device efficiency of a planar structured perovskite-based solar cell up to 19.3% (device architecture reported in Figure 6 (a)). This surprisingly high value was achieved via a fine control of the energy levels alignment throughout the device interfaces. In particular the ability to synthesize an Yttrium-doped TiO_2 selective layer

(in order to increase its overall conductivity with respect to the undoped material) at low temperature (150 °C) gave the possibility to substitute the electrode material; in this case ITO was used as a transparent electrode in place of FTO. In order to better match the work function of the TCO with respect to the selective layer (energy levels of the functional layers reported in Figure 6 (b)), an ultrathin polyethyleneimine ethoxylated (PEIE) layer was physisorbed on the ITO surface. The obtainment of an electrode work function near (or even lower) to the one of the selective layer (together with its increased conductivity given by Y-doping) was considered the reason of the extremely high device efficiency obtained.

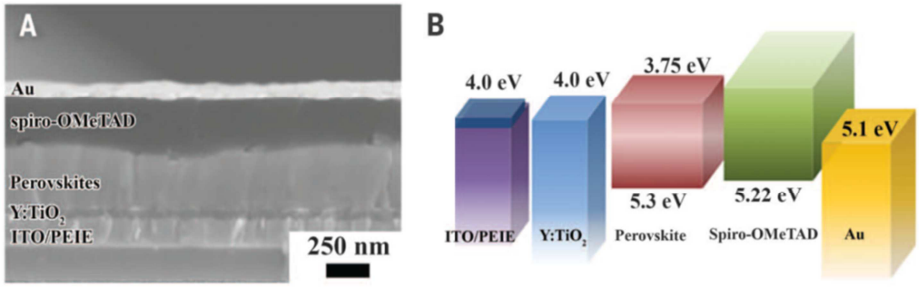

Figure 6 (a) SEM cross-sectional image of the device. (b) Diagram of energy levels (relative to the vacuum level) of the functional layers of the device (prior to contact). The work functions of each layer were determined with UV photoelectron spectroscopy (UPS). Pictures taken from [43].

2.2 Transparent Conducting Oxides

In the above discussion concerning novel solar cell devices we have already mentioned two of the most performing *n*-type TCOs: ITO and FTO. Between them, indium-tin oxide is definitely the most widely employed one. Nevertheless, due to the increasing demand of this material (especially in the field of flat panel displays) and the high price of In, a lot of effort has been made to find its substitution [44]. Several materials have been investigated, and among them fluorine-doped tin oxide (FTO) and aluminum-doped zinc oxide (AZO) emerged as suitable candidates. We already reported about the temperature stability of FTO, which makes it an almost unique TCO for particular applications, like for example the solar cell devices described in Section 2.1.1 and 2.1.2. On the other hand, a big effort is made in order to obtain flexible electronic devices with new functional properties not intrinsically present in common compact TCO films. From this point of view AZO is one of the most studied materials

because of the possibility to obtain highly conducting and transparent thin films even for room temperature synthesis conditions [45]. Moreover, it has been shown how it is possible to highly control the light scattering properties of AZO [46], making it highly appealing for the fabrication of all organic solar cell devices [47].

Nevertheless, what recently resulted as the new big thing in the TCO's field, with an almost immediate industrial application, is again based on the employment of indium: the amorphous TCOs, firstly discovered in 1996 by H. Hosono *et al.* [48]. As a matter of fact, the development of this new class of TCOs which are based on the overlap of the *ns* orbitals even if the short range order is broken, evidenced the superior performances of the amorphous system In-Ga-Zn-O (a-IGZO) [49, 50].

All the above mentioned materials are *n*-type TCOs. Although the ability to obtain a *p*-type TCOs could be very appealing especially for the possibility to create transparent *p*/*n* junctions, up to now no valuable materials able to fulfill the desired functional properties have been obtained yet and a suitable candidate has still to be found [51]. In the next section the fundamental properties of the TCOs will be presented, focusing on the class of the *n*-type doped oxides.

2.2.1 Fundamental properties of TCOs

The starting point for having a transparent oxide is the bandgap, which should be higher than 3 eV, i.e. sufficiently large to avoid visible light absorption. On the other hand, a proper amount of extrinsic and intrinsic doping should provide a sufficient charge carrier concentration to make it conductive (i.e. degenerate semiconductor). Nevertheless, it is not trivial to combine these two requirements; as a matter of fact, because of their wide bandgap and large amount of charge carriers required for being conductive, the optical and electrical properties of TCOs are tightly bonded together.

From a physical point of view, the conductivity σ of a material is ruled by:

$$\sigma = en\mu$$

where e is the elementary charge, n the carrier concentration and μ their mobility [39]. There are two possible ways to increment the charge carrier concentration of a wide bandgap oxide. The first one involves the ability to promote the formation of "free carriers" starting from the basic compound, i.e. an intrinsic doping; the most common case for oxides is the control of the oxygen stoichiometry, although the formation of oxygen vacancies itself is not always directly involved in the promotion of conduction

electrons in the conduction band [52]. Nevertheless, in order to obtain the low resistivity values required for a practical application of a TCO ($\rho \sim 10^{-3} - 10^{-4}$ Ωcm), the intrinsic doping alone is not enough; a certain amount (usually in the order of a few at. %) of metal ions should be substituted with aliovalent ions which could effectively act as electron donors for the considered compound [53]. This results in the partial filling of the lowest conduction band with electrons (usually in the order of $n \sim 10^{20} - 10^{21}$ cm^{-3}).

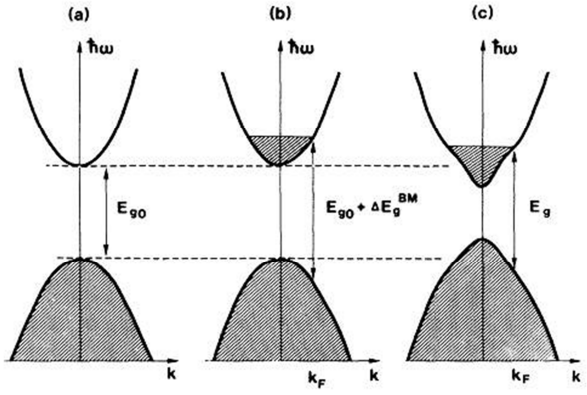

Figure 7 (a) Band structure representation of a direct gap semiconductor with parabolic bands separated by $\boldsymbol{E_{g0}}$. (b) Doping-induced (n-type) increase of the optical gap by an energy amount $\boldsymbol{\Delta E_g^M}$. (c) Perturbed band structure and resulting optical gap $\boldsymbol{E_g}$ as a consequence of many-body effects. Shaded areas denote occupied states, $\boldsymbol{k_F}$ represents the Fermi wave vector. Picture taken from [54].

As a direct result of the Pauli Exclusion principle, the occupation of band-edge states forces higher-energy optical transitions with respect to the original bandgap of the oxide E_{g0} (see Figure 7 (a) and (b) for undoped and donor-doped compound respectively). The carrier-induced shift ΔE_G is called Moss-Burstein effect [55], and in the case of a simplified Drude model it can be described according to:

$$\Delta E_G = {\hbar^2}/{2m^*}\,(3\pi^2 n)^{2/3}$$

where n is the electron density, $\hbar$ is the reduced Planck constant and m^* is the reduced effective mass (defined as the reciprocal of the inverse sum of the effective masses of the hole and the electron, *i.e.* $m^{*(-1)} = m_e^{*(-1)} + m_h^{*(-1)}$). According to the presented equation, a high doping level results in an increased transparency in the UV region due to increased optical bandgap (represented in Figure 7 (a) and (b)). Nevertheless, this has to be considered as a qualitative description, since the effect of the nonparabolicity of the bands (represented in Figure 7 (c)), which could be induced by many-body type interactions, is not considered in the model [54, 56, 57].

Up to this point, the possibility to obtain an increased transmittance of the material as a function of the increased charge carrier density of the degenerately doped material could suggest to maximize *n*. However, other two factors are strictly interconnected with the presence of a highly populated conduction band: the first one is the transmittance at high wavelengths and the second one is the charge carrier mobility. If the bottom of the conduction band is partially filled with carriers, they can be considered as a free electron gas (Drude model), which can absorb electromagnetic radiation to sustain collective plasma oscillations at its resonance frequency. This is the plasma wavelength λ_p, which can be evaluated as [58]:

$$\lambda_p = 2\pi c \left(\frac{\varepsilon_0 \varepsilon_\infty m^*}{n_e e^2}\right)^{1/2}$$

where ε_0, ε_∞, c, m^*, and e denote the dielectric constant of vacuum, the high-frequency permittivity, the speed of light, the effective mass, and the electronic charge, respectively. A direct consequence is that for the most part of the TCOs (which are characterized by a m^* in the order of $0.1m_0$, where m_0 is the rest mass of the electron), n has to be limited to a value below 10^{21} cm^{-3} in order to avoid a sensible absorption by the electrons populating the conduction band in the near-IR / visible part of the solar spectrum [7]. This requirement is even more strict in the case of the solar cell application of TCOs, where a high transmittance for a wide region of wavelengths is a preferred property [35].

However, if a sufficiently high electron effective mass is desired for a TCO in order to tolerate the presence of an higher concentration of free electrons in the conduction band without strongly affecting its transmittance, on the other hand a high m^* would be detrimental for the charge carrier mobility. For degenerately doped semiconductors, the mobility in presence of a large amount of ionized impurities μ_{ii} (i.e. the substitutional doping elements) should obey to the following equation [35]:

$$\mu_{ii} = \frac{3(\varepsilon_0 \varepsilon_\infty)^2 h^3}{Z^2 m^{*2} e^3} \frac{n}{N_i} \frac{1}{F_{ii}^{np}(\xi_d)}$$

where h is the Planck's constant, N_i is the dopant concentration, Z is its charge state (usually +1), $\xi_d = (3\pi^2)^{1/3} \varepsilon_0 \varepsilon_\infty h^2 n^{1/3} / m^* e^2$ is the screening parameter and F_{ii}^{np} is the screening function for ionized impurity scattering for a non-parabolic conduction band. Moreover, it is worth mentioning that a too large dopant concentration (N_i) would

become detrimental for the electron mobility due to the scattering induced by ionized impurities.

Up to now, we have just considered the effect of extrinsic defects on the electrical and optical properties of TCOs, evidencing the strong interplay between them; but the effect of intrinsic defects should be considered as well. For instance, we just mention the possible role played by oxygen vacancies in several binary compounds: in this case, inter-bandgap states can be formed, leading to available optical transitions which can decrease the overall transparency of the TCO [59, 60].

Presenting the main aspects which are ruling the functional properties of the TCOs, the effect of grain boundaries was not considered. Nevertheless, it should be mentioned here that the study of polycrystalline films could be more complicated (e.g. grain boundary scattering); some of these aspects will be discussed during the presentation of the results as a choice of clarity.

2.3 Donor doped TiO_2: a new class of TCOs

At the beginning of this chapter we have already presented the superior properties of TiO_2 for photovoltaic applications, discussing its key role played in solar cell devices. Nevertheless, being a wide bandgap semiconductor, TiO_2 is not intrinsically conducting due to the reduced amount of charge carriers in the conduction band. In 2005 it was discovered by the research group of T. Hitosugi [6, 61] how it is possible to combine to its intrinsic good transparency in the visible range a high conductivity, via substitution of a certain amount of Ti atoms with group V elements such as niobium or tantalum in the anatase cell. In particular, in these works it has been shown how it is possible to obtain resistivity values in the order of 2×10^{-4} Ωcm for epitaxially grown thin films.

This discovery sparked the interest on a new and never considered application field for TiO_2: the one of TCOs. In order to understand the potentialities of this new class of d-electron-based TCOs, we here first mention the state of the art regarding the synthesis of the material; we then discuss the defect chemistry which is ruling the functional properties of doped TiO_2 and finally present a comparison between the two most important TiO_2 donor elements (Nb and Ta) which could be employed in order to dope the material.

2.3.1 *Synthesis of transparent conducting TiO_2-based thin films*

Anatase TiO_2 thin films have been fabricated by several techniques, like Pulsed Laser Deposition (PLD), Molecular Beam Epitaxy (MBE), sputtering, Chemical Vapor Deposition (CVD), sol-gel and spry pyrolysis [62-67]. Nevertheless, the achievement of a high conductivity via doping (e.g. Ti substitution with Nb and Ta) suitable for TCO applications has been reported so far just with PLD and sputtering technique.

The first articles reporting on TiO_2 as a TCO, were based on Nb- and Ta-doping (TNO and TaTO) obtained in epitaxially grown thin films via PLD on single crystals of $SrTiO_3$ (001) and $LaAlO_3$ (001) substrates [6, 61]. In Figure 8 the electrical properties obtainable with several Nb and Ta doping concentrations are reported. It is possible to note that the lowest resistivity at room temperature (for both TNO and TaTO $\rho_{min} \sim 2 \times 10^{-4}$ Ωcm) is obtained for a similar doping amount (6 at. % for NTO, 5 at. % for TaTO, Figure 8 (a) and (b) respectively).

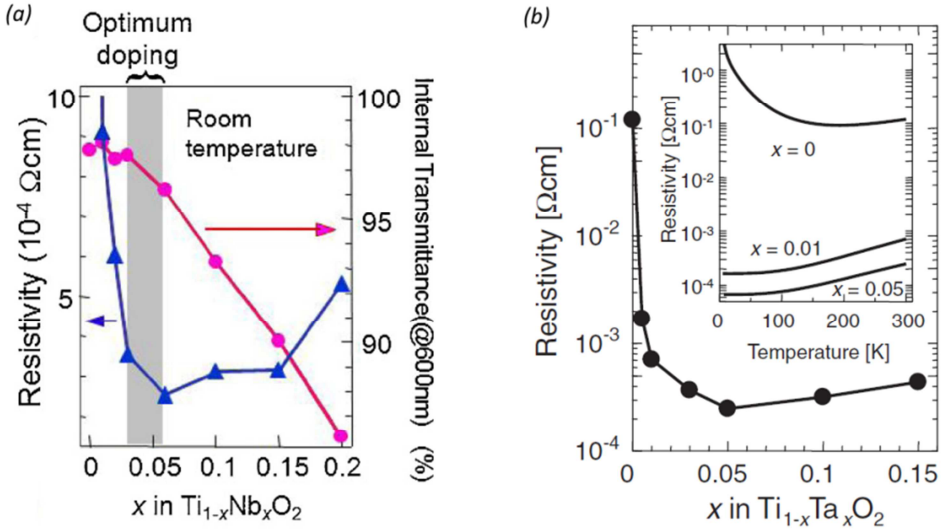

Figure 8 (a) Room temperature resistivity and internal transmittance of Nb-doped TiO_2 as a function of several doping concentrations for epitaxially grown thin films on $SrTiO_3$ (001) substrates; (b) room temperature resistivity of Ta-doped TiO_2 as a function of several doping concentrations for epitaxially grown thin films on $SrTiO_3$ (001) and $LaAlO_3$ (001) substrates; in the inset the resistivity vs temperature is reported for three different compositions; (a) and (b) pictures were taken from references [7] and [61] respectively.

The extremely low electrical resistivity achievable by these optimally-doped TiO_2 (001)-oriented films was shown to be coupled with an excellent (> 90%) internal

transmittance* to the visible light. These functional properties, comparable with the top class TCOs like ITO and FTO, are obtained for a laser ablation of mixed oxides targets ($Ta/Nb_2O_5 – TiO_2$) in low oxygen partial pressure ($p_{O2} = 1.3 \times 10^{-3}$ Pa) with a substrate temperature T_s of ~ 550 °C so to promote the direct formation of the anatase phase. High conductivity values for both TNO and TaTO were obtained as well in a single-step process with radio-frequency sputtering technique on heated $SrTiO_3$ substrates (T_s ~ 400 °C) [68].

Nevertheless, the possible future application in real devices (e.g. solar cells) of this new class of TCOs is strictly related to the ability to obtain doped TiO_2 films with comparable functional properties on inexpensive substrates, like glass. This generally implies the obtainment of a randomly-oriented polycrystalline film. It has been demonstrated that it is possible to obtain highly conducting TNO films on glass substrates via both PLD and sputtering technique [69-77], while TaTO has been considerably less studied [78, 79]. To the best of our knowledge, the lowest resistivity values at room temperature obtained so far for polycrystalline TNO and TaTO thin films are 4.6×10^{-4} Ωcm and 8.7×10^{-4} Ωcm respectively [70, 79]. However, in order to obtain highly conductive polycrystalline TiO_2-based TCOs it is necessary to use a two-step approach, which involves the deposition of amorphous films (e.g. by PLD or sputtering usually at room temperature in presence of low p_{O2}) followed by an *ex-situ* annealing process in a reducing atmosphere (vacuum or H_2-based, commonly at temperatures between 500 °C and 600 °C) so as to induce crystallization to a pure anatase phase and thus increase the carrier mobility, without compromising the charge carrier density. In this context, it is noteworthy that annealing processes in oxidizing atmospheres (e.g. air) result in highly insulating films [7].

2.3.2 Defect chemistry of TiO_2: intrinsic and extrinsic doping

Bulk TiO_2 in both the anatase and rutile crystalline form is usually considered as an intrinsically *n*-type semiconductor. This is related to the likely obtainment under usual synthesis conditions of a stoichiometry deviation which results in a non-intentional shallow doping [80]. Nonetheless, it is possible to significantly vary and control the conductivity of this material as a function of the adopted synthesis

* Defined as the transmittance of the thin film without considering reflection losses

conditions (e.g. oxygen partial pressure). The research area which aims at the identification of the point defects involved in the modification of the electrical properties of compounds as a function of several synthesis conditions constitutes the branch of the defect chemistry.

Intrinsic doping: titanium dioxide can result in the non-obvious presence of a metal-like conductivity at room temperature; nevertheless, this can be obtained just for the anatase crystalline phase. H. Tang *et al.* firstly reported on the different electrical behavior of nominally extrinsically undoped TiO_2 anatase and rutile thin films [81]. As it is possible to see from Figure 9, the thin films treated in an annealing cycle performed in reducing atmosphere both show a decrease of the electrical resistivity. Nevertheless, vacuum annealed anatase films results in a transition to a metallic-state with a sensibly higher *n*-type conductivity with respect to rutile, which preserves a semiconducting character.

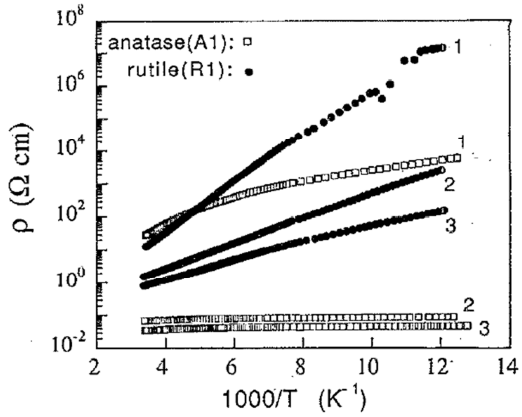

Figure 9 Resistivity vs 1000/T, measured on sputtering deposited anatase (A – 300 °C < substrate T < 400 °C) and rutile (R – substrate T > 400 °C) films: (1) as deposited; (2) vacuum (1.3×10^{-5} Pa) annealed at 400 °C for 2 h; (3) vacuum annealed at 450 °C for 2 h. Graph taken from [81].

The decreased resistivity in presence of reducing conditions (low oxygen partial pressure - p_{O2}) at high temperatures is an experimentally predicted behavior[†] for the defect chemistry of TiO_2 for both anatase and rutile due to the predominant concentration of positive charged defects like oxygen vacancies and/or titanium interstitials which are formed in this regime (since the electroneutrality in the crystal should be fulfilled by $n = 2[V_O^{\bullet\bullet}]$ or $n = 4[Ti_i^{\bullet\bullet\bullet\bullet}]$, where the charged defects are

[†] Considering the conductivity dependency with the oxygen partial pressure at a fixed temperature $\sigma \propto (p_{O2})^m$, where the coefficient *m* reveals the majority defect ruling the conduction mechanism based on thermodynamic equilibrium considerations.

represented according to the Kröger-Vink notation[‡] [82]) [83-85]. Nevertheless, only anatase exhibits a metallic conductivity at room temperature after the annealing cycle (see Figure 9). This substantially different conducting behavior at room temperature is still debated, and several theoretical works are considering the role of the oxygen stoichiometry as the key parameter in determining TiO_2 functional properties [86-88]. In particular, based on Density Functional Theory (DFT) P. Deák *et al.* found that in reduced anatase samples the V_O should be the dominant defect, being shallow enough to result in the formation of delocalized electrons in the conduction band at room temperature, while in the rutile structure the electrons remain localized and should be thermally released (i.e. resulting in the different conduction mechanism at room temperature) [87].

On the other hand, if an oxygen-rich atmosphere is considered (high p_{O2}), the defect chemistry of TiO_2 should be governed by the formation of *p*-type defects (e.g. $p = 4[V_{Ti}''''']$ or $p = 2[O_i'']$). In this case the electronic conductivity of both the crystal phases should drastically decrease, and in the case of anatase it has been recently experimentally demonstrated the possibility to switch to a *p*-type conductivity [89].

Extrinsic doping: in the case of donor-doped TiO_2 (only the group-V elements Nb or Ta will be considered), the aliovalent atom is experimentally found to substitute Ti in both anatase and rutile cells [90]; based on electronautrality conditions, this should result in the release of an electron:

$$D_2O_5 + 2Ti_{Ti}^{\times} \rightleftharpoons 2D_{Ti}^{\bullet} + 2e' + 2TiO_2 + 1/2\, O_2(g)$$

where *D* is indicating the donor element (i.e. Nb or Ta). Typically, in this case the oxygen vacancy as well as the hole concentration are deeply decreased compared to the undoped case and the electroneutrality condition is modified, particularly at intermediate p_{O2} ($n = [D_{Ti}^{\bullet}]$) and under oxidizing conditions ($[D_{Ti}^{\bullet}] = 4[V_{Ti}''''']$ or $2[O_i'']$) [83, 91]. Nevertheless, also in the case of Nb- or Ta-doped TiO_2 a substantial difference in the conduction mechanism at room temperature has been reported as a function of the crystalline structure: as in the case of intrinsically doped titanium oxide, while anatase shows a metallic behavior, rutile is semiconducting [92]. Resonant photoemission

[‡] M_S^C, where *M* corresponds to the species (atoms - e.g. Ti, vacancies - V, electrons or holes - *e* or *h*), *S* corresponds to the lattice site occupied by *M* (e.g. substitutional in a lattice site, or in an interstitial site - *i*), and *C* corresponds to the electronic charge of the species relative to the site that it occupies, where • represent a resultant positive charge, while ′ represents a negative charge.

spectroscopy on donor-doped TiO_2 samples obtained/treated in reducing atmosphere does not show the presence of defect states within the bandgap and the Fermi level is located above the conduction band in the case of anatase [93]; in contrast for rutile the defect states appear within the bandgap [94]. Consistently, theoretical works based on DFT calculations found that donor-doped anatase is metallic while rutile is a semiconductor due to the presence of electron self-trapping sites (i.e. localized electrons) [95, 96].

Although the different conducting behavior upon doping between these two TiO_2 crystalline structures has been explained, there is still an open question in the electrical properties of extrinsically doped anatase; as discussed in section 2.3.1, the presence of a reducing atmosphere (in both direct epitaxial, or two-step polycrystalline growth) is a necessary condition in order to obtain TiO_2-based TCOs. Nevertheless, in the case of a large amount of extrinsic doping, the high doping level should in principle pin the electron concentration over a broad range of oxygen partial pressure (e.g. for a doping amount of 5 at.%, $n \sim 1.4 \times 10^{21}$ cm^{-3} under the hypothesis of 100% donor atoms replacing Ti - $D_{Ti}^{\bullet}$) making the exposure to rather oxidizing conditions less problematic in terms of conductivity. One possible explanation to the oxygen-related loss of conductivity suggested by Huy et al. [97] is that the solubility of the donor element in the anatase lattice is reduced in oxygen-rich conditions, leading to the formation of the non-doping D_2O_5 phase. However, O-rich conditions are expected to reduce only slightly the doping element solubility (i.e. the concentration of $D_{Ti}^{\bullet}$ defects) [78, 98, 99]. For this reason, the obtainment of insulating TNO and TaTO thin films in presence of a non-reducing atmosphere still represents an open point in the understanding of this new class of TCOs.

Finally, it should be noticed that the cited theoretical and experimental works which are trying to explain the physical mechanisms behind the conducting behaviour of these oxides are based on the requirement of a system at a thermodynamic equilibrium and the possible interaction/association of different defects is not considered (e.g. clustering / interplay of different point defects).

2.3.3 Comparison between Nb and Ta doping

In optimally doped TNO and TaTO TCOs it has been shown that the high charge carrier density obtainable for epitaxially grown (001)-oriented thin films is related to the

extremely high doping efficiency (experimentally estimated $n \sim 1.4 – 1.6 \times 10^{21}$ cm^{-3} for a 5 – 6 at.% doping, corresponding to an electron release efficiency η_e > 90% in both Ta- and Nb-doped systems based on $n = [D_{Ti}^{\bullet}]$) [6, 61]. On the other hand the electron mobility is approaching in both cases the value of $\mu \sim 20$ $cm^2V^{-1}s^{-1}$. The overall resistivity of randomly oriented polycrystalline TiO_2-based TCOs is found to increase significantly with respect to the epitaxially grown ones; in the case of Nb substitutionals, which is largely the most investigated doping element for TiO_2, the resistivity value is shown to be at least doubled in the case of polycrystalline films (from $\rho_{min} \sim 2 \times 10^{-4}$ Ωcm for the epitaxially grown film, to $\rho_{min} \sim 5 \times 10^{-4}$ Ωcm for the randomly oriented one). Both the epitaxial and polycrystalline TCOs are characterized by a metallic behavior ($d\rho/dT > 0$, see inset in Figure 8 *(b)*), showing a constant value of the charge carrier density as a function of *T* (i.e. degenerate semiconductor); consequently the conductivity (i.e. mobility) results to be dominated by phonon scattering [7]. While the charge carrier concentration is not found to be significantly affected by the presence of grain boundaries (η_e still in the order of 90% [7]), the polycrystalline system shows a severe reduction of the electron mobility (μ_{max} = 8.0 $cm^2V^{-1}s^{-1}$ for a randomly oriented polycrystalline TNO film [70]) which leads to an overall increased resistivity of the thin film with respect to the epitaxially grown ones.

These data are consistent with the electron effective mass m^* anisotropy theoretically predicted for the anatase cell; in fact, while the electron effective mass orthogonal to the tetragonal axis of the unit cell m_x^* was estimated to be in the range of $0.4 – 0.6\, m_0$ (where m_0 is the electron rest mass), which is actually the usual TCO range [100], the electron effective mass parallel to the tetragonal axis m_z^* is found to be definitely higher since no value lower then $3.5\, m_0$ has ever been theoretically deduced from anatase band structure calculations [97, 101]. Since it is known the detrimental effect of a large m^* with respect to the overall mobility (see Section 2.2.1), the reduced μ recorded for TNO polycrystalline films could be interpreted as the effect of an almost randomly oriented electron path along the thin film (due to the presence of several randomly oriented crystal domains), while in the case of epitaxially grown (001)-oriented films the electron conduction should be limited to the direction orthogonal to the tetragonal axis of the unit cell (i.e. providing a higher mobility due to the lower electron effective mass m_x^*). The predicted positive effect for an electron path limited to the x-axis of the anatase cell on the overall mobility of the thin film was experimentally

demonstrated by N. Yamada *et al.* [102]. In this work a preferential (001)-orientation has been obtained for polycrystalline TNO thin films; this resulted in the highest mobility ever recorded for a TiO_2-based polycrystalline TCO (μ = 9.1 $cm^2V^{-1}s^{-1}$ for n = 1.7×10^{21} cm^{-3}). Nonetheless, apart from the evidenced anisotropic conductivity of the anatase cell, the intrinsic effect of grain boundaries should be certainly considered to play a role in decreasing the overall mobility of polycrystalline thin films with respect to the epitaxially grown ones.

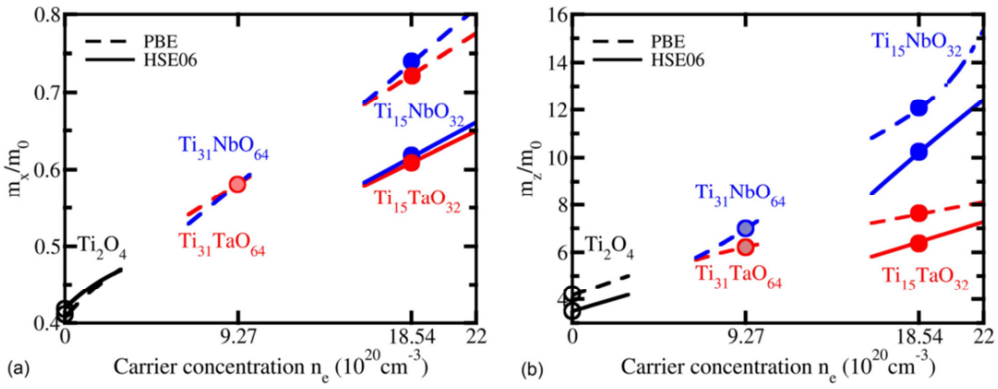

Figure 10 Orthogonal m_x (a) and parallel m_z (b) optical effective mass with respect to the tetragonal axis of the anatase unit cell of TNO (blue) and TaTO (red), calculated from DFT by the Perdew-Burke-Ernzerhof - PBE (dashed lines) and screened hybrid functional in the generalized Kohn-Sham-theory - HSE06 (solid lines) functionals. The circles represent values calculated from the band structure of the respective supercells. The lines are extrapolations assuming no change in the bands for small concentration changes. Both pictures are taken from reference [97].

It is interesting to note that on the basis of the comparison between experimental data and DFT calculations, H. Huy *et al.* [97, 101] found a dependency of the optical effective mass in both the cell directions as a function of n (Figure 10 (a) and (b) for orthogonal m_x and parallel m_z optical effective mass with respect to the tetragonal axis respectively [97]); in particular, a severe increase of m_z with increasing charge carrier concentration for both TNO and TaTO was evidenced (Figure 10 (b)).

Nevertheless, the enhancement of the optical effective mass with n in the direction parallel to the main axis of the Ta-doped system was calculated to be less than 60% of that occurring in Nb-doped anatase. This, together with a considerably higher solubility of Ta with respect to Nb in TiO_2, could represent a definitive advantage for TaTO polycrystalline films with respect to TNO for TCOs application [97]. Despite these considerations, TaTO is considerably less studied then TNO, especially in the case

of polycrystalline thin films, about which just a few works have been published [78, 79].

2.4 Donor-doped TiO_2 in solar cell devices: beyond the TCO application

Donor-doped TiO_2 is an interesting material also for applications outside of the TCO field. In fact, several research fields/applications which are already employing TiO_2 could effectively take advantage of the possibility to control and modify the functional properties of this material as a function of the presence of an extrinsic doping element, like electrocatalysis or water splitting processes [10, 103]. Nevertheless, in the next sections, and more in general in this thesis work, we decided to particularly focus on the advantages related to the implementation of donor-doped TiO_2 in solar cell devices.

2.4.1 Electron selective layer

In Section 2.1 we have already discussed the working principles and the possible architectures of dye sensitized and perovskite-based solar cells. In particular the necessity of implementing an electron selective compact layer of TiO_2 in order to avoid an intimate contact between the photoactive material and the TCO (i.e. so to reduce charge carriers back recombination processes) was discussed for solid state devices.

It has been recently demonstrated that the substitution of the nominally undoped TiO_2 selective layer with a Nb-doped one could led to superior device performances for both dye sensitized and perovskite-based solar cells [104, 105]. Since the electron selective layer should be characterized by a lower charge carrier density with respect to the TCO (see Section 2.1.1 and 2.1.2), for this kind of application the TNO layer is thermal treated in oxygen-rich atmosphere (according to the defect chemistry considerations discussed in Section 2.3.2). The presence of the doping element in the compact layer was shown to result in an overall increase of the device efficiency. This evidence was discussed to be related to an increased injected electron transport efficiency with respect to the undoped TiO_2 and to a better suited energy level alignment with respect to the FTO electrode. This last point has to be discussed in light

of the presence of an energy barrier between the TiO_2 selective layer and the FTO (see Section 2.1.3). As discussed by X. Yin *et al.* [105], the presence of Nb in the anatase cell should increase the charge carrier density with respect to the undoped material (although it should be pointed out that the crystallization process has been performed in air, resulting in a non-metallic film); this should increase the electron conductivity of the selective layer with respect to the undoped material, and bring the Fermi energy position closer to the conduction band. Consequently, a higher but narrower Schottky barrier results at the interface with the FTO compared with that for pristine TiO_2. Since the presence of the energetic barrier at the interface is thought to enable the passage of electrons from the selective layer to the TCO via tunneling effect, the presence of a sharp and narrower barrier in the case of the doped material results in a more efficient electron transfer to the front electrode. Moreover, the possible presence of a higher energetic barrier is discussed as a function of the collected experimental evidence of a more efficient ability to block the backward electron transport [105].

Although the upshift of the Fermi energy level could be present even in the case of air-annealed TNO, it should be pointed out that the corresponding effect related to the formation of a sharper Schottky barrier could be considered as a second order effect under working conditions (i.e. illumination), due to the injection in the selective layer of the photogenerated electrons which was already discussed to cause the formation of a quasi-Fermi level close to the conduction band in the selective layer (see Section 2.1.3) [5].

2.4.2 Photoanode

It has been recently reported in literature on the ability of increasing the overall efficiency of DSSC devices using a Nb-doped TiO_2 nanoparticles network as a photoanode material [106, 107]. The recorded electron-transfer efficiency improvement is proposed to be connected to an increased core conductivity of the nanoparticles induced by the presence of the dopant. Nevertheless, it should be considered that the electronic transport throughout an interconnected network of nanoparticles is a slow trap-limited diffusion process due to the presence of a severe amount of grain boundaries and defects, and so potentially very different with respect to the electronic conduction expected in a compact layer [4].

Ta has been tested as a donor element for DSSC photoanodes by the research group of R. Lopez [8, 108]. In this case the improved performances obtained for the DSSC tested devices were also connected to the ability to substitute the sintered nanoparticle architecture with a hierarchically grown TiO_2-based "nano-forest" architecture obtained via PLD technique (see Figure 11).

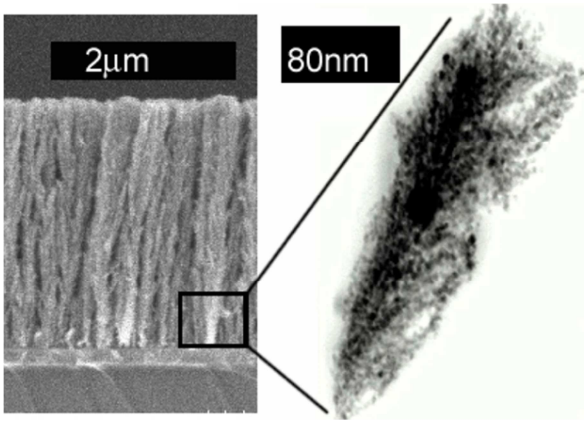

Figure 11 SEM micrography of Ta-doped TiO_2 "nano-forest" obtained by PLD and tested as a photoanode in DSSC devices. On the right a magnification of a single vertically-oriented "nano-tree" is shown. Picture taken and modified from reference [8].

The improved efficiency is shown to be connected in this case not only to the Ta-doping itself, but also to the thin film morphology, which could be able in principle to guarantee a better conductivity in the vertical direction (i.e. along the single "nano-trees", see Figure 11). Moreover, the ability of finely controlling the morphology at the nano- and meso-scale could lead to a light scattering control of the incoming radiation by the photoanode [11].

2.5 Objectives of this work

The main goal of this thesis work is to develop Ta-doped TiO_2 thin films in order to study the material functional properties; in particular we tried to unveil TaTO full potentialities as a new type of TCO, also discussing on its possible future implementation in new generation solar cell devices as a selective layer/photoanode. We focus on the physical aspects behind the functional properties of the material, aiming to understand and control its defect chemistry as a function of several deposition/annealing conditions (e.g. p_{O2} dependence, crystallization process) with particular interest on their relation with stoichiometry and structure at the atomic or nano-scale.

In order to achieve a fine control on the functional properties of the investigated material and to study the possibility to obtain different morphologies (e.g. compact-porous), PLD technique is chosen to synthesize TaTO as well as undoped TiO_2 films as it is known to be one of the most effective and highly controllable techniques for the deposition of functional oxides [109]. Compact as well as porous polycrystalline films are obtained via room temperature depositions on glass substrates so as to obtain amorphous TaTO thin films which are subsequently thermal treated in *ex-situ* annealing cycles.

Several characterization techniques are systematically carried out on the synthesized films in order to determine their morphology (Scanning Electron Microscopy - SEM), crystalline structure (Raman Spectroscopy), electrical properties (*i.e.* resistivity, carrier density and mobility by Van der Pauw and Hall effect measurements) and optical properties (UV-vis-NIR absorption/transmission/reflection spectroscopy). Moreover, fruitful external collaborations established during the PhD enabled to enrich the quality of the work:

- D. Chrastina (XRD measurements) and R. O. Ferragut (Positron Annihilation Spectroscopy – PAS), L-NESS, Dipartimento di Fisica, Politecnico di Milano, Como;
- M. Amati and L. Gregoratti (Scanning Photo Electron Microscopy – SPEM), Elettra – Sincrotrone Trieste S.C.p.A., Trieste;
- A. Abbotto and N. Manfredi (realization of perovskite-based solar cell devices), Dipartimento scienza dei materiali, università Milano Bicocca, Milano;
- G. Gregori (study on the material defect chemistry), T. Acartürk and U. Starke (Secondary Ion Mass Spectroscopy - SIMS), Department of physical chemistry of solids, Max Planck Institute for solid state research, Stuttgart;
- T. Hitosugi and S. Nakao (synthesis of TNO thin films), Kanagawa Academy of Science and Technology (KAST), Japan.

3. Synthesis of doped TiO_2 thin films

In this chapter we present the basic aspects on the synthesis of TiO_2-based thin film. After having discussed the main experimental parameters which can rule the thin film growth mechanisms with our PLD apparatus (Section 3.1.1), we present the methods which have been employed to obtain TaTO samples with different doping amounts (Section 3.2). We then focus on the relationship between the oxygen background pressure employed during the deposition process and the obtained thin film morphology (Section 3.3). Finally, we report on the *ex-situ* thermal treatments performed on the as deposited samples (Section 3.4).

3.1 Pulsed Laser Deposition technique

Pulsed Laser Deposition is a physical vapor deposition process carried out in a controlled atmosphere which is appositely obtained in the deposition chamber. The PLD apparatus is schematically represented in Figure 12. Highly energetic laser pulses are focused on a solid target; its surface is consequently ablated and the vaporized chemical species form a plasma with a characteristic plume shape. The chemical species which constitute the plume condense on the surface of the substrate which is placed in front of the target, and consequently the film growth takes place. The ablation and condensation processes are confined in a closed system: the deposition chamber. Inside the deposition chamber, the presence of a pumping and a gas inlet system is ensuring the presence of a controlled environment in a variable pressure range.

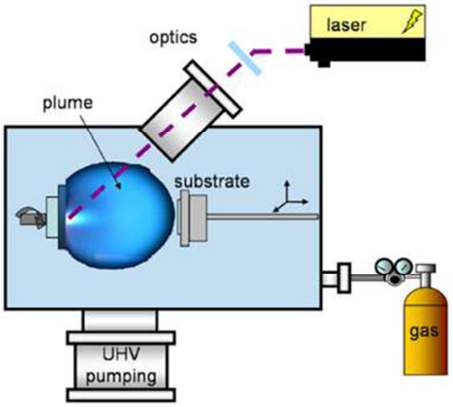

Figure 12 Schematic representation of a PLD apparatus. Modified picture from [110].

The physics of the ablation process and plume expansion is a very complex matter, highly dependent on the background pressure in the deposition chamber and on the gas employed (which could be a passive or an active medium, i.e. reactive or inert with respect to the chemical species involved) [110], the laser parameters such as the pulse energy, the energy density on the target surface (laser fluence), pulse duration (nanoseconds vs. pico/femto seconds), wavelength, light polarization, laser repetition rate (frequency of the impinging pulses) and the ablated material which is constituting the solid target (e.g. oxide or metal) [111]. A complete description of these processes is beyond the scope of this work, and just the aspects which result beneficial to the understanding of this work will be briefly presented.

3.1.1 PLD apparatus and deposition mechanism

The PLD apparatus which has been used to deposit all the thin films studied in this work is shown in Figure 13. It is equipped by a Continuum-Quantronix Powerlite 8010 Qswitched Nd:YAG pulsed laser. The most employed wavelength for the depositions was in the UV, obtained starting from the fundamental laser wavelength (IR, λ = 1064 nm) with two frequency multipliers (4th harmonic, λ = 266 nm). The pulse duration is 6 ns, the energy per pulse was maintained at 75 mJ, and the repetition rate at 10 Hz. The laser spot size on the target (and thus the laser fluence, having fixed the energy per pulse) was varied with a plano-convex lens with focal length = 50 cm. The adopted system is properly designed so to permit a roto-translation of both target and substrate; this ensures the ability to obtain an homogeneous ablation of the target, as well as the obtainment of several twin samples in a single deposition process since a

proper axial offset of the rotating sample holder results in the formation of a peripheral circular crown (~ 1 cm wide) of homogeneously deposited material (the adopted target-substrate misalignment is visible in Figure 14 *(c)* and *(d)*).

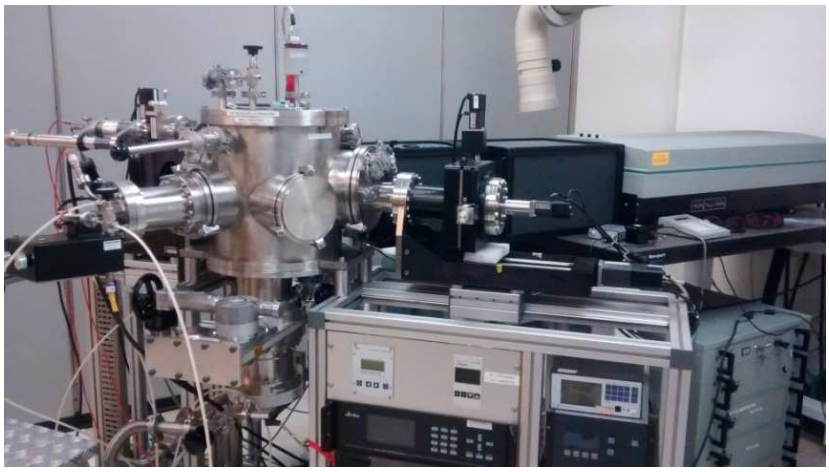

Figure 13 Apparatus employed for the deposition of the thin films studied in this work.

For an oxide target (e.g. TiO_2) hit by nanosecond laser pulses the ablation mechanism is mainly controlled by thermal conduction through the lattice. The range of laser fluence employed in this experimental work (0.9 – 3 J/cm^2) and the wavelengths investigated (mainly limited to λ = 266 nm) ensure the absorption of an high energy density by a small volume of the target material causing its vaporization. This laser-matter interaction process takes place in the first hundreds of picoseconds and leads to the formation of a plasma on the target surface, i.e. a gas constituted by electrons and ionized species; the plasma formed during the PLD process possesses the peculiar characteristic to basically preserve the same cationic ratio of the ablated target material. Since plasma expansion starts when the laser pulse is still impinging on the target surface (nanosecond laser pulse duration), the energy is then efficiently absorbed by the plasma itself leading to kinetic energy increase of the ablated species (in the range of 10 – 100 eV) [109-111]. Since the typical timescale for the ablation plume to reach the substrate surface (sample holder placed in front of the target at a fixed distance of 5 cm) is in the order of several microseconds, the laser frequency employed in our experiments (10 Hz) ensures that the laser plasma interaction is limited to a single shot process [109].

Once the single pulse is finished the highly energetic plasma plume expands in the normal direction from the target surface. The dynamics of this process is strictly

related to the background pressure in the deposition chamber. In particular it is possible to identify at least two different deposition regimes:

1. a low pressure regime which ensures a reduced scattering of the ablated species with the background gas in the deposition chamber (in Figure 14 represented *(a)* schematically and *(c)* shown experimentally);
2. a high-pressure regime in which a large amount of collisions between ablated species and gas molecules strongly reduces the overall plume energy leading to its spatial confinement, i.e. expansion up to a so called stopping distance (Figure 14 represented *(b)* schematically and *(d)* shown experimentally).

In case 1) the chemical species ablated from the target preserve most of the initial kinetic energy up to the condensation on the substrate surface (several tens of eV). Usually this condition leads to an almost atom-by-atom deposition mechanism, resulting in a compact, dense thin film morphology.

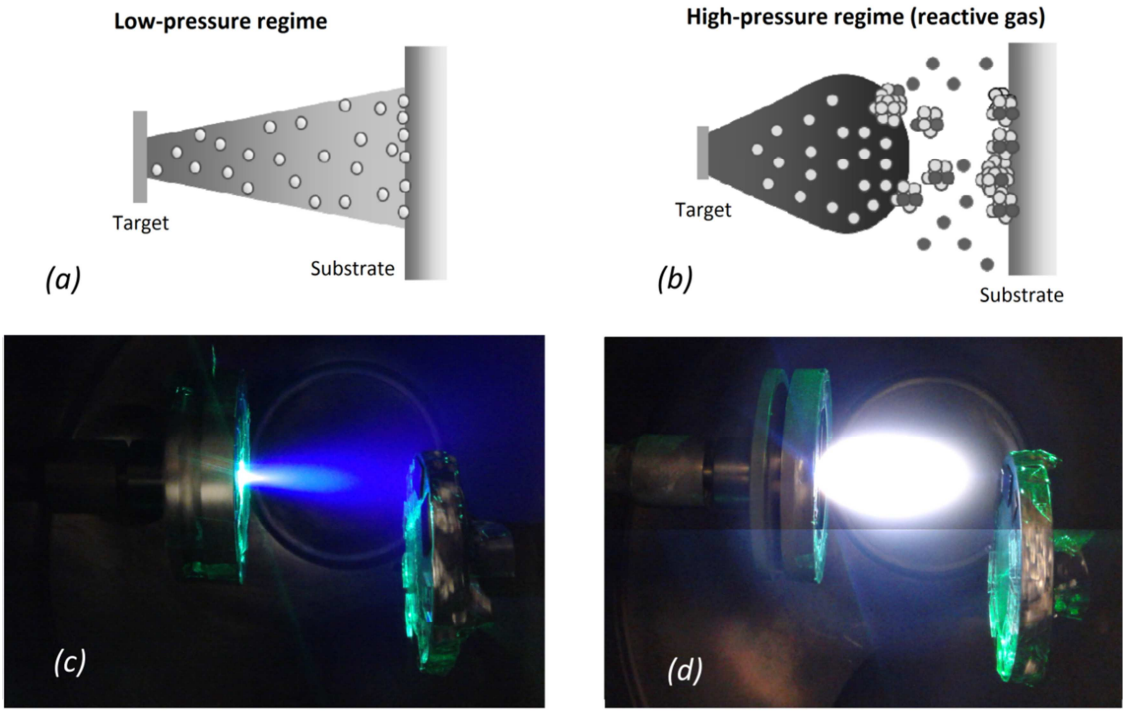

Figure 14 Schematic pictures of the plasma plume expansion dynamics in presence of a *(a)* low and *(b)* high background pressure in the deposition chamber (pictures taken from reference [110] and modified); *(c)* and *(d)* are pictures taken *in-situ* in our experimental apparatus during the ablation of a TaTO target in presence of an oxygen background pressure of 1 Pa (representative of the low pressure regime dynamics *(a)*) and 10 Pa (representative of the high-pressure regime dynamics *(b)*) respectively.

On the other hand, in case 2) the presence of a relatively high background pressure during the deposition process is causing the formation of a travelling shockwave, leading to a well-defined plume spatial confinement. In fact, the several collisions with the gas molecules in the surroundings produce an overall reduction of the kinetic energy of the atomic species in the plume (down to even fractions of eV); the radiative de-excitation mechanisms of the ablated atoms is the mechanism behind the brighter color of the confined plume showed in Figure 14 *(d)* with respect to the one obtained at a lower background pressure (Figure 14 *(c)*). These conditions favor the nucleation of low-energetic clusters in the gas plume before reaching the substrate, eventually leading to the formation of a porous thin film constituted by a nanostructured assembly of clusters [109, 110]. Although the background pressure has been discussed to rule the film morphology, other parameters like the laser fluence, the mass flow of the incoming gas and the target-to-substrate distance can contribute to its determination.

Moreover, it should be considered that in this work the TiO_2-based thin films are all deposited in oxygen, meaning a reactive background atmosphere. In this case the gas molecules which are present in the chamber are not just able to rule the kinetic energy of the ablated species, but also play an active role in the stoichiometry determination of the obtained thin film.

3.2 Change of the extrinsic doping amount in TiO_2-based thin films

Being able to obtain an atom-by-atom condensation of the ablated species and to transfer to the deposited thin film the cationic stoichiometry of the target, PLD permits the deposition of highly complex multicationic crystal structures (e.g. layered superconducting cuprates) [109]. For this reasons this is one of the most indicated techniques in order to obtain an high control level of the doping incorporation in thin films.

In our study case, we focused on the ability of obtaining Ta-doped thin films with several nominal doping amounts (Ta = 0 – 1 – 5 – 10 at.% with respect to Ti). Taking advantage from the ability to preserve the cationic ratio of the ablated material, TaTO with nominally 5% and 10% doping amount were obtained ablating sintered Ta_2O_5:TiO_2 (molar ratio of 0.025:0.975 and 0.05:0.95 respectively, starting powders purity 99.99%) targets. In the case of the undoped TiO_2 thin films a single component

target has been used (TiO_2 starting powder purity 99.9%). In order to obtain a low level of Ta doping amount an heterogeneous target has been created partially covering the undoped TiO_2 target with Ta-metallic wires (purity 99.95%, diameter 0.25 mm). This led to the deposition of thin films with a Ta content which has been estimated to be around 1 at.% from XPS measurements, as discussed later in this thesis (Section 4.3.3).

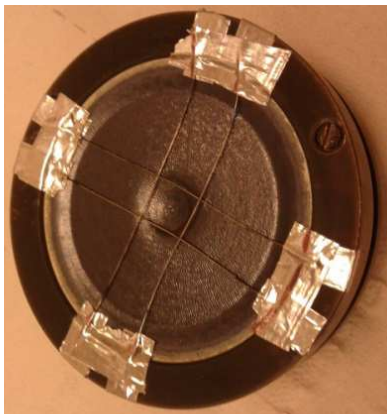

Figure 15 Picture of the heterogeneous target (TiO_2 sintered disk + Ta metallic wires network) which has been ablated to obtain TaTO thin films with ~ 1 at.% of Ta-doping amount.

Since it is difficult to state *a-priori* the difference in the ablation rate between the oxide target and the metallic wires (e.g. laser wavelength effect on oxide vs. metal ablation rate, cylindrical shape of Ta wires), it was experimentally found that an effective doping with high reproducibility is obtained for the ablation of an heterogeneous target with the metallic wire network illustrated in Figure 15.

3.3 Background pressure-driven morphology

Since among all the TiO_2-based sample depositions the target-to-substrate distance was maintained as a fixed parameter and the laser fluence has been just slightly varied, we can safely assume that in these conditions the final film morphology is basically just determined by the oxygen background pressure adopted during the laser ablation process (see Section 3.1.1). In order to obtain a controlled atmosphere in the deposition chamber, a base vacuum ($p < 4 \times 10^{-3}$ Pa) is previously realized with a pumping system consisting of a primary and a turbomolecular pump; the desired background pressure is subsequently achieved by injecting pure oxygen (5.0 purity degree) with a mass flow controller.

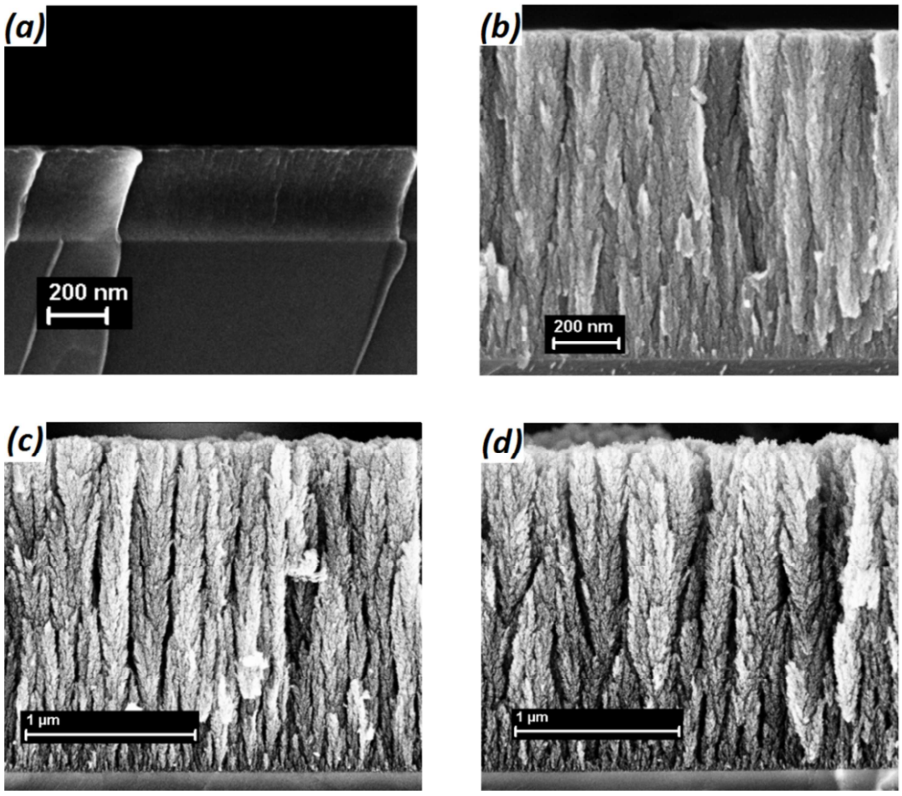

Figure 16 SEM micrographies of TaTO films deposited on Si (111) substrates at different O background pressures:*(a)* 1 Pa (Ta = 1 at.%), *(b)* 5 Pa (Ta = 1 at.%), *(c)* 10 Pa (Ta = 5 at.%), *(d)* 15 Pa (Ta = 5 at.%).

Consistently with what has been previously discussed in Section 3.1.1 we were able to identify two deposition regimes in room temperature PLD of TiO_2 thin films as a function of different oxygen background pressures (p_{O2}):

- **$p_{O2} \leq 2.5$ Pa**, large kinetic energy deposition process (Figure 14 *(a)* and *(c)*) leading to a compact thin film morphology (Figure 16 *(a)*);
- **$p_{O2} \geq 5$ Pa**, nanoparticles formation in the gas phase and deposition at significantly lower kinetic energy (Figure 14 *(b)* and *(d)*) leading to a nanoporous morphology (Figure 16 *(b)*, *(c)* and *(d)*).

Furthermore, we noticed that while no morphological changes can be evidenced by SEM in the case of compact thin films deposited in a wide range of $p_{O2} \leq 2.5$ Pa, in the framework of the second regime nanoparticles assemble in vertically oriented nanostructures which result more "open" and well separated with increasing the oxygen background pressure (see morphologies obtained at $p_{O2} = 5 – 10 – 15$ Pa in Figure 16 *(b)*, *(c)* and *(d)* respectively). Consistently, it has been shown that this leads to the possibility to control the overall surface area of the porous films obtained, which can be

tuned in the range of 10 – 100 m^2/g by changing the p_{O2} and the overall film thickness [11, 112].

Moreover, once fixed the p_{O2} during the ablation process, no morphological changes were noticeable in TiO_2-based thin films as a function of a different doping amount.

3.3.1 Hierarchical growth of TiO_2-based films

The ordered arrangement of TiO_2 nano-sized particles which are formed in the gas phase during the ablation process is strongly dependent on the p_{O2} in the chamber. This evidence was discussed in Section 3.1.1 to be related to the ability of changing the kinetic energy of the species that are reaching the substrate. In particular it has been shown in Section 3.3 that in the p_{O2} = 5 – 15 Pa regime, it is possible to reach a nanoparticle assembling which leads to a film morphology resembling a nanoforest [19]. The growth mechanism in this case is similar to a ballistic deposition model which is used to study sedimentation phenomena of colloidal particles [113, 114]; in fact, due to the low kinetic energy regime the incoming nanoparticles are aggregating without any significant diffusion mechanism after reaching the substrate [115].

Each tree which is constituting the nanoforest can be conceived as growing starting from a single seed particle deposited on the substrate (Figure 17 *(b)*). The growth of every single nanotree is hierarchical and usually evolves in the formation of bundles in the case of several micrometers thick films (Figure 17 *(a)*); their typical lateral size (and consequently their surface area and characteristic porosity) is increased by increasing the p_{O2}[*]. The nanotrees (or eventually their bundles) are characterized by a vertically connected structure, while they result to be well spatially separated in the substrate plane direction (Figure 17 *(c)*). The nanoparticles which are constituting the elementary building blocks of the nanostructures are characterized by a typical dimension in the order of 10-20 nm (Figure 17 *(d)*).

[*] For a too high background pressure (p_{O2} in the order of 100 Pa) the typical nanotree shape is lost, and the thin film results in a foam-like microstructure (not shown in this work).

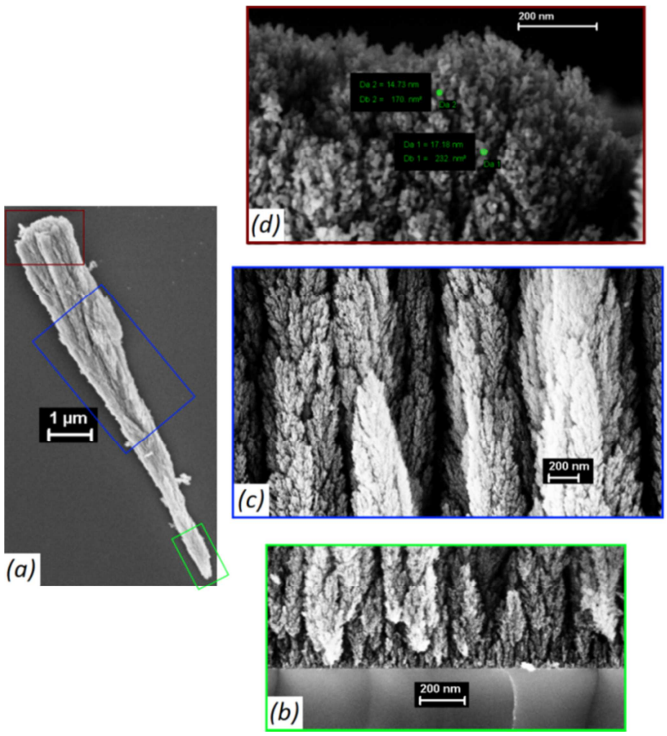

Figure 17 SEM micrographs acquired for TaTO thin films deposited on Si substrates at P_{O2} = 15 Pa; *(a)* a bundle of nanotrees detached from the substrate (Ta = 5 at.%); magnified details for TaTO nanoforests: *(b)* nucleation sites (seeds) for the single nanotrees growth (Ta = 5 at.%), *(c)* evolution of vertically oriented and spatially separated nanotrees (Ta = 5 at.%), (d) high magnification of the upper part of a nanotree with typical dimension of the constituting nanoparticles (Ta = 0 at.%).

The typical dimensions of these hyperbranched structures range from the nanometric to the micrometric scale (e.g. leaves, branches, trunks of the nanotrees and voids among them). For this reason, the possibility to tune the characteristic features of this morphology as a function of deposition conditions (e.g. p_{O2}) is thought to have important implications in light scattering processes [115].

3.4 Annealing treatments

All the TiO_2-based thin films deposited on soda-lime glass substrates were systematically investigated by means of Raman spectroscopy; the typical feature of all the as-deposited samples via room temperature PLD is the presence of broad bands typical of the absence of a long range order. In Figure 18, the black line represents the commonly obtained spectra for the amorphous films.

The samples were usually thermal treated *ex-situ* in different atmospheres so to induce their crystallization. In the case of air annealing treatments a Lenton muffle

furnace has been used; the typical thermal cycles exploited in this work involved heating ramps of 4 – 8 °C/min up to temperatures of 500 – 550 °C. A dwell time of 1 or 2 hour was usually employed at the peak temperature. The cooling ramp in the muffle is usually not precisely controllable (cooling time in the order of 4 – 5 hours to reach room temperature starting from 500 – 550 °C) because of its high thermal inertia.

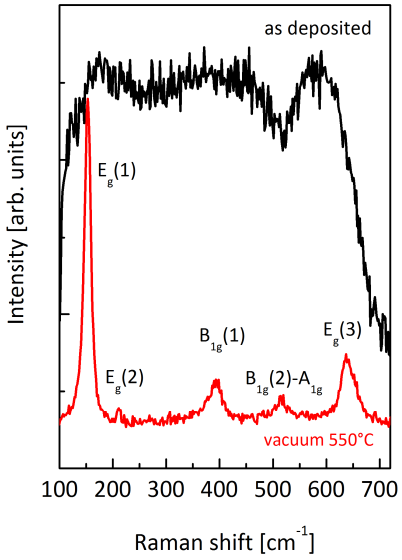

Figure 18 Raman spectra of as-deposited (black line) and vacuum annealed (red line) TaTO thin films deposited at 1.25 Pa oxygen background pressure; picture taken from our published work [116] and modified.

Annealing cycles in vacuum and in controlled atmospheres at atmospheric pressure (Ar, N_2, Ar/H_2 mixture with 3% of H_2) were performed in a home-made furnace equipped with a pumping system consisting of a primary and an Agilent Varian Turbo-V 250 turbomolecular pump (base vacuum $p_{O2} < 4 \times 10^{-5}$ Pa). The heating and cooling temperature ramps employed were always maintained at 10 °C/min. Several annealing temperatures (400 – 550 °C) and dwell times (10 – 60 minutes) have been investigated.

When a thermal cycle is performed at a temperature > 450 °C the thin films become polycrystalline and the Raman spectra always show the presence of pure anatase phase regardless of the thin film morphology (e.g. compact / porous), background annealing atmosphere employed, or the presence of different amounts of the extrinsic dopant. The red line in Figure 18 shows the typical Raman spectra obtained for a TiO_2-based thin film annealed in such conditions; all the Raman active modes of anatase are present: it is possible to identify the three E_g modes (with a nominal

frequency of 144 cm^{-1}, 197 cm^{-1} and 639 cm^{-1} for (1), (2) and (3) respectively), the B_{1g} mode at 399 cm^{-1} and the peak at 519 cm^{-1}, due to superposition of the remaining A_{1g} and B_{1g} modes [117, 118].

The morphology of compact thin films remains almost unchanged after the annealing treatments. In the case of hierarchically grown nanoforests, the annealing treatment usually leads to a partial sintering effect among the nanoparticles which are constituting their building blocks.

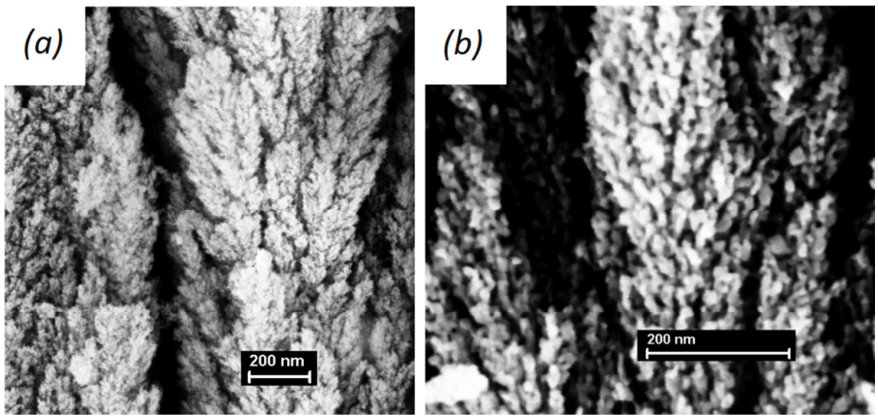

Figure 19 SEM micrographs of TaTO (Ta = 5 at.%) nanotrees obtained with room temperature PLD with a p_{O2} = 15 Pa *(a)* as-deposited, and *(b)* air annealed at T = 500 °C for 2 hours.

The sintering effect is more evident when the annealing treatment is performed in the muffle furnace (see Figure 19 to compare the morphology of an as deposited *(a)* and an air annealed *(b)* TaTO porous film); this is probably related to its discussed intrinsic high thermal inertia (i.e. slower cooling time with respect to the home made furnace). Nonetheless, the overall vertically oriented nanoforest-shaped morphology is maintained after the annealing cycles.

4. Tuning the functional properties of TiO_2-based thin films

In this chapter the ability of controlling the electrical and optical properties of Ta-doped and undoped TiO_2 films is discussed. In this framework, different thin film morphologies and compositions have been investigated. The results concerning the functional properties control of compact and porous films are presented in separate sections (Section 4.2 and 4.3 respectively). The standard experimental methods for the electrical and optical characterization of the thin films are presented in Section 4.1. The electrical characterization of porous thin films required an advanced characterization method with measurements performed at a synchrotron light facility; the basic principles of the employed technique are presented in Section 4.3.

Finally, in Section 4.4 the possible advantages of a combined compact / porous morphology on an engineered multi-layer structure are discussed, particularly focusing on the possible future implementation of an all TiO_2-based anode in new generation solar cell devices.

4.1 Experimental methods

This section is based on the materials and methods section presented in the PhD thesis of P. Gondoni [119].

4.1.1 Electrical measurements: determination of resistivity and charge carrier density

The electrical properties of all the compact thin films have been measured in 4-point probe configuration according to the configuration proposed by Van der Pauw in 1958 [120]. This technique permits the evaluation of the electrical resistivity of thin films with an arbitrary shape under the following hypothesis:

- the analyzed thin film is connected (i.e. without holes);
- the 4 electrical contacts are placed on the borders of the sample (see Figure 20);
- the dimension of the electrical contacts is negligible with respect to their distance.

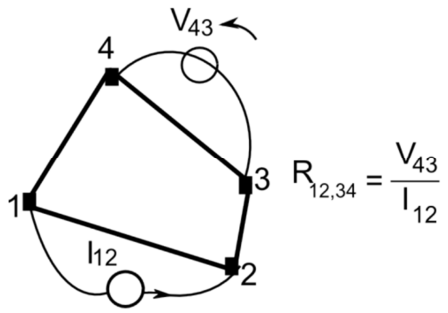

Figure 20 Schematic representation of the 4-point probe Van der Pauw configuration. Picture taken from [119].

As graphically reported in Figure 20, the resistance on one sample side is evaluated as follows: a current I is injected between two electrodes (e.g. I_{12}*), while the corresponding voltage drop is measured across the two opposite electrodes (e.g. V_{43}†). In total 8 resistance values are measured by reversing the current flow and by exchanging the electrodes configuration where the current flows and the voltage drops are measured (the adopted notation is reported in Figure 20). The recorded resistance measurements must satisfy the following relations:

$$R_{21,34} = R_{12,43} \;\Big|\; R_{32,41} = R_{23,14} \;\Big|\; R_{43,12} = R_{34,21} \;\Big|\; R_{14,23} = R_{41,32}$$

and for symmetry conditions:

$$R_{21,34} + R_{12,43} = R_{43,12} + R_{34,21} \;^{\ddagger}\Big|\; R_{32,41} + R_{23,14} = R_{14,23} + R_{41,32} \;^{\S}$$

* Where the subscript 12 is representing the direction of the current flow injected from electrode 1 to 2.
† Where the subscript 43 is representing the voltage drop measured between electrodes 3 and 4.
‡ Resistance values of the "side A" of the sample.
§ Resistance values of the "side B" of the sample.

If these conditions are verified, it is possible to evaluate the average resistance values on the two sides of the samples, called R_A and R_B. The sheet resistance of the sample R_S (i.e. resistivity per unit thickness measured in Ω/□) is then found as the solution of the equation

$$e^{-\pi\frac{R_A}{R_S}} + e^{-\pi\frac{R_B}{R_S}} = 1$$

which in the case of a square sample ($R_A = R_B = R$) can be solved as

$$R_S = \frac{\pi}{ln\,2} R$$

consequently, from the definition of R_S the resistivity of the thin film is

$$\rho = R_S d$$

Where *d* is the thickness of the thin film, which in this work is always evaluated from cross sectional images with SEM.

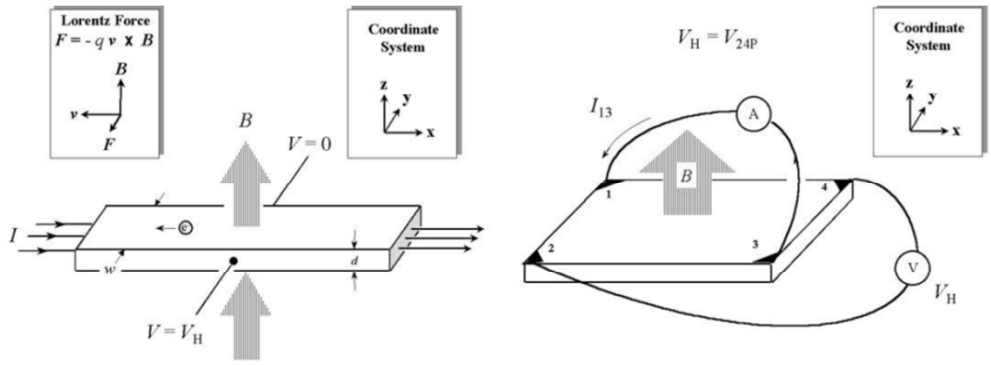

Figure 21 Schematic representation of the Hall effect in a conducting film (left) and 4-point probe configuration employed for the Hall voltage drop V_H determination along the *y* axis (right). Picture taken from [119].

Moreover, additional electrical measurements performed in different imposed flowing current – measured voltage drop configurations, in presence of an applied magnetic field with known intensity *B* (see Figure 21), enable to separate the charge carrier density *n* and mobility μ contributions from the evaluated value of the resistivity (Hall measurements). This evaluation is possible under the hypothesis of a current flow in an ideal metal within the framework of the Drude model [39]; in a classical description, when a magnetic field is orthogonally applied with respect to the current flow in a metal-like material, an electrical potential V_H is established due to the Lorentz force acting on the moving charge carriers (see Figure 21). This potential drop is the Hall voltage, and is orthogonal to both the magnetic field and the injected current *I*, and its magnitude inversely depends on the charge carrier density *n* according to:

$$V_H = \frac{IB}{qnd}$$

where q represents the charge of the majority carrier (which in our case is the electron charge). Experimentally V_H is obtained by injecting I while measuring the potential drop in crossed configurations (as schematically shown on the right side of Figure 21); the V_H measurement is repeated and averaged over all the possible diagonal configurations, and it is also performed with a reversed magnetic field in order to compensate for possible offsets. It is thus possible to evaluate n (and consequently the mobility, since $\rho = qn\mu$) for the examined thin film.

The electrical characterization was performed with a Keithley K2400 source/measure unit as a current generator (from 100 nA to 10 mA), an Agilent 34970A voltage meter, and a 0.57 T Ecopia permanent magnet.

4.1.2 *Optical measurements: UV-VIS-NIR absorbance/transmittance*

In order to determine the optical properties of the thin films, a commercial spectrophotometer (UV-vis-NIR PerkinElmer) was employed in the range λ = 250 - 2000 nm. The presence of a light monochromator and an integration sphere around the tested sample (diameter 150 mm), permit to obtain the value of the total transmitted light T over the whole solid angle as a function of λ of the impinging light. Since the measurement should represent the intrinsic optical properties of the thin film, the contribution of the glass substrate has to be considered. For this reason, the total transmittance of the bare substrate is measured as reference, and the T of the investigated sample is normalized with respect to the measured glass contribution by setting at 100% the intensity at the substrate/film interface.

The spectrophotometer allows also to experimentally measure the reflectance R of the thin films. Consequently, the absorbance A of the samples can be estimated as

$$A = 1 - T - R$$

Moreover, since TiO_2 is characterized by the presence of a wide bandgap, considering T and R in the vicinity of its absorption onset it is also possible to estimate its optical bandgap by means of Tauc plots [121]. The theoretical value of the absorption coefficient α for photons of energies $h\nu$ just above the optical gap E_G is given by [122]

$$\alpha = C(h\nu - E_G)^{1/r}$$

where C is a constant dependent on the optical transition matrix element, while r indicates the type of transition in the considered material; in the case of the samples analyzed in this work r is equal to 0.5, being TiO_2 characterized by indirect band gap transitions [66]. The graphical representation of α^r as a function of the photon energy $h\nu$ should have a linear behavior close to the material absorption edge (as experimentally shown in Figure 22); the intercept of the linear fit with the energy axis represents the optical bandgap of the material ($h\nu = E_g$ for $\alpha = 0$).

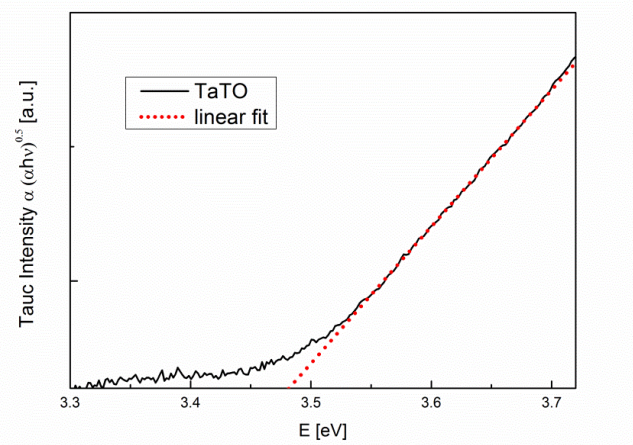

Figure 22 Tauc plot of a vacuum annealed TaTO thin film deposited at p_{O2} = 2 Pa. The red dotted line is the linear fit exploited in the range of the linear region in correspondence of the band gap absorption.

As it is possible to note from Figure 22, for a more accurate realization of the Tauc plots, $(\alpha h\nu)^r$ is considered for the Tauc intensity axis rather then α^r [123].

The absorption coefficient of the thin films has been experimentally determined from transmittance and reflectance spectra making use of the Lambert-Beer's law

$$\alpha = -\frac{1}{d} ln \frac{T}{1-R}$$

although in several cases it is possible to neglect the reflectance contribution in the vicinity of the absorption edge for the optical bandgap determination [100], in the case of TiO_2-based thin films the R contribution was found in this work to be fundamental for a correct E_G determination.

4.2 Compact thin films

Several TiO_2-based thin films were deposited on soda-lime glass and Si substrates and subsequently annealed in various atmospheres. As it was pointed out in Section 3.2, TaTO films with different extrinsic doping levels were tested. Since the

most thorough investigation was made on Ta:TiO_2 samples with a nominal Ta atomic extrinsic content of 5%, most of the presented results are referred to this composition, which has been demonstrated from literature to be the optimal doping amount for TCO's application (see Figure 8 *(b)* [61]); for this reason, when not differently specified, we will refer in this work to TaTO for thin films with this particular composition.

In this section, it is firstly considered a series of compact TaTO samples 150 nm thick deposited at room temperature in a wide range of oxygen partial pressures (p_{O2} = 1 – 2.25 Pa); the effect of annealing processes performed in several controlled atmospheres (Section 4.2.1), of different p_{O2} during the room temperature deposition process (Section 4.2.2), of a different laser fluence employed during the laser ablation (Section 4.2.3), and of the film thickness (Section 4.2.4) is discussed in the framework of the resulting thin film structural, electrical and optical properties. When not otherwise specified, we will refer in the following sections to thin films deposited with a laser fluence of 0.9 J/cm^2.

Most of the results presented in these sections were published in a peer reviewed journal [116]. The accomplished results on the optimally doped samples are exploited to study the effect of a different amount of extrinsic dopant (Section 4.2.5).

4.2.1 *Effect of ex-situ thermal treatments*

As already mentioned in Section 3.4, the as deposited films with PLD at room temperature are characterized by an amorphous structure (Figure 18). The absence of a long range crystalline order for the as deposited films is also confirmed by XRD analysis carried out by D. Chrastina (L-NESS, Dipartimento di Fisica, Politecnico di Milano, Italy) on selected TaTO and undoped TiO_2 samples (PANalytical X'Pert PRO MRD high-resolution X-ray diffractometer).

Among the several annealing cycles tested on the amorphous TiO_2-based samples, the one at 550 °C[**] for a dwell time of 1 hour (heating and cooling ramps of 10 °C/min) was found to be the most reliable thermal cycle in terms of results reproducibility, and performance (i.e. XRD peak intensity, electrical and optical

[**] Highest tested temperature due to intrinsic limitations of the soda-lime glass substrates, i.e. overcoming of glass transition temperature T_g leading to a substrate softening.

properties) thermal cycle; for these reasons from now on in this work we will refer to it as the *"standard annealing"* process. An example of the typical XRD spectra obtained for undoped TiO_2 and TaTO thin films crystallized in a standard annealing cycle performed in vacuum is reported in Figure 23. The most intense diffraction peaks of the anatase phase ((101) and (200)) are present.

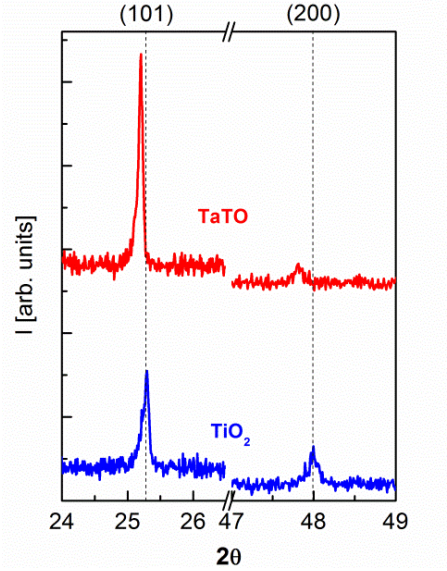

Figure 23 XRD acquisition in *θ-2θ* configuration for TiO_2 (blue line) and TaTO (red line) films after a standard vacuum annealing cycle. In the upper part of the graph, the corresponding anatase diffraction plane indexes are reported. Picture taken from reference [116] and modified.

Comparing the XRD diffraction peaks of vacuum annealed TaTO and TiO_2 (red and blue line respectively in Figure 23) it is possible to notice that the introduction of Ta atoms in the crystal lattice seems to increase the intensity of the (101) peak, while simultaneously decreases the (200) one with respect to the undoped film. This different intensity ratio was consistently recorded for several samples in *θ-2θ* configuration XRD scans. One possible explanation would imply that the presence of the doping element is able to induce a <101> preferred-oriented polycrystalline growth: since the <101> surface has the lowest surface energy for TiO_2 [124], it has been shown that anatase thin films grown on amorphous substrates can result in either randomly-oriented or <101> preferred-oriented polycrystalline forms [125]. Nonetheless, the variation in the intensity ratio could be also ascribable to a defect-induced lattice distortion or disordering strictly related to the presence of the doping element in the crystal matrix. Consistently with the last hypothesis, the presence of a sensible shift to smaller angles in both the TaTO peaks with respect to the undoped films (as visible in Figure 23) could

be partially related to a lattice expansion due to Ta incorporation in substitutional Ti sites, because the slightly larger ionic size of Ta^{+5} (0.064 nm) with respect to Ti^{+4} (0.061 nm) [61, 126]. Although the overall intensity signal of the XRD peaks was not found to be noticeably affected by the annealing atmosphere (i.e. the crystallinity), we just mention here that the peak absolute positions is dependent on the crystallization atmosphere employed. A complete discussion of the anatase cell parameters evaluated from the XRD peak positions will be presented in Section 5.1.2.

Moreover, from the collected XRD data it has been possible to evaluate the mean crystalline domain size of the thin films. In fact, crystallites of a finite size Δd lead to a broadening of a diffraction peak which can be estimated according to the Scherrer equation

$$\Delta d = \frac{K\lambda}{\Delta(2\theta)cos\theta}$$

Where *K* is a dimensionless shape factor of the order of unity, λ is the X-ray wavelength (in our case is the Cu $K\alpha_1$ line which has a λ = 0.1540562 nm), $\Delta(2\theta)$ is the peak broadening evaluated at half maximum intensity and θ is the Bragg angle. The calculated Δd for the analyzed TiO_2-based thin films annealed in air or vacuum atmospheres resulted to be comparable to the film thickness, which represents the highest possible recordable value since the Scherrer equation provides an evaluation of the mean crystalline domain size in the almost-vertical direction.

Moreover, an optical microscopy analysis with polarized light (Leitz orthoplan-pol) of the thin film surface allowed the evaluation of the grain size in the horizontal plane. The samples annealed with a standard cycle are characterized by grains in the order of tens of micrometers, and the presence of the dopant doesn't seem to play a major role. Such a gigantic expansion of the anatase grains in the post crystallization process of amorphous thin films is a peculiar property of TiO_2 which was already observed by Pore *et al.* [127]. A more detailed discussion on the fine differences recorded on the crystalline domain size and grain dimension is reported in the framework of TaTO samples deposited at different p_{O2} (Section 4.2.2).

According to the literature evidences discussed in Section 2.3.1, the obtainment of low resistive TiO_2-based thin films is strictly related to the presence of a reducing atmosphere employed in the crystallization process.

The amorphous samples show a typical resistivity value of the order of 10 Ωcm without showing any significant tendency with respect to the presence of doping (blue squares in Figure 24). Although it was not possible to discern the contributions of *n* and μ[††], this represents a clear indication that the dopant is not active in the amorphous phase of TiO_2.

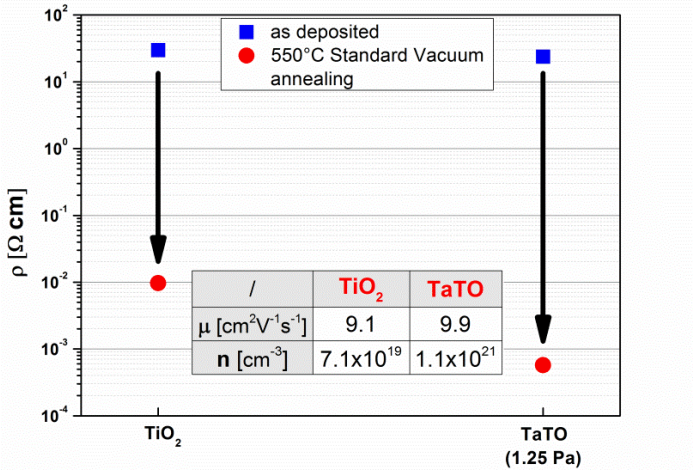

Figure 24 Effect on the resistivity of the crystallization process exploited in a standard vacuum annealing cycle for TiO_2 and TaTO (deposited in an oxygen background pressure of 1.25 Pa). The resistivity values for the as deposited films are represented with blue squares, while the crystallized ones with red circles. In the inset table are reported the mobility and the electron density obtained after the crystallization process. Picture taken from [116] and modified.

A standard annealing process performed in vacuum (red circles in Figure 24) results in a drop of nearly 3 orders of magnitude for undoped TiO_2, reaching a resistivity value of $\rho = 9.69 \times 10^{-3}$ Ωcm, comparable with the best results obtained for PLD epitaxially grown thin films [62]. The TaTO film with the best electrical properties showed a resistivity value of $\rho = 5.73 \times 10^{-4}$ Ωcm and sheet resistance $R_S = 38$ Ω/□ (150 nm thick, $p_{O2} = 1.25$ Pa, see Figure 24); to the best of our knowledge, the resistivity value for the TaTO thin film is the lowest reported in literature for a tantalum-doped TiO_2 polycrystalline film and in line with the best results obtained with the most investigated TNO (see Section 2.3.1). We just mention here that highly conducting TaTO thin films with comparable electrical properties were obtained in a standard annealing process performed in a reducing atmosphere based on an Ar/H_2 mixture (H_2 = 3%) at atmospheric pressure; this experiments are discussed in Section 4.2.2.

[††] Too scattered V_H values obtained from Hall measurements

The difference between the electrical properties of vacuum annealed TiO_2 and TaTO mainly resides in the charge carrier density, which for the doped sample is more than one order of magnitude higher ($n = 7.1 \times 10^{19}$ cm^{-3} and $n = 1.1 \times 10^{21}$ cm^{-3} for TiO_2 and TaTO respectively, see inset table in Figure 24). This evidence indicates the activation of Ta as an effective dopant in the TiO_2 anatase cell. On the other hand, the charge carrier concentration recorded for the vacuum annealed TiO_2 film should be related to the formation of a wide amount of intrinsic donor defects, like $V_O^{\bullet\bullet}$ and $Ti_i^{\bullet\bullet\bullet\bullet}$ (see Section 2.3.2).

Apart for the mere resistivity record obtained for the TaTO film, the most intriguing aspect which has to be underlined is the exceptionally high electron mobility value recorded (μ = 9.9 cm^{2}V^{-1}s^{-1}). In fact, as already discussed in Section 2.3.3 no evidence of mobility values higher than 8 cm^{2}V^{-1}s^{-1} has ever been reported for randomly oriented polycrystalline donor doped TiO_2 thin films [70]. Since this result has been obtained for Nb-doped samples, which is by far the most investigated doping element for TiO_2 for TCO application (Section 2.3.1), we note that the sensibly higher mobility value recorded for TaTO could represent the experimental demonstration of the lower effective mass theoretically predicted by H. A. Huy *et al.* [97] for Ta with respect to Nb at high charge carrier concentrations (discussed in Section 2.3.3). Nevertheless, it should be mentioned that the role of grain boundaries in determining the electron mobility value (i.e. charge carrier trapping and/or scattering processes) can play a relevant role in this framework, and is not taken into account in this discussion.

In order to understand the effect of the standard vacuum annealing process on the optical properties of TaTO, in Figure 25 *(a)* is reported the overall characterization of the sample with the best electrical properties (Figure 24). Looking at the total transmittance spectra obtained before and after the crystallization process (as deposited amorphous TaTO represented by a dotted line, while after annealing by a continuous black line in Figure 25 *(a)*), it is possible to note that the total transmittance in the visible region (T_{vis} for λ = 400 – 700 nm) is sensibly increased after the thermal treatment (T_{vis} = 70.6% and 76.6%). This increment is explained by the obtainment of an ordered structure after the crystallization process.

The T_{vis} of the crystallized film is basically determined by reflectance (R_{vis} = 18.7%, blue line in Figure 25 *(a)*), while absorption is as low as 5%. The obtained fringes and their relative positions are connected to light interference phenomena due to

the presence of multiple reflections inside the film, and are consequently related to its thickness and the refractive index. Another interesting difference between the total transmittance spectra of amorphous and vacuum annealed thin films is noticeable at $\lambda >$ 1400 nm: the crystallized TaTO shows in the near IR the absorption tail of the free carrier plasma wavelength (Section 2.2.1) due to the presence of a large amount of conduction electrons, while the as-deposited film does not show this peculiar feature. This is another evidence proving that the doping element is not active in the amorphous structure.

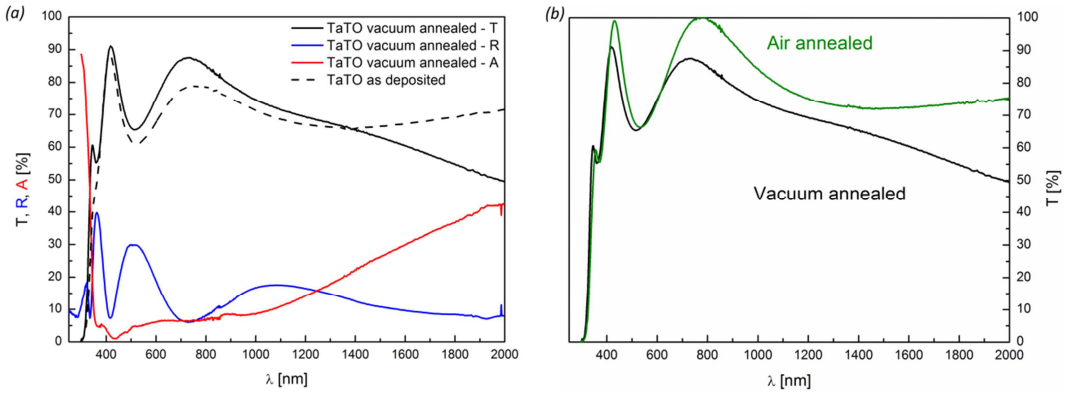

Figure 25 *(a)* Total transmittance (black line), reflectance (blue line), and absorbance (red line) spectra of 150 nm thick TaTO film deposited at p_{O2} = 1.25 Pa crystallized with a standard vacuum annealing. The black dotted line refers to the total transmittance of the same sample before the thermal cycle. Picture taken from [116]. The total transmittance spectra after the vacuum annealing process is reported also in *(b)* in order to permit a clear comparison with a twin TaTO thin film crystallized in air (green line).

When an equivalent TaTO film is crystallized in air (green line in Figure 25 *(b)*), its overall transmittance in the visible region is sensibly increased with respect to both the amorphous and the vacuum annealed one (T_{vis} = 80.0%). This is consistent with the presence of a well ordered structure also in the case of the air annealed samples, which is in line with XRD data. The overall transmittance increase recorded with respect to the vacuum annealing process could be related to a sensible decrease of the oxygen vacancy concentration in the anatase structure of the air annealed TaTO [128, 129]. Moreover, as previously discussed in the case of the amorphous film, also the air annealed TaTO does not show a decreasing transmittance in the near-IR region, pointing to the absence of a large concentration of conduction electrons (green line in Figure 25 *(b)*).

This last point is confirmed by the electrical characterization of the TaTO samples crystallized in air: this annealing atmosphere resulted in highly insulating

samples. In fact, with our experimental setup, it was not possible to measure the resistivity of both undoped and doped TiO_2. Even a standard annealing cycle performed in nitrogen (99.999 % purity, oxygen concentration nominally < 3 ppm) at atmospheric pressure resulted in highly insulating samples, not electrically measurable with our experimental setup.

Nevertheless, the collected data presented so far do not clarify if the TiO_2 electrical properties are affected even by a very little concentration of oxygen in the crystallization environment, or if the reducing atmosphere is inducing in the anatase structure a substantial variation of the thin film stoichiometry.

4.2.2 *Effect of the oxygen partial pressure during the deposition process*

The required condition in order to obtain TiO_2-based TCOs is the crystallization from the amorphous phase in a standard annealing process performed in reducing atmosphere (e.g. vacuum). Nevertheless, the electrical, optical and structural properties are found to be all strictly connected to the oxygen background pressure employed during the room temperature ablation process.

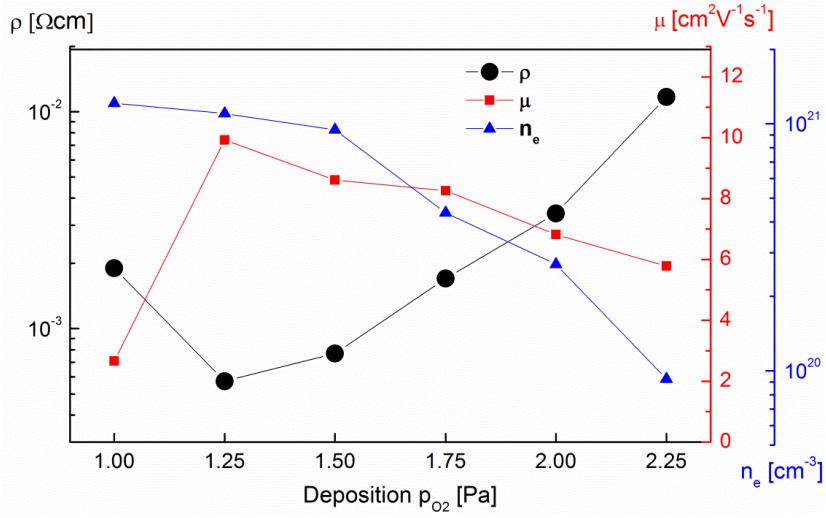

Figure 26 Electrical properties of standard vacuum annealed polycrystalline TaTO 150 nm thick films as a function of a different p_{O2} employed during deposition process. The black circles represent the resistivity, the blue triangles the charge carrier concentration and the red square the electron mobility. Picture taken from [116] and modified.

As visible from Figure 26 the control of the oxygen partial pressure employed in the deposition chamber is able to finely rule the electrical properties of TaTO thin films even though they were all crystallized in the same ex-situ vacuum annealing treatment.

Resistivity values decrease by more than one order of magnitude, as the p_{O2} is reduced from 2.25 to 1.25 Pa, while increases again with a further pressure reduction to 1 Pa. Further analyzing the contributions of mobility and charge carrier density (reported in Figure 26 as red squares and blue triangles respectively) it is possible to identify that the decrease in the electrical conductivity of the TaTO sample deposited at 1 Pa is connected to the sudden drop of electron mobility (μ = 2.7 $cm^2V^{-1}s^{-1}$, just after having reached its maximum value in the sample deposited at 1.25 Pa, μ = 9.9 $cm^2V^{-1}s^{-1}$), despite presenting the highest charge carrier density of the set (n = 1.21 × 10^{21} cm^{-3}). A sensible and continuous decrease of the charge carrier density is linked to the slight increase of the deposition pressure, which reaches the lowest value for TaTO deposited at 2.25 Pa (n = 9.26 × 10^{19} cm^{-3}). On the other hand, also the mobility is slightly decreasing in the range of p_{O2} = 1.25 Pa – 2.25 Pa by increasing the p_{O2}, and the lowest value of 5.78 $cm^2V^{-1}s^{-1}$ is obtained for the sample deposited at the highest oxygen partial pressure of the set.

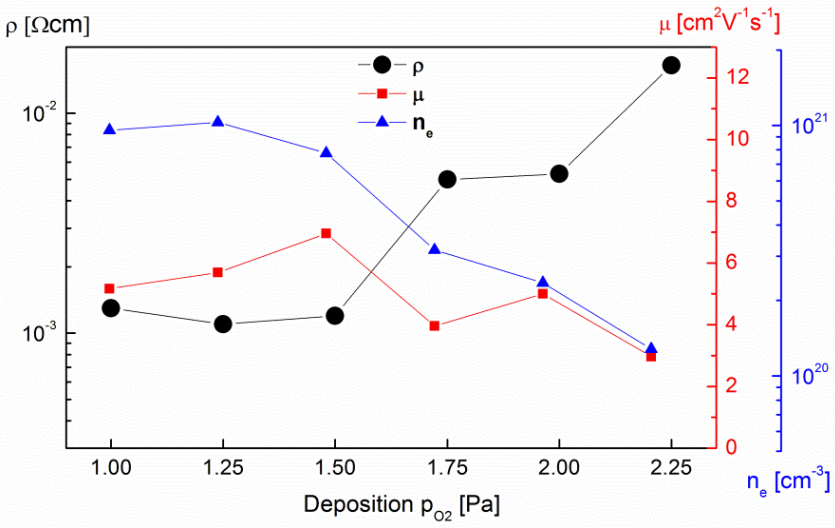

Figure 27 Electrical properties of standard annealing processed at atmospheric pressure in Ar/H_2 atmosphere (3% H_2) polycrystalline TaTO 150 nm thick films as a function of a different p_{O2} employed during deposition process. The black circles represent the resistivity, the blue triangles the charge carrier concentration and the red square the electron mobility.

For the same set of TaTO samples, a standard annealing cycle was performed also in an Ar/H_2 mixture (3% H_2) at ambient pressure. As it is possible to note from Figure 27, a very similar trend as a function of p_{O2} is present. In particular the trend of the charge carrier density is almost superimposed to the one shown in Figure 26 for the same set of vacuum annealed samples, evidencing a very similar effect on the activation

of the doping element between these two reducing atmospheres. Nevertheless, the mobility values are generally lower with respect to the ones recorded for the standard vacuum annealing process.

Focusing on the best electrical results of the standard vacuum annealing (Figure 26), the decreased mobility as a function of p_{O2} was found to be connected to a reduced crystallinity outside of the narrow deposition window of p_{O2} = 1.25 – 1.75 Pa (not shown).

Consistently, it is shown in Figure 28 that the p_{O2} is ruling the mean crystalline domain size dimension of the vacuum annealed TaTO samples. The just mentioned narrow window of deposition pressure for which the crystallinity seems to be higher is confirmed (mean domain size basically limited by the film thickness in the range of 1.25 – 1.75 Pa, Figure 28). Nonetheless, the overall values even outside the "best crystallinity" p_{O2} range are always comparable to the thin film thickness (150 nm thick samples). Also the undoped sample (blue filled circles in Figure 28) show a comparable domain size, and the effect of an annealing cycle performed in air (empty points in Figure 28) is shown to just slightly increase the mean domain size for both TaTO and TiO_2.

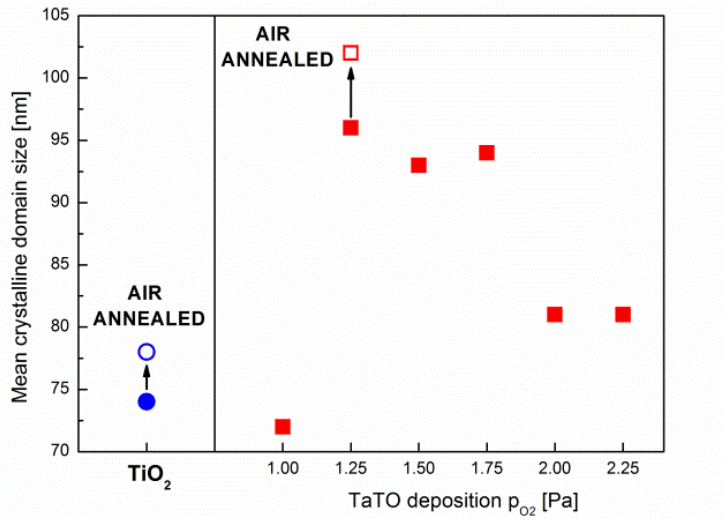

Figure 28 Mean crystalline domain size evaluated from XRD of TiO_2 (blue circles on the left side) and TaTO films (red squares) as a function of the different deposition p_{O2}, vacuum (filled) and air (empty) annealed. Picture taken from [116].

As already pointed out in the previous section (4.2.1) an optical microscopy analysis of the thin film surface permits to evaluate the grain size in the horizontal direction. In Figure 29 the effect of the slight change of the oxygen partial pressure on

the overall distribution of the lateral grain dimension of vacuum annealed samples is shown.

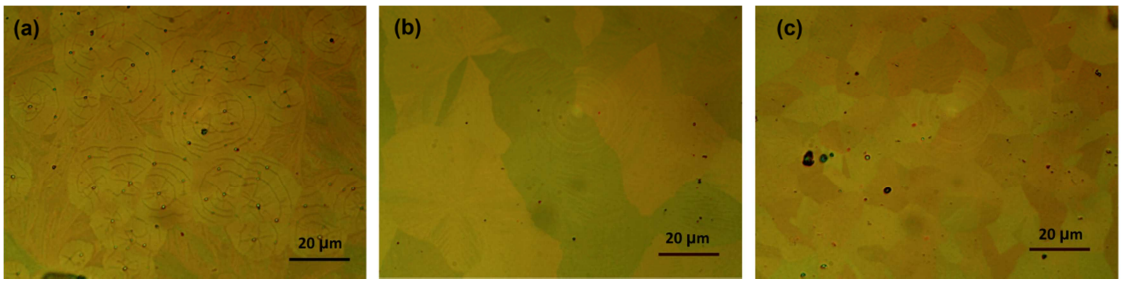

Figure 29 Surface images captured using optical microscope with polarized light of TaTO films crystallized in a standard vacuum annealing cycle and previously deposited at 1 Pa (a), 1.5 Pa (b), and 2.25 Pa (c). Image taken from [116].

Circular macro-cracks are only observed on the surface of TaTO deposited at 1 Pa (Figure 29 (a)), although the presence of macro-grains is noticed. This evidence could explain its mobility fall shown in Figure 26. Furthermore, the macro-grain dimension is following the trend obtained from the XRD analysis (Figure 28): in the narrow window of deposition pressures for which the XRD crystalline domain size is larger, the grain size is of the order of 25-30 µm (1.25-1.5-1.75 Pa, Figure 29 (b)), while for higher deposition pressures (2-2.25 Pa) the typical grain size decreases down to 10-15 µm (Figure 29 (c)).

As well as the structural and the electrical properties, also the optical properties of vacuum annealed TaTO films appear to be controlled by the deposition p_{O2}. As shown in Figure 30, a tendency to an overall higher transmittance by increasing the oxygen partial pressure is present. This is particularly evident in the near IR-region where, according to the recorded trend for the charge carrier density (see Figure 26), lower transmittance at lower pressures is in agreement with the relation with the plasma oscillation frequency (see Section 2.2.1). Also the mean transmittance values (reported in the inset of Figure 30) generally show higher values for higher oxygen deposition pressures, although for $p_{O2} \geq 1.5$ Pa the T_{vis} ramains close to values in the order of 80%. When the TaTO films deposited in the same conditions are crystallized in air, the behavior is very similar to the one discussed in the previous section for the sample deposited at 1.25 Pa (see Figure 25 *(b)*); in this case no trend is evidenced as a function of a different p_{O2} and the T_{vis} is enhanced up to 80% for all the samples without showing the free carrier absorption in the near-IR region (not shown).

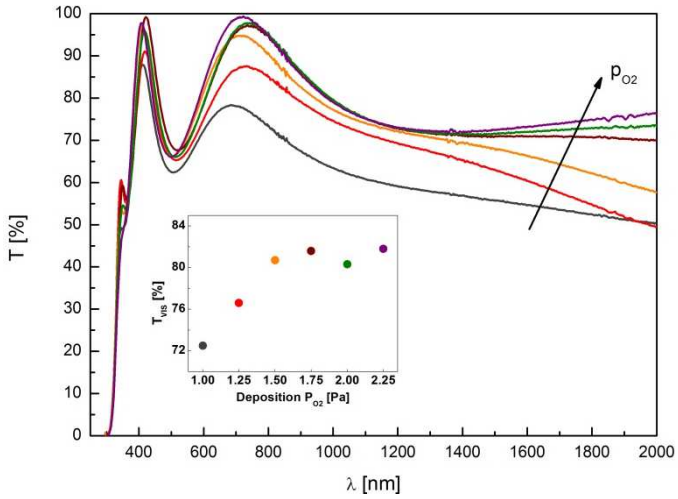

Figure 30 Total transmittance spectra of 150 nm thick TaTO films deposited at different p_{O2} and subsequently crystallized in a standard vacuum annealing cycle. In the inset the T_{VIS} as a function of the different p_{O2} is shown. Picture taken from [116].

Combining the experimental data collected for the electrical and optical characterization, it was possible to obtain a plot of the optical energy gaps (see Section 4.1.2) for the TaTO vacuum annealed films deposited at different p_{O2} as a function of their charge carrier density, aiming at evaluating the possible presence of a Moss-Burstein effect due to the filling of the conduction band (see Section 2.2.1).

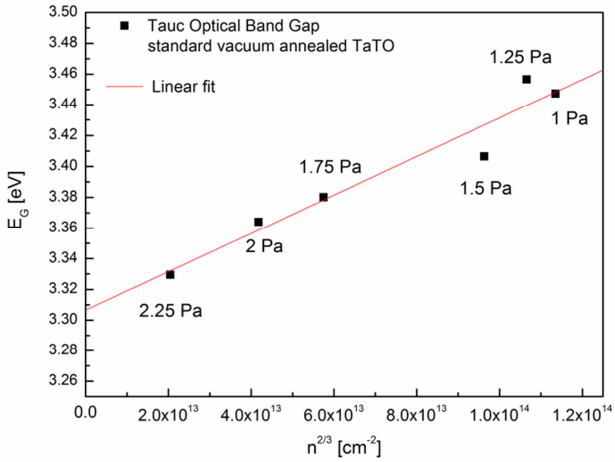

Figure 31 Tauc optical band gap as a function of $n^{2/3}$ for standard vacuum annealed TaTO films deposited at different p_{O2}. Charge carrier densities are the same reported in Figure 26. Image taken from [116] and modified.

As observed in Figure 31, E_G shows a trend as a function of the charge carrier density. The reliability of these data is confirmed by the y-axis intercept of the linear fit, that is, 3.31 eV, since this value is in line with the band gap of anatase TiO_2 (3.2 – 3.4

eV). Based on the proportionality $\Delta E_G \propto 1/m^* \, (n)^{2/3}$ (Section 2.2.1), from the slope of the linear fit it is possible to estimate the mean optical electron effective mass to be $m^* = 2.9m_0$, where m_0 is the electron rest mass. Because of the anisotropic character of the anatase cell (Section 2.3.3), the evaluated effective mass should be considered as a combination of orthogonal m_x^* and parallel m_z^* (with respect to the tetragonal unit cell axis) components, because it is likely that the electron path is almost randomly oriented since we are dealing with non-oriented polycrystalline films. According to the theoretical values reported in literature and previously discussed in Section 2.3.3, the electron effective mass evaluated in this work from optical measurements seems to be consistent. Nonetheless, this value should be read just as an estimate because it does not take into account the many-body effects and the nonparabolicity of the conduction band, which usually lead to an overestimate of the deduced m^*.

Finally, the estimated mean value of m^* allows to calculate the expected plasma wavelength λ_p (i.e. the light absorption by the "gas" of conduction electrons, see Section 2.2.1). It was found for the TaTO film with the best electrical properties (p_{O2} = 1.25 Pa, n = 1.1 × 10^{21} cm^{-3}) that $\lambda_p = 4160\, nm$. This value seems to be consistent with the transmittance spectra shown in Figure 25 *(a)*, although it was not possible to experimentally validate the maximum λ_p absorption, due to the upper limit of the spectrophotometer ($\lambda_{max} = 2000\, nm$). This high value of λ_p is definitely an advantage for TCO applications, because for other materials such as AZO, ITO and FTO the useful density of the free electrons is limited by a shift ($\propto \sqrt{m^*}$) of λ_p in the visible region (Section 2.2.1).

4.2.3 Effect of the laser fluence

In order to explore the optimization of the deposition process, the effect of a different laser fluence for TaTO and TiO_2 thin films was also explored[‡‡]. In particular higher laser fluences were investigated (1.15 J/cm^2 and 1.5 J/cm^2). The amount of ablated material is related to the energy density on the target surface, and we have just discussed in Section 4.2.2 the paramount role played by the deposition p_{O2} in determining the functional properties of these samples. Consequently, in order to

[‡‡] As previously pointed out in Section 4.2, all the samples analyzed so far were deposited with a laser fluence of 0.9 J/cm^2.

optimize the electrical properties obtained at a different fluence it was necessary to find the best oxygen background pressure for the change of this parameter. It was found that while in the case of the samples obtained with a laser fluence of 0.9 J/cm^2 the optimum electrical properties were obtained for vacuum annealed samples deposited at 1.25 Pa (see Figure 26), the increment up to 1.15 J/cm^2 and 1.5 J/cm^2 required to decrease the p_{O2} down to 1 Pa in order to obtain the best conductive properties. The electrical results are reported in Figure 32; the use of a higher laser fluence slightly increases the obtained resistivity of TaTO (from 5.73 × 10^{-4} to 6.47 × 10^{-4} Ωcm) due to a small decrease in the free electron density. The most interesting result is related to the recorded strong enhancement of the electron mobility: for a TaTO sample with the same thickness (150 nm) deposited at a laser fluence of 1.15 J/cm^2 (1 Pa O_2) it was possible to increase the mobility with respect to TaTO obtained at 0.9 J/cm^2 (μ = 9.9 cm^{2}V^{-1}s^{-1}) up to 12.5 cm^{2}V^{-1}s^{-1} (ρ = 5.90 × 10^{-4} Ωcm, n = 8.49 × 10^{20} cm^{-3}, R_S = 39.3 Ω/□). For comparison we studied also a vacuum annealed TiO_2 (150 nm) film deposited at 1.15 J/cm^2, which showed as well a noticeable increase in the electron mobility with respect to the previously tested 0.9 J/cm^2 (ρ = 6.46 × 10^{-3} Ωcm, n = 6.16 × 10^{19} cm^{-3}, μ = 15.7 cm^{2}V^{-1}s^{-1}).

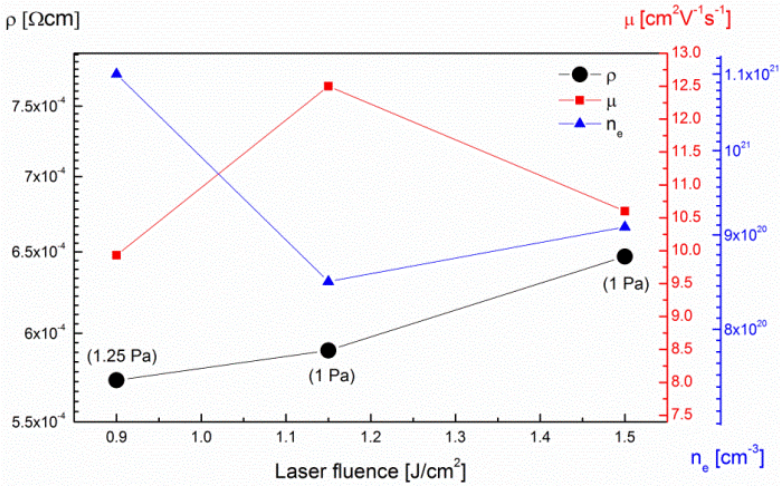

Figure 32 Electrical properties of standard vacuum annealed polycrystalline TaTO 150 nm thick films as a function of a different laser fluence employed during deposition process. In the brackets are reported the employed deposition p_{O2}. The black circles represent the resistivity, the blue triangles the charge carrier concentration and the red square the electron mobility. Picture taken from [116] and modified.

In the case of the polycrystalline TaTO film, the high mobility value obtained for the 1.15 J/cm^2 laser fluence is approaching the results obtained for the epitaxially

grown TaTO and TNO thin films on single crystal substrates (Section 2.3.1). As previously discussed in Section 4.2.1, this result further strengthens the hypothesis that Ta could have several advantages over Nb as a doping element because of a lower theoretically predicted electron effective mass in presence of a large amount of charge carriers (Section 2.3.3).

Moreover, such a large mobility value obtained for a slight increase of the laser fluence is coupled with a sensible enhancement of the overall transmittance: as shown in Figure 33, although maintaining almost the same resistivity, T_{vis} was increased of nearly 5% with respect to the sample deposited at 0.9 J/cm^2, overcoming the important TCO technological limit of 80% (T_{vis} = 81.1%).

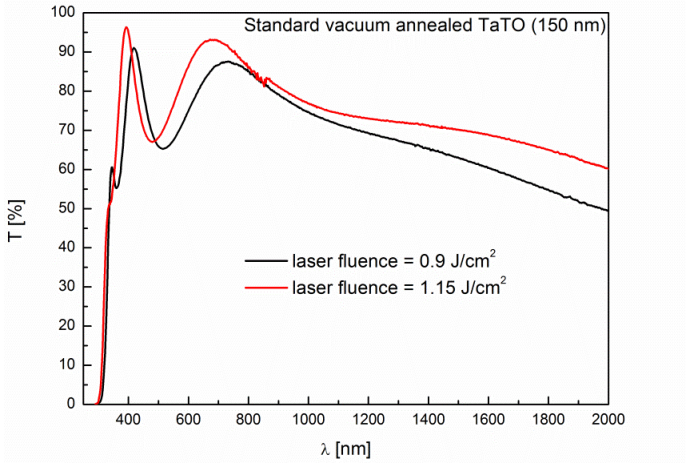

Figure 33 Total transmittance spectra of 150 nm thick TaTO films deposited at a laser fluence of 0.9 J/cm^2 (black line) and 1.15 J/cm^2 (red line) annealed in a standard vacuum annealing cycle. Picture taken from [116] and modified.

4.2.4 Effect of the film thickness

Once identified the best synthesis conditions in order to obtain the best compromise between electrical and optical properties for TaTO transparent conducting applications (laser fluence 1.15 J/cm^2, p_{O2} = 1 Pa, standard vacuum annealing process), we focused on the functional properties of a thicker film.

We verified that maintaining the very same synthesis conditions the electrical properties are almost independent with respect to the TaTO film thickness: a 295 nm thick TaTO film showed almost the same resistivity of the 150 nm one (ρ = 5.90 × 10^{-4} Ωcm for the 150 nm thick, while ρ = 5.57 × 10^{-4} Ωcm for 295 nm). This consequently leads to the possibility to linearly decrease the sheet resistance just increasing the film

thickness (R_S from 39.3 Ω/□, to 18.9 Ω/□ almost doubling its thickness). Although comparable, in the case of the thicker thin film an even higher electron mobility with respect to the 150 nm film is obtained (μ = 13 $cm^2V^{-1}s^{-1}$), while n is found to be almost unchanged.

As for the thickness effect on the optical properties, the total transmittance spectra of the 150 nm (red line) and the 295 nm (blue line) samples are reported in Figure 34. The nearly doubled thickness results in a decrease in T_{vis} of 6% (from 81.1% to 75.2%).

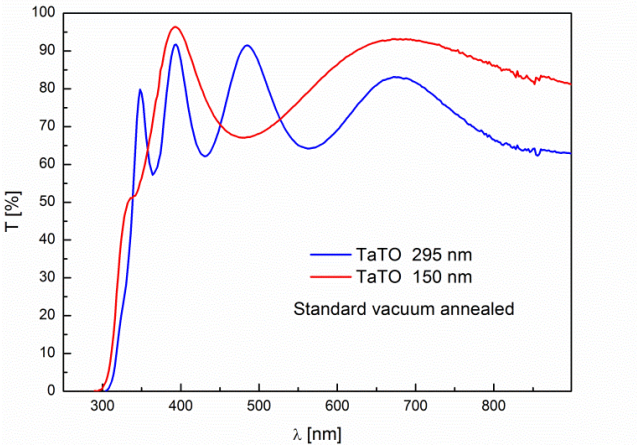

Figure 34 Total transmittance spectra of 150 nm and 295 nm thick TaTO films deposited at a laser fluence of 1.15 J/cm^2 and annealed in a standard vacuum process. Picture taken from [116] and modified.

Nevertheless, it should be pointed out that the reduced transmittance is basically due to reflectivity reasons, as absorbance has been already discussed to play a secondary role in this material (see Figure 25 *(a)*). In fact, we note that it could be possible to engineer the light transmittance at certain wavelengths in a very precise way taking advantage of the position and interspace of the well-defined and thickness-dependent interference fringes (e.g. total transmittance higher than 90% in the regions of wavelength close to 390 and 480 nm for the 295 nm thick TaTO film, blue line in Figure 34).

4.2.5 *Effect of different extrinsic dopant concentrations*

The ability disclosed in the thorough work made on optimally doped TaTO samples to finely control their functional properties has been exploited for different concentrations of extrinsic dopants. In particular we studied an underdoped (Ta content

= 1 at.%) and overdoped (Ta content = 10 at.%) composition. Since the studied thin films were not always characterized by the same thickness, for a sake of work clarity just the effect on the electrical properties is presented. In fact, the effect on transmittance should be studied on samples with the very same film thickness to be meaningful, as demonstrated in Section 4.2.4.

As well as in the case of optimally doped TaTO, it was found that it is possible to finely rule the electrical properties of the standard vacuum annealed films by tuning the p_{O2} during the room temperature deposition process; again this was found to be mostly related to the possibility of changing *n* in a wide range (not shown). Apart from the sample with Ta = 1 at.% which was exhibiting the lowest resistivity for a deposition in a p_{O2} = 1 Pa, the best electrical properties for all the other compositions were obtained for a p_{O2} = 1.25 Pa (ρ, *n* and μ as a function of different Ta doping content are reported in Figure 35).

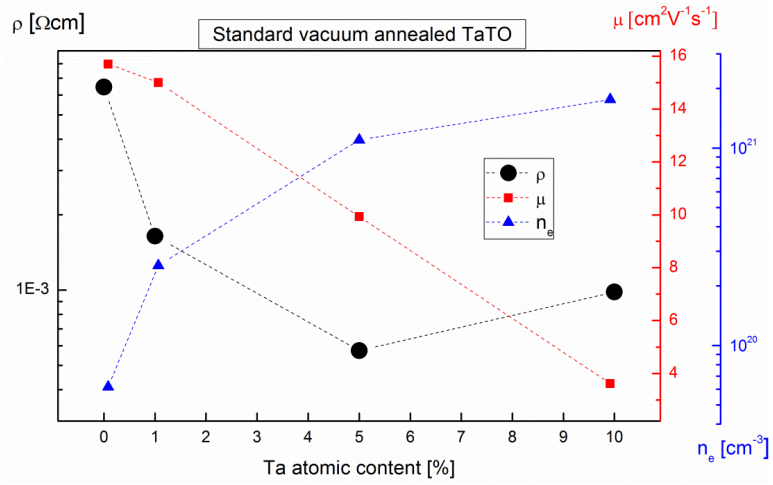

Figure 35 Best electrical properties obtained for standard vacuum annealed polycrystalline TaTO films as a function of a different Ta-doping level. The black circles represent the resistivity, the blue triangles the charge carrier concentration and the red square the electron mobility.

First of all we observe that the resistivity behavior (Figure 35) shows a very similar trend with respect to the epitaxially grown TaTO thin films with different doping amounts previously studied by Hitosugi *et al.* (see Figure 8 *(b)*) [61]. In particular ρ is decreasing from a value of 6.46×10^{-3} Ωcm of the undoped sample, down to 1.64×10^{-3} Ωcm for 1 at.% of Ta, reaching its lowest value for the 5% composition ($\rho = 5.73 \times 10^{-4}$ Ωcm). The overdoped composition is slightly increasing the resistivity ($\rho = 9.82 \times 10^{-4}$ Ωcm). The obtained absolute values are very similar to the ones reported

for the epitaxially grown corresponding compositions; this is an important indication which allows one to state that the grain boundaries are not playing a major role in determining the electrical properties of this material. This evidence is very promising for a future implementation of TiO_2-based TCOs in real devices (e.g. solar cells), and is probably connected to the ability of obtaining tens of micrometers large grains with a mean crystalline domain size along the vertical direction which is basically limited by the film thickness (Figure 28 and Figure 29).

An almost linear increase of the charge carrier density as a function of the Ta content is shown (Figure 35), basically confirming the high dopant activation efficiency of TiO_2-based TCOs (Section 2.3.3).

It is interesting to note that by changing Ta content *n* is varying in a very similar range (10^{19} – 10^{21} cm^{-3}, blue triangles in Figure 35) as the one obtained for the optimally doped films deposited at different p_{O2} (see Figure 26); it is worth to underline that the physical mechanism which is behind the tunability of the charge carrier concentration is likely to be different: while changing the amount of Ta results in a variation of the extrinsic doping amount, in the case of the *n* modulation observed in samples deposited at different p_{O2} with a fixed amount of Ta the role (direct or indirect) of several intrinsic defects should rule the trend.

Finally, also the electron mobility is found to decrease almost linearly as a function of doping amount (red squares in Figure 35). This is consistent with the expected effect due to the presence of an increasing amount of ionized impurities in the crystal lattice (see Section 2.2.1).

4.3 Porous thin films

The study of the structural, optical and electrical properties of nanotree-shaped TiO_2-based films is a very complicated matter. In fact, differently from the compact samples, in this case the film is grown starting from a nanoparticle assembly with typical dimension in the range of tens of nanometers. Moreover, the surface/volume ratio of these nanostructured film is very sensitive to the oxygen background pressure employed during the deposition process (Section 3.3). Also the characterization of these porous films is a complicated matter, especially in the case of electrical measurements due to the intrinsic impossibility to employ cross sectional 4-point probe technique (i.e.

single nanotrees have a weak connectivity on the horizontal direction, see 3.3.1). A detailed analysis of their functional properties as a function of different synthesis conditions would require a separate dedicated work. For these reasons, in the framework of this thesis some preliminary results and novel experimental approaches limited to TiO_2-based porous films deposited at 10-15 Pa, potentially interesting as photoanodes for photovoltaic devices, are discussed.

4.3.1 Structural properties

An annealing treatment is crystallizing the thin films in pure anatase phase, consistently to what discussed for the TiO_2-based compact thin films (Section 4.2.1). Nevertheless, fundamental differences have been found regarding the annealing atmosphere employed. In Figure 36, we compare the Raman spectra acquired for ~ 2 µm thick TaTO films deposited in the range 10 – 15 Pa oxygen background pressure and subsequently annealed.

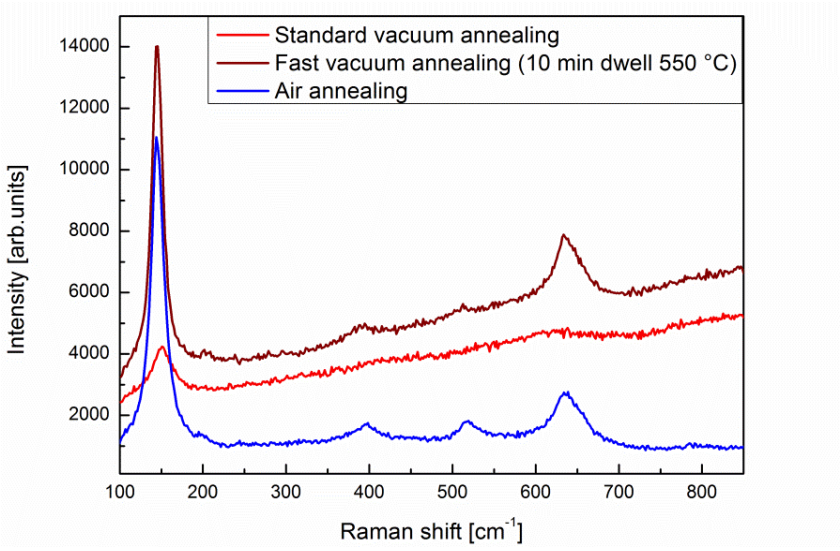

Figure 36 Raman spectra acquired for TaTO air annealed (blue line, p_{O2} = 10 Pa), standard vacuum annealed (red line, p_{O2} = 15 Pa) and fast vacuum annealed (bordeaux line, p_{O2} = 15 Pa).

The Raman spectra acquired for the air annealing process (blue line in Figure 36) is comparable to the ones collected for several TiO_2-based compact samples (see Figure 18). Nonetheless, a different behavior is recorded for nanotree-shaped thin films annealed in vacuum atmosphere. A standard annealing cycle usually results in the presence of a strong photoluminescence background (slope of the red line in Figure 36). This evidence points towards the presence of a defected structure which eventually

results in the formation of in-gap states causing photoluminescence. Due to the extremely high surface area of these porous films with respect to the compact ones, it could be hypothesized that the presence of a reducing atmosphere can result in a severe oxygen desorption from the nanoparticles surface which are constituting the building blocks of the film. This would considerably increase the number of defects in the nanostructures, since their surface is almost totally exposed to the annealing atmosphere.

Based on this hypothesis we reduced from 60 to 10 minutes the dwell time of the annealing cycle (fast vacuum annealing, bordeaux line in Figure 36), trying to reduce the overall exposure of the thin film to the reducing atmosphere at high temperature (T = 550 °C). Consistently, we found that in the framework of a fast annealing cycle performed in vacuum there is a tendency to obtain more defined anatase peaks with respect to the standard annealing (bordeaux and red line respectively in Figure 36).

Nevertheless, it is important to higlight that this discussed behavior is not systematically recorded and different annealing treatments (standard or fast) performed in the same vacuum level, sometimes turn out in very different Raman spectra, eventually showing just the presence of photoluminescence, or on the contrary very defined anatase peaks. These controversial results were obtained for TiO_2-based porous films regardless of the different amount of dopant, and are still under investigation.

4.3.2 Optical properties

The photoluminescence recorded in several Raman spectra of vacuum annealed films is sometimes accompanied by a visible darkening of the samples. This interesting evidence was already observed in literature for undoped TiO_2 nanoparticles and actually represents a hot topic (i.e. black titania) especially in the field of photocatalytic / water splitting processes [17]. In this framework, the evidenced darkening of the TiO_2 nanoparticles treated in reducing atmosphere is proposed to be likely connected to several reasons related to the formation of a disordered superficial layer surrounding the crystallized nanoparticles, characterized by the presence of a severe amount of oxygen vacancies and hydrogenated states, eventually resulting in the formation of in-gap states [17].

In order to in-situ visually monitor the darkening of the porous films when subjected to a crystallization process in vacuum atmosphere, an experimental setup with

a camera pointing on the surface of the samples was designed. Selected pictures of TaTO samples surface taken during the temperature heating ramp of a standard annealing cycle are reported in Figure 37 (ramp 10 °C/min). The darkening effect of the films is clearly visible for all the porous films, regardless of the different p_{O2} employed during the deposition process (p_{O2} = 5 – 15 Pa), while in the case of the compact sample (p_{O2} = 1 Pa) no darkening effect is reported (consistently with the results presented in Section 4.2).

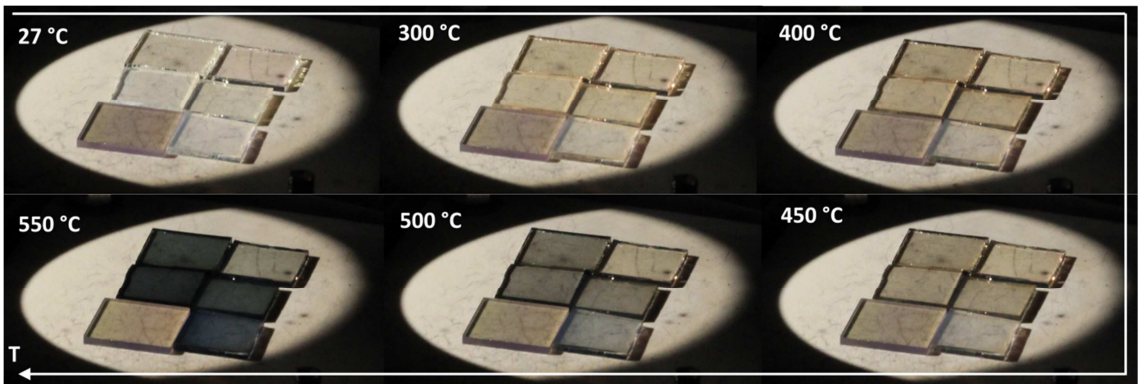

Figure 37 Pictures taken during the heating ramp of a standard crystallization cycle exploited in vacuum atmosphere of several TaTO samples (deposition pressure reported in the top left picture). On the top left corner, the corresponding temperature when the picture was taken is reported.

It is noteworthy that the darkening of the porous samples starts at very low temperatures (~ 300 °C) and increases gradually up to the dwell temperature of 550 °C. Moreover, we report the evidence that once reached the peak T, the color of the porous films is not changing anymore as a function of the dwell time, pointing out that this could be a very fast process (although we are aware that this represents just a visual / superficial evidence). As previously discussed in the case of the Raman spectra, it should be again remarked that also the darkening effect is not observed for all the vacuum annealing cycles, and we are still investigating on this aspect.

Due to the variability of the optical characteristics obtained after the annealing processes, in this section just the total transmittance spectra of the as deposited porous films is discussed. In particular, we noticed that the porous films are highly transparent in the whole λ range tested (see Figure 38). More interestingly, we report on the possibility to obtain a transmittance increment in the system soda-lime glass substrate + TaTO nanotrees with respect to the bare substrate (spectra reported in Figure 38 are not normalized with respect to glass).

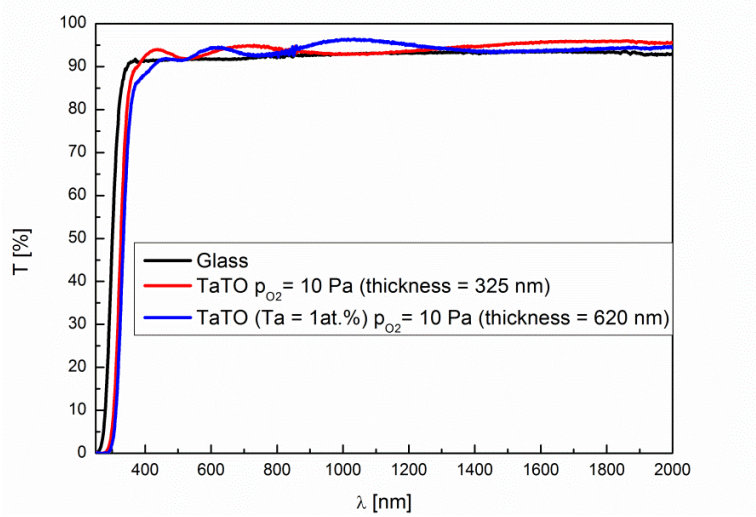

Figure 38 Total transmittance spectra of the bare glass substrate (black line) and not-normalized spectra of Ta:TiO_2 thin films with different thickness values (325 nm for TaTO – red line, and 620 nm TaTO with 1 at.% - blue line).

In particular, the minimum values of the thickness interference fringes for both the TaTO films deposited at p_{O2} = 10 Pa are shown to lay on the baseline of the glass while the maximum values result in higher values of transmittance for both the tested thicknesses of 325 nm and 620 nm. This result is still under investigation, but it is possible that the low density TiO_2 layer is ruling the determination of its refractive index, eventually resulting in an anti-reflective coating for the glass substrate. In the most simple approach, this would happen in a normal incident angle configuration (the light is impinging perpendicularly to the surface) when the refractive index of the TiO_2 layer results to be between those of air (n_0 ~ 1) and the soda-lime glass substrate (mean n_s ~ 1.5). As a matter of fact, it has been analytically estimated that the refractive index of nanotree-shaped TiO_2 films with very similar morphology can result in values of n as low as 1.28 (supplementary information in reference [112]).

4.3.3 Electrical properties

As already pointed out, it is not possible to determine the electrical properties of the nanotree-shaped hierarchically grown TiO_2-based films via a direct application of the electrical contacts on top of the film (conventional 4-point measurements approach). Moreover, the characterization of the cross-plane vertical conductivity is the most important value to be determined for the nanotrees: since they are intended for a photoanode application, the injected electrons in the TiO_2-based porous layer are taking

advantage of the vertically-oriented conduction path dictated by the film morphology. Two different approaches were employed in this work in order to try to evaluate the electrical properties of the nanotrees: (a) a direct and (b) a contactless measurement.

a) Direct resistance measurement: one possible approach would be to deposit the hierarchical film on a conductive substrate (which in principle could be made of the same material in our case, since the thin film in a compact form would effectively represent a TCO) to attempt an electrical contact between the top of the nanoporous structure and the bare conductive substrate, enabling the possibility to perform a resistance measurement. This approach has been recently used by our research group to attempt the measurement of the electrical properties of a porous film made of AZO [130]; micromanipulators were employed in order to minimize the contact area (20 – 30 μm^2). With this approach it was demonstrated that it is possible to extract a resistivity value for the nanostructured network considering the contact area of the tip as the effective section where the current flows (see Figure 39 (a) and (b)).

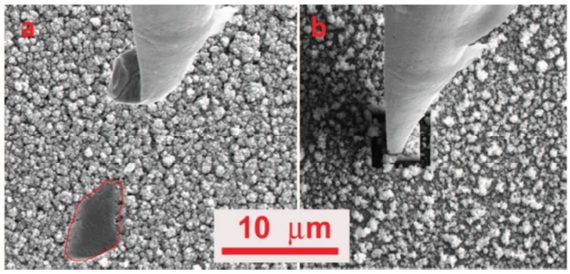

Figure 39 Top view of AZO porous film acquired with SEM. a) Image of the left trace by micromanipulator tip after an I-V measurement; b) SEM image of a tip contact in a delimited square region. Image taken from [130].

The limitation of this approach is connected to the intrinsic fragility of the porous network. In fact, the physical contact between the micromanipulator tip and the top of the AZO porous layer could result in the structural damage of the measured film (see Figure 39 (b)), and it is consequently difficult to state whether the measured resistance is intrinsically the one of the nanostructures or the one of the compacted network.

For this reason we attempted a different approach for the TiO_2-based nanotrees aiming to result in a less demanding measurement with respect to their intrinsic structural fragility. A 12 µm thick TaTO film was deposited at p_{O2} = 15 Pa and subsequently annealed in vacuum atmosphere with a fast cycle so to induce its

crystallization (SEM micrography reported in Figure 40 *(a)*). The surface of the film was subsequently mechanically scratched on top of a TEM copper grid characterized by a 8.5 μm wide metal network and ~ 30 μm sized voids (Figure 40 *(b)*). This resulted in the obtainment of single detached nanotrees, or bundles of them, on the surface of the metal grid network (Figure 40 *(c)*). The grid was subsequently reversed and fixed on an insulating mica substrate, and a thin layer of gold was evaporated on top of it (substrate maintained far from the evaporation source so to avoid the heating of the system). This procedure resulted in the obtainement of metal pads on the insulating substrate remarking the void shape of the TEM grid (i.e. its negative) which was subsequently removed (Figure 40 *(d)*).

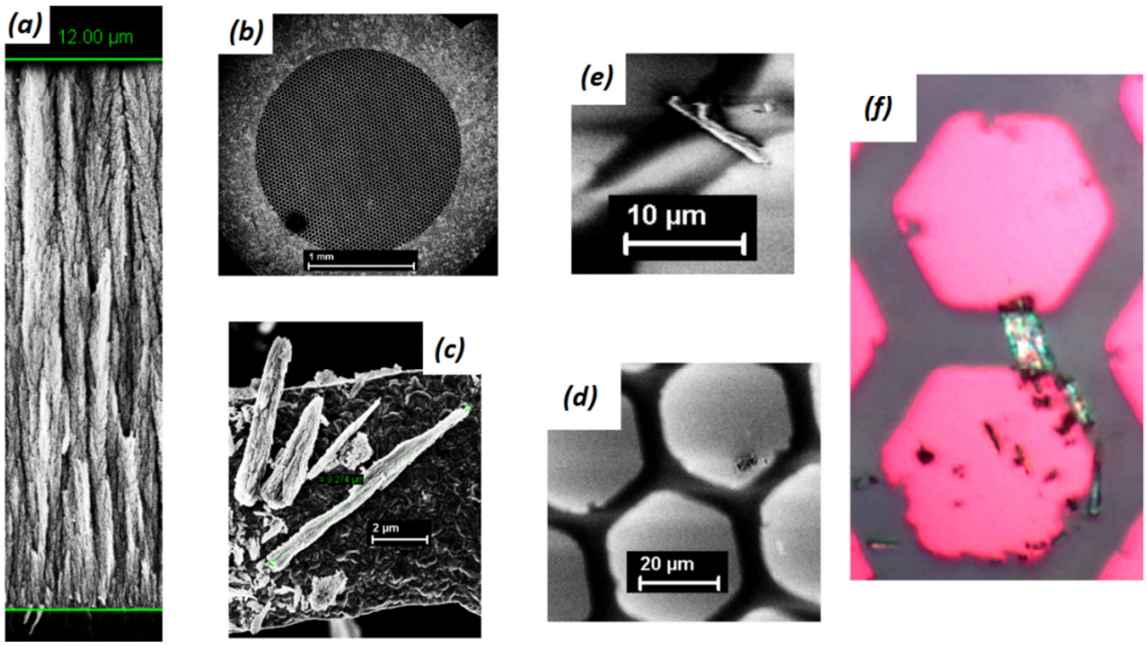

Figure 40 Steps for the obtainement of electrically contacted TaTO nanotrees: *(a)* vacuum annealed TaTO film deposited at p_{O2} = 15 Pa (SEM), *(b)* TEM Cu grid employed as a template for the scratching of nanotrees (SEM), *(c)* scratched nanotrees on the TEM grid network (SEM), *(d)* gold pads evaporated on top of a mica insulating substrate (SEM), *(e)* and *(f)* TaTO nanotrees constituting a bridge between the evaporated gold pads (SEM and optical microscope with polarized light).

The nanotrees which were randomly distributed on the surface of the metal grid network before the evaporation process (Figure 40 *(c)*), eventually resulted in an effective bridge connecting the gold pads (Figure 40 *(d)* and *(f)*). As it is visible from the otpical microscope image reported in Figure 40 *(f)*, the evaporated gold is superficially covering the nanotree far ends when bridging two separate pads, probably enabling a good electrical contact. The correct identification of the bridged metal pads

would allow to measure the I-V characteristic which should be intrinsically connected to the resistance of the nanotrees. Although this novel approach is really promising for the direct determination of the electrical properties of the nanotrees, a correct evaluation of the parameters involved in the measurement and in the samples preparation (e.g. determination of the nature of the electrical contact between the contacted metal pads, limitations in the applied voltage / current for the nanotree characterization, optimal thickness of the metal pads in order to obtain the best covering / contact of the nanostructure's far ends beneath them) are still under investigation and up to now it was not possible to obtain any reliable resistance value.

b) Contactless measurements: the investigation of cross-plane electrical transport properties of TiO_2-based nanotrees was performed through an indirect approach, based on Scanning Photo Electron Microscopy (SPEM) at the ELETTRA synchrotron facility of Trieste (ESCA microscopy beamline). This approach recently resulted in the conductivity evaluation of spatially separated GaAs nanowires [131] and consist in a contactless monitoring with photoelectron microscopy of the surface potential along the individual nanostructures thanks to the employement of an highly focused incident photon beam (spot of diameter smaller than 150 nm).

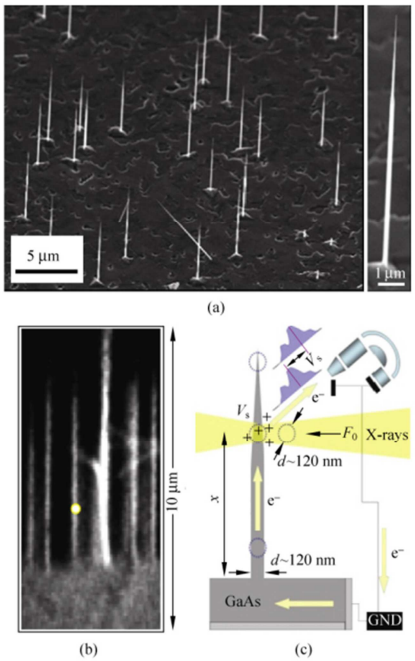

Figure 41 *(a)* SEM images of GaAs nanowires; *(b)* SPEM image obtained for Ga *3d* electron photoemission spectra; *(c)* schematic representation of the contactless set-up to monitor the evaluation of the surface potential V_S by collecting spectra from different points along the nanostructure. Picture taken from reference [131].

The basic principle of this technique consists in acquiring X-ray photoemission spectra (XPS) along the growth axis direction of the spatially separated nanostructures (see Figure 41 *(c)*) and monitoring the presence of a rigid energetic shift for XPS peaks. In fact, if the electrical conductance of the measured structures is too low to allow an easy electron flow from the substrate to the probed area, the photoemitted electrons are not effectively compensated, resulting in the build-up of a positive surface potential V_S. Consequently a rigid shift in the kinetic energy ΔE_k of the photoemitted electrons is recorded; the ΔE_k increases proportionally to the distance from the substrate *x*, according to the relation [131]

$$\Delta E_k = C \frac{x}{\sigma} A_x$$

where *C* is a parameter depending on the beam properties (photon flux, irradiated area, electron yield), σ is the electrical conductivity and A_x the cross section of the nanostructure at the distance *x* with respect to the substrate (estimated from SEM measurements). The ΔE_k expression implies that the limit in the measurable conductivity of the investigated nanostructure is connected to the energetic resolution of the measurement (low resistivity results in a complete recovery of the photoemitted electrons by the substrate leading to non-detectable shifts). In addition, this technique allows to obtain surface chemical information about the probed areas (i.e. from the analysis of XPS peaks).

A series of TaTO samples ~ 16 μm thick with a different doping amount (Ta = 0, 1, 5 ad 10 at.%) was deposited at room temperature on Si substrates (since the experiment requires the presence of a conducting substrate so to permit the compensation of the photoemitted electrons) at p_{O2} = 15 Pa, resulting in a very similar morphology (see Figure 42). We decided to study the electrical properties of this particular morphology because it is very similar to the one employed in the work made by R. Ghosh *et al.* in which it has been demonstrated that TaTO nanotrees with 1 at.% of extrinsic doping amount can result in an improved efficiency of DSSCs when employed as photoanodes [8].

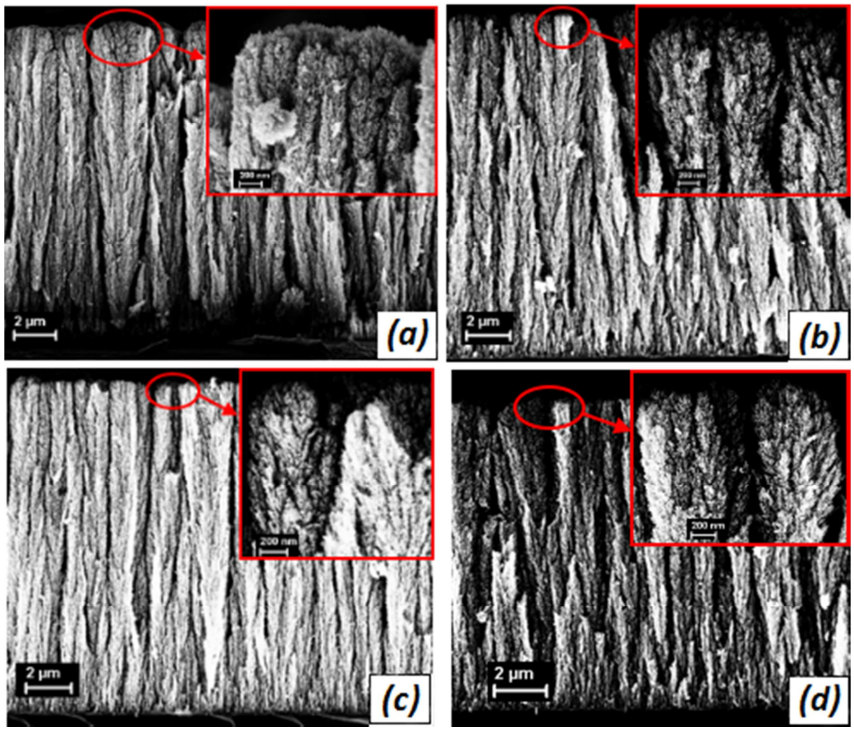

Figure 42 SEM picture of SPEM analyzed air annealed TaTO samples deposited at p_{O2} = 15 Pa with different doping amounts: Ta = 0 at.% *(a)*, 1 at.% *(b)*, 5 at.% *(c)*, 10 at.% *(d)*.

The possibility to obtain twin samples in the same deposition process allowed also to directly compare the effect of the annealing process and atmosphere. In particular SPEM measurements were performed on the highlighted samples in the table reported below.

Ta [%]	Amorphous	Air annealed	Air + vacuum annealed
0			
1			
5			
10			

The air annealing process employed a dwell time of 2 hours at 500 °C. In order to prevent the non-reproducibility of the vacuum annealing process (Section 4.3.1), we found that if the standard cycle is performed after a previous crystallization in air, the resulting Raman spectra of all the films show anatase peaks as intense as the ones obtained after the air annealing process, although still characterized by a

photoluminescence background (see Figure 43). We also report for these very thick films the presence of rutile (R) and brookite (B) peaks (dotted pink and yellow lines in Figure 43). Nontheless, the presence of these TiO_2 polymorphs should be limited to a very low amount with respect to the predominant anatase phase [118]. Nonetheless, it has been already reported that the increase of the oxygen background pressure during the PLD deposition process can eventually lead to the formation of secondary TiO_2 polymorphs after an annealing cycle performed in the range of 500 °C [110]. Moreover, no darkening effect was obtained for all the air + vacuum annealed samples (see Section 4.3.2).

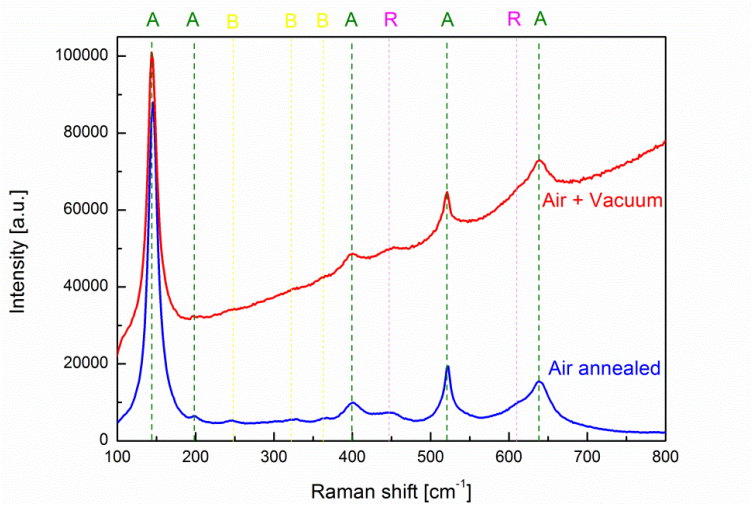

Figure 43 Raman spectra acquired for the SPEM analyzed undoped TiO_2 films *(a)* air annealed, and *(b)* air + standard vacuum annealed. Letters refer to A = anatase, B = brookite, R = rutile.

The TiO_2-based films on Si substrates were cleaved and mounted on a sample holder in order to expose to the photon flux the cross section of the film (see Figure 44).

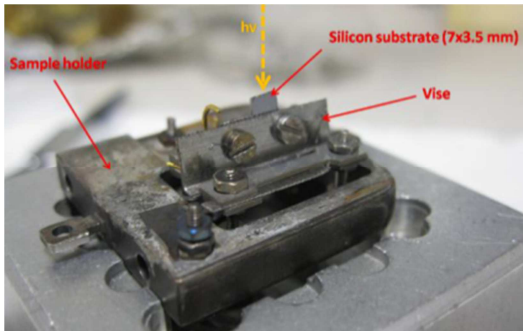

Figure 44 Mounting system and configuration employed for the SPEM investigation.

The X-ray beam produced by synchrotron source is focused on the sample cross section by means of Fresnel zone-plate optics; the spot diameter can be as small as 150

nm. We operate our experiments in an imaging spectromicroscopy mode: a chosen area of the sample is mapped by collecting photoelectrons in a previously chosen kinetic energy range while scanning the sample with respect to the microprobe. In particular we studied the acquired maps for Ti 2p and O 1s peaks. These images were acquired with a dwell time of 50 ms, so to avoid a chemical modification of the sample. The photoemission spectra were recorded at a fixed photon energy of 675 eV; all the reported spectra are plotted as a function of the kinetic energy (KE), so the photon energy is essential in order to derive the corresponding binding energy scale (BE).

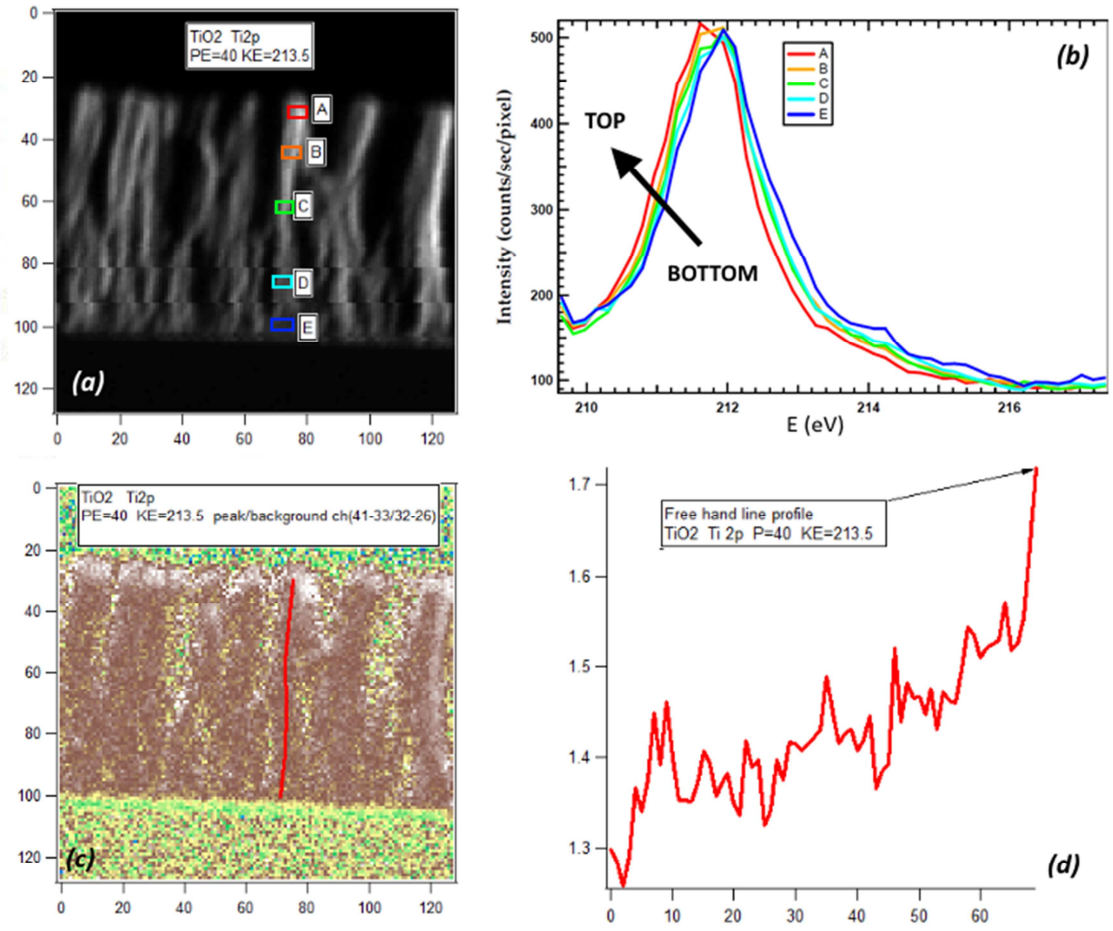

Figure 45 *(a)* SPEM map of the cross section of the TiO_2 sample acquired from the Ti 2p core level; pixels are reported on the x- and y-axis; the letters and the colored rectangles are representing the map regions where the spectra shown in *(b)* where extracted. *(c)* Map resulting from the ratio between the chosen energetic intervals of the peak (peak/background) from the spectra of the original map *(a)*; the red line is representing the free hand line profile which has been extracted in *(d)*. On the x-axis of *(d)* pixels are reported (0 = bottom of the nanostructure), while on the y-axis the intensity of the peak/background is reported.

The possible presence and evaluation of an energetic shift along the single nanostructures was evaluated according to the following procedure:

- Acquisition of a SPEM chemical map corresponding to the XPS peak of an element (e.g. Ti 2p); an example is reported in Figure 45 *(a)*, where the numbers on the x- and y-axis represent the number of pixels: every pixel represents the area of the XPS spectrum for the selected energetic interval corresponding to the chosen peak element under investigation (resulting from the 50 ms impinging of the probe spot of ~ 150 nm).
- It is possible to extract an average spectrum selecting an area in the map. Comparing the spectra derived from different x positions along a single nanostructure it is possible to evaluate the presence of a top-to-bottom energetic shift (see Figure 45 *(b)*). Moreover, from these spectra it is possible to identify the presence of a chemical change along the nanostructure (which would change the shape of the acquired peaks).
- If the shape of the peaks is reasonably similar (i.e. no significant chemical variations are recorded), it is possible to highlight the energetic shift by properly choosing an intensity ratio between two fixed energetic intervals of the peak (e.g. left part of the peak/beakground) so to obtain larger peak/background intensities when moving from the bottom to the top of the nanostructures in the case of a recorded energetic shift. In this way, the energetic shift can be graphically shown as reported in Figure 45 *(c)*, i.e. as a map in which the different intensity of the colors represents the different resulting peak/background intensity.
- By the identification of a line profile along a single nanotree, it is possible to plot the peak/background intensity as a function of the distance from the substrate (see Figure 45 *(d)*). The peak/background intensity can be converted in an energetic scale (eV) under the hypothesis of spectra having the same shape, i.e. chemical composition (evaluation of the top-to-bottom energetic shift from spectra extracted from the original map, like red-blue spectral shift in Figure 45 *(b)*), so evidencing and estimating the presence of the ΔE_k as a function of the distance from the substrate.
- We obtained different maps for every element (e.g. Ti 2p) in different regions of the sample, and we averaged the obtained line profiles over several different nanostructures so to obtain more reliable data.

The complete analysis of all the collected data is presented in the master thesis of E. De March ("Contactless Measurement of Electrical Properties in TiO_2-based Tree-like Nano and Mesostructures", Politecnico di Milano, academic year 2014-2015) in which I was involved as co-supervisor. The results obtained for the Ti 2p signal for all the tested TiO_2-based samples crystallized in air atmosphere are reported in Figure 46: an almost linear behavior is recorded from the mean values of the analyzed samples.

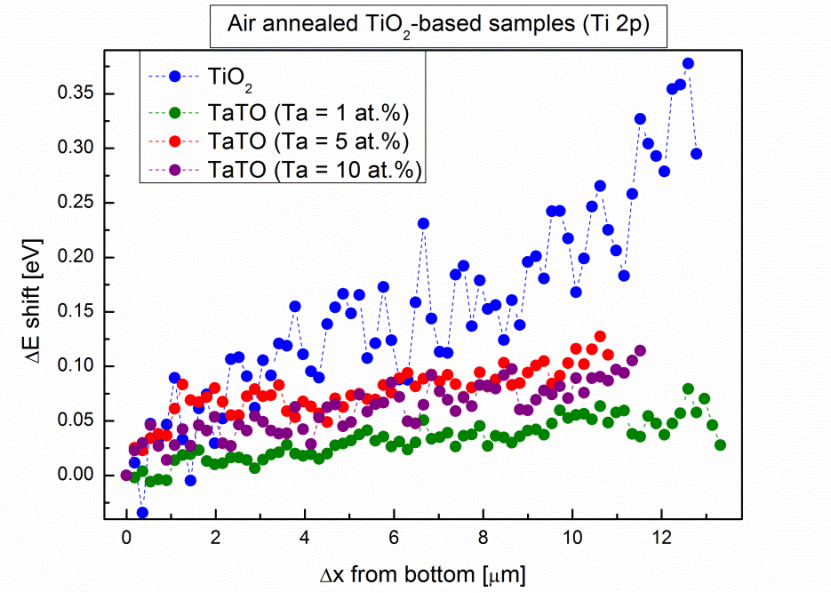

Figure 46 Mean energetic shift evaluated for air annealed TiO_2-based samples starting from single nanotrees as a function of the distance from the bottom of the analyzed structure.

Assuming that the larger the slope of the almost-linear recorded behavior (Figure 46), the more resistive are the nanotrees, it is possible to state that the air annealed Ta-doped nanotrees are intrinsically more conductive with respect to the undoped TiO_2 ones for all the tested compositions. Nonetheless, an internal trend among the TaTO samples can be underlined: in particular, the TaTO sample with Ta = 1 at.% shows the lowest resistance, while the recorded slope for Ta = 5 and 10 at.% is almost equal.

This highlights a different behavior with respect to the compact films, for which the optimum doping concentration for obtaining the best electrical properties was found to be 5 at.%. Nevertheless, it is possible that in the case of nanotree structures the best amount of extrinsic ionized defects is reduced due to the tens of nanometer sized particles which are constituting the building blocks of the porous films (with respect to the tens of micrometer sized grains of the compact layers, see Section 4.2.1). Moreover, these results are in line with the increased photocurrent in DSSCs obtained by R. Ghosh

et al. for air annealed hierarchically grown Ta:TiO_2 (Ta ~ 1 at.%) photoanodes with respect to undoped TiO_2 ones [8], pointing towards the possibility to tune the functional properties of this material even in the nanostructured form.

Up to now, the analysis was limited to the Ti 2p elemental maps. For the working principle of this technique, the presence of a rigid energetic shift in the acquired spectra should be present for all the analyzed XPS peaks. Nevertheless, the results of the SPEM measurements performed on O 1s did not always show the same trend as the ones showed for Ti 2p. In particular, while in the case of the air annealed TiO_2 sample a very good agreement with respect to the Ti 2p results was found, for all the Ta-doped samples no energy shift for O 1s was clearly detectable (not shown). We are still investigating on this point, but there could be several reasons related to this evidence. The most probable one is connected to the sensibly larger O 1s energetic spectra with respect to the Ti 2p one, which leads to a more difficult evaluation of the energetic shift especially in the case of low ΔE. In fact, the O 1s shift was detected just for the most resistive sample (undoped TiO_2, see Figure 46).

Moreover, following the same experimental procedure we also investigated the effect of different thermal treatments on TiO_2 and TaTO (Ta = 5 at.%) nanotrees. This analysis is limited to the Ti 2p maps for the aforementioned reasons.

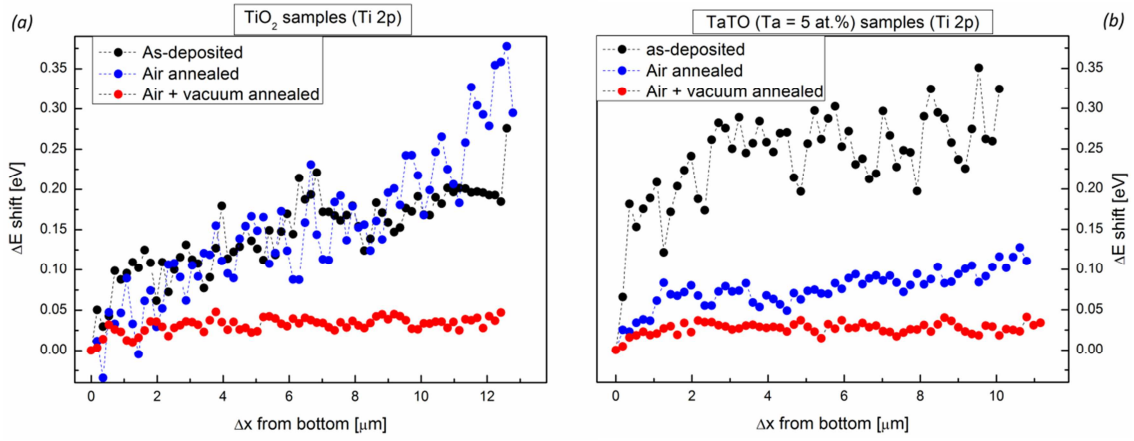

Figure 47 Mean energetic shift evaluated for TiO_2 *(a)* and TaTO *(b)* nanotrees exposed to different treatments as a function of the distance from the bottom of the analyzed structures.

The data for the as deposited samples (black lines in Figure 47 *(a)* and *(b)* for TiO_2 and TaTO respectively) show a similar slope for the undoped and the doped sample. This is consistent with a similar resistance of these two amorphous nanostructers, as already discussed for the case of the compact non crystallized films

(see Section 4.2.1). While the air annealing treatment results in an almost unchanged XPS shift trend for the undoped films with respect to the as-deposited one, in the case of TaTO the recorded energetic shift along the axis of the nanostructures is significantly diminished compared to the amorphous one (blue lines in Figure 47 *(a)* and *(b)* for TiO_2 and TaTO respectively). The different behavior between the crystallized undoped and TaTO could suggest a certain degree of extrinsic doping activation in the air annealed nanostructured films which was not detectable in the case of the compact morphology (air annealing resulted in non-electrically measurable samples, see Section 4.2.1). Nonetheless, the most intriguing result is related to the possibility to reduce the resistance of both the undoped and doped nanotrees when the air annealing process is followed by a vacuum standard one (red lines in Figure 47 *(a)* and *(b)* for TiO_2 and TaTO respectively): both the spectra show a flat ΔE profile as a function of Δx, indicating that the nanotrees became too conductive for the sensitivity of the technique (intrinsically limited by the energetic resolution).

This last evidence is similar with the one obtained for vacuum annealed TiO_2-based compact films, but most importantly opens up to the possibility to test this kind of thermal treatment for DSSC TiO_2 photoanodes, in order to study if the increased conductivity of the porous network could result in an overall increase of the photovoltaic cell efficiency. On the other hand, it should be considered that a too large concentration of charge carriers in the photoanode could lead to an increase of the recombination phenomena with photogenerated holes (intimate contact between photoactive material and porous TiO_2). Nonetheless, we point out that the proved ability to change in a controlled manner the electrical properties of TiO_2-based porous films, constitutes an extremely appealing ability which could be exploited in the framework of several fields (see Chapter 2).

All the considerations made so far are valid in the framework of an internal comparison among the studied samples. Nonetheless, it is possible to obtain a rough estimate of the total resistance of the "average" tree-like structures. The values of the total resistance can be computed by taking the maximum ΔE recorded for a sample showing a trend as a function of Δx (top of the nanostructure) and dividing it by the electron current value which is required to compensate for the photon-induced charging (experimentally measured I = 60 pA). The resistance of the air annealed TiO_2 nanotrees was estimated to be around 5 GΩ, while the one of air annealed TaTO with 1 at.%

doping was one order of magnitude lower (~ 0.5 GΩ). Intermediate and very similar values were calculated for TaTO with Ta = 5 and 10 at.% (~ 2 GΩ).

Finally, also unfocused survey XPS spectra were acquired to monitor the Ta relative content with respect to Ti in the doped films. By considering the area ratios between Ta 4f and Ti 2p signals for the doped samples it has been found that TaTO with a nominal Ta content of 10 at.% has almost twice the Ta content of TaTO with Ta = 5 at.%, while the tantalum content of TaTO with nominally 1 at.% (obtained by laser ablation of a heterogeneous target, see Section 3.2) was evaluated in the range of 1.28% and 1.44% (considering as exact reference either the value obtained for the 10 at% or for the 5 at.% respectively). Nevertheless, it should be pointed out that an absolute quantitative analysis is extremely difficult in absence of a standard sample reference.

4.4 TiO_2-based multi-layers

After the obtainment of the functional properties control of compact and porous layers, the possibility to experimentally synthesize multi-layer structures was investigated. This is a very interesting opportunity, since it could result in the ability of obtaining an all TiO_2-based TCO + selective layer + photoanode for solar cell applications; this novel multi-layer architecture could represent the possibility to properly investigate the role played by the interfaces at the anode side of the device, eventually leading to an overall efficiency improvement of the cell (see Section 2.1.3).

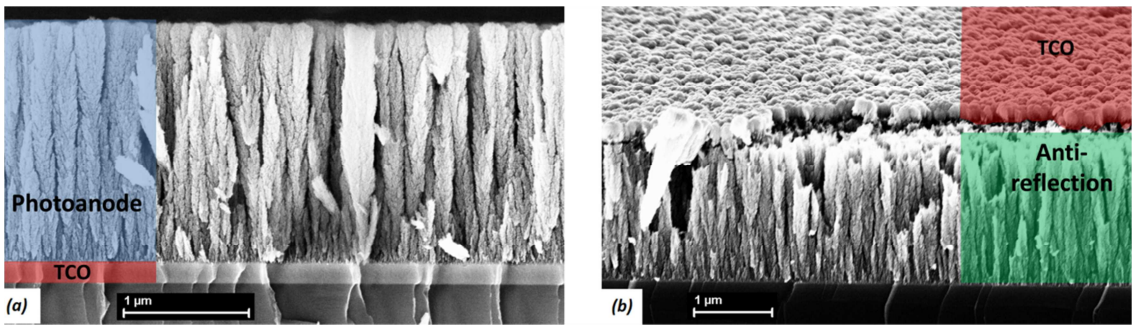

Figure 48 Multi-layer TaTO architectures obtained by PLD at room temperature in a single deposition process. *(a)* Compact + porous multi-layer, *(b)* inverted morphology. The colors are highlighting the different layers, underling the active role they should play in the structure.

Exploiting the high control level achieved in the PLD deposition of TiO_2-based thin films, we demonstrated the possibility to obtain several multi-layer configurations.

In Figure 48 *(a)* an obtained compact + porous TaTO architecture is reported. This structure was achieved by changing the p_{O2} during a single deposition process: the 150 nm thick compact layer was deposited at a p_{O2} = 1.25 Pa, while rising the p_{O2} up to 10 Pa, the 1.8 μm thick porous layer was obtained on top of it. This particular architecture could represent an effective TCO + photoanode suitable for liquid DSSC (due to the absence of the selective layer, see Section 2.1.1). On the other hand, as previously demonstrated in Section 4.3.2, the porous layer could also act as an anti-reflection coating with respect to the glass substrate (see Figure 38). In this framework has to be intended the reversed architecture proposed in Figure 48 *(b)*, in which the thickness of the thin films was maintained equal to the previous configuration, but the porous layer is placed beneath the compact one; in this case the nanotree-shaped layer is employed with the aim of obtaining an overall increase of the total transmittance, while the compact one is intended to work again as a TCO. An evident increase of the top compact layer roughness is noticeable with respect to the one directly deposited on the bare glass substrate; this could clearly affect its conductivity in view of a TCO application. Although we are not aiming to clarify this aspect in this work, it is worth noting that similar porous + compact AZO structures studied in our research group could result in acceptable electrical properties of the TCO even if characterized by a high roughness [47].

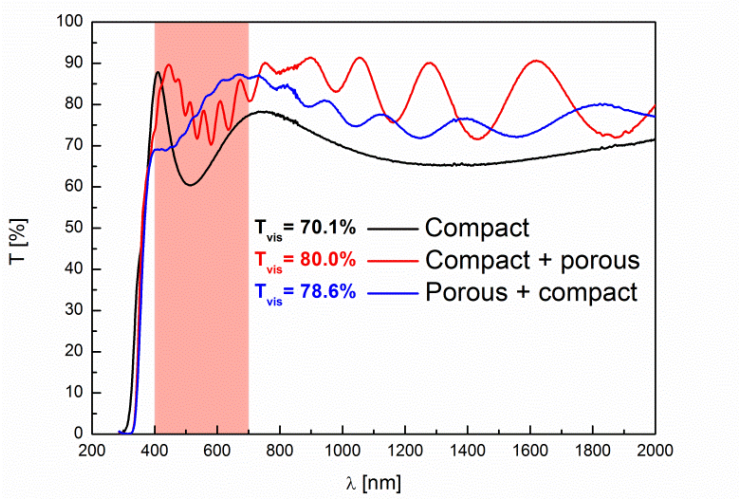

Figure 49 Total transmittance spectra (normalized with respect to the glass substrate) of a TaTO single compact layer (150 nm, black line), a compact + porous (150 nm + 1.8 μm, red line, SEM structure shown in Figure 48 *(a)*) and a porous + compact (1.8 μm + 150 nm, blue line, SEM structure shown in Figure 48 *(b)*) multi-layer architecture. The highlighted part in the graph is the visible region of the spectra, for which the T*vis* is reported for all the structures.

The total transmittance spectra of the multi-layer structures shown in Figure 48 have been acquired and compared with that of an as deposited TaTO single compact layer with the same thickness of 150 nm (see Figure 49). Both the amorphous multi-layer structures show a considerable transmittance improvement with respect to the single compact layer (T_{vis} data reported in Figure 49). As previously proposed in Section 4.3.2, this evidence should be related to an antireflection effect obtained with the porous TiO_2 based nanotree layer: in fact, also in the case of the TaTO compact + porous architecture the decreased mass density of the nanostructured layer should result in a lower refractive index with respect to the one of the compact film beneath it.

Nonetheless, we demonstrated that it is possible to obtain for the double layer compact + porous a significant transmittance improvement with respect to the single TaTO compact layer (T_{vis} from 80.1% to 87.8%) even after a single standard vacuum annealing process (see Figure 50). Nonetheless, we notice that the transmittance improvement after the reducing thermal cycle is strictly related to the possibility of avoiding the already discussed darkening of the porous structure (see Section 4.3.2).

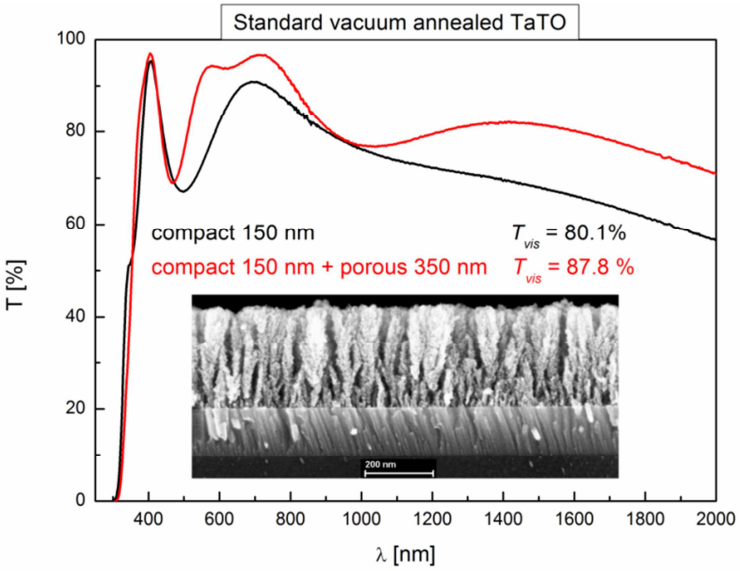

Figure 50 Total transmittance spectra (normalized with respect to the glass substrate) of a standard vacuum annealed TaTO multi-layer structure (red line, corresponding SEM of the crystallized structure reported as an inset) and of a single compact layer with the same thickness (black line).

Up to this point, just double layer structures intended as a TCO + photoanode suitable for liquid electrolyte DSSCs were shown. Nonetheless, it was already pointed out that in new generation solid state DSSCs as well as in perovskite based solar cells, the presence of a selective layer able to avoid an intimate contact between the TCO

layer and the photoactive material is mandatory in order to reduce the recombination processes in the device (see Section 2.1). In this framework, we took advantage of the possibility to obtain a very different charge carrier density in standard vacuum annealed TaTO layers while maintaining the same compact morphology (see Section 4.2.2). This allowed us to obtain all-TaTO double layer compact morphology structures characterized by a *(i)* high charge carrier density (n ~ 10^{21} cm^{-3} for p_{O2} = 1 Pa) in the 150 nm thick bottom TCO, while *(ii)* low charge carrier density (n ~ 10^{19} cm^{-3} for p_{O2} = 1 Pa) on the ~ 30 nm thick top selective layer (see compact layers in Figure 51). Moreover, the very same charge carrier density of the selective layer was obtained for an undoped TiO_2 top layer (n ~ 10^{19} cm^{-3} for p_{O2} = 1.4 Pa). This could represent the opportunity to directly investigate the effect of the extrinsic dopant in a double layer TaTO + TiO_2 architecture with almost the same electrical properties.

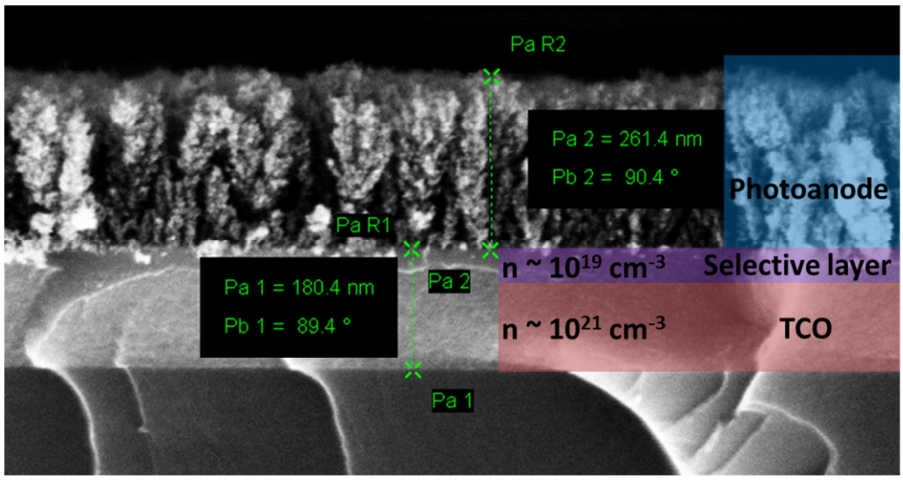

Figure 51 Triple-layer TiO_2-based structure currently under test for perovskite solar cells.

Finally, it was also possible to obtain with the same approach a triple-layer structure (see Figure 51) in which the photoanode porous layer (p_{O2} = 15 Pa) is added on top of the TCO + selective layer structure. All the possible combinations (TaTO homostructure / TaTO + TiO_2 heterostructures) are currently under testing for different architectures of perovskite solar cell devices (flat / sensitized) in the framework of the established collaboration with the research group of A. Abbotto (università Milano Bicocca).

5. Investigation of structure and defects in TiO_2-based thin films

In this chapter an investigation of the physical reasons behind the highlighted ability of finely tuning the electrical properties of TaTO compact films is presented. XRD and Raman spectroscopy have been performed on several TiO_2-based samples in order to correlate their structural (Section 5.1) and vibrational properties (Section 5.2) obtained for different synthesis conditions with the resulting functional properties, and thus with the presence of ionized defects in the anatase crystal structure. Moreover, the Positron Annihilation Spectroscopy (PAS) technique is exploited on doped and undoped films treated in different atmospheres in order to shed light on the point defects involved in determining their electrical properties (Section 5.3).

5.1 Doping-induced structural effects: unit cell parameters

A set of crystallized TaTO samples deposited at different p_{O2} and a nominally undoped TiO_2 film as reference were characterized through XRD (PANalytical X'Pert PRO MRD high-resolution X-ray diffractometer, using CuKα1 radiation, λ = 0.15406 nm, selected by a two-bounce Ge monochromator) measurements performed in grazing

incident angle configuration (fixed incident angle ω = 5°)[*]. This scan configuration has been chosen because of the resultant higher diffraction peak intensity with respect to the θ-2θ scan due to an higher interaction with the thin films.

The results presented in this section were published in a peer reviewed journal [116].

5.1.1 Determination of unit cell parameters from XRD

Following the procedure reported in this Section and proposed by our collaborator D. Chrastina for our experimental data analysis [132], it was possible to evaluate the anatase tetragonal cell parameters from the XRD peak positions.

For a given incidence angle ω and scattering angle (between incident and scattered beams) of 2θ, the scattering vector $\vec{q} = (q_x, q_z)$ is given by[†]

$$q_x = {}^{2}/_{\lambda} \sin\theta \sin(\theta - \omega) \ , \quad q_z = {}^{2}/_{\lambda} \sin\theta \cos(\theta - \omega)$$

$q_y \neq 0$ would represent "out of plane" scattering and is not considered. Since for a polycrystalline film with no preferred grain orientation the incidence angle ω is irrelevant (because crystals are present in the sample with every possible orientation), which means that only 2θ is relevant, resulting in

$$q_{(hkl)} = {}^{2}/_{\lambda} \sin\theta_{(hkl)}$$

for the lattice planes (*hkl*), and since we are using $1/\lambda$ for the length of the wavevector, the spacing $d_{(hkl)}$ of the lattice planes in real space is simply

$$d_{(hkl)} = {}^{1}/_{q_{(hkl)}}$$

In a tetragonal crystal with lattice parameters a, $b = a$, and c, the spacing of the (*hkl*) planes is given by

$$\frac{1}{d_{(hkl)}} = q_{(hkl)} = \sqrt{\left(\frac{h}{a}\right)^2 + \left(\frac{k}{a}\right)^2 + \left(\frac{l}{c}\right)^2}$$

so for the relevant (101) and (200) reflections in the TiO_2-based films investigated in this work, we have

[*] XRD measurements performed by D. Chrastina (L-NESS, Dipartimento di Fisica, Politecnico di Milano, Italy).

[†] In some conventions $2\pi/\lambda$ is used instead of $1/\lambda$ for the length of the wavevector of the x-ray radiation.

$$\frac{1}{d_{(101)}} = q_{(101)} = \sqrt{\left(\frac{1}{a}\right)^2 + \left(\frac{1}{c}\right)^2} = \sqrt{\frac{1}{a^2} + \frac{1}{c^2}}$$

$$\frac{1}{d_{(200)}} = q_{(200)} = \sqrt{\left(\frac{2}{a}\right)^2} = \frac{2}{a}$$

meaning that *a* can be found as $2/q_{(200)}$ and *c* can be found from

$$\frac{1}{c} = \sqrt{q_{(101)}^2 - \frac{1}{a^2}} = \sqrt{q_{(101)}^2 - \frac{q_{(200)}^2}{4}}$$

5.1.2 Effect of a different p_{O2} at a fixed Ta doping concentration

In Section 4.2.2 and 4.2.5 we have shown that the electrical properties of conducting TaTO thin films can be changed in a wide range of resistivity values. More in detail this ability was found to be tightly connected to the fine tunability of their charge carrier concentration. Nevertheless, two distinct phenomena should be considered to be responsible of this behavior after their crystallization in reducing atmosphere. On one side *(i)* we demonstrated how it is possible to change *n* due to the different nominal concentration of the extrinsic dopant (see Figure 35); in this case the concentration of Ta in Ti substitutional sites [$Ta_{Ti}^{\bullet}$] could well explain the order of magnitude obtained for the concentration of electrons released in the conduction band after their crystallization in vacuum, under the hypothesis of an extremely high dopant activation efficiency (see Section 2.3.3). On the other hand *(ii)* we showed that once the Ta nominal concentration is fixed (Ta = 5 at.%), the *n* of the vacuum annealed TaTO films can be tuned in the same range (10^{19} – 10^{21} cm^{-3}, see Figure 32) as a function of a different p_{O2} employed during the deposition process. In particular we focus on *(ii)*: it is plausible to assume in this case that the reported trends in the TaTO electrical properties are related to a more complex defect chemistry. In fact, since O-richer conditions are not expected to lead to the segregation of nondoping Ta_2O_5 phases in TaTO, or to sensibly affect the [$Ta_{Ti}^{\bullet}$], the coupling between a decreasing concentration of $V_O^{\bullet\bullet}$ and / or the occurrence of a certain amount of *p*-type electron-killer defects like V_{Ti}'''' and / or O_i'' associated to an increasing oxygen partial pressure employed during the deposition process could be responsible of the obtained trend of *n* (see Section 2.3.2).

Since the concentration of the above mentioned defects should vary in a rather wide range in order to be compatible with the observed decrease of *n* with respect to the TaTO film which showed the best electrical properties ($n \sim 10^{21}$ cm^{-3}), it could be possible to detect a corresponding variation in the anatase unit cell parameters. For this reason the anatase tetragonal cell parameters *a* and *c* for the same set of standard vacuum annealed TaTO samples discussed in Section 4.2.2, which were deposited in a p_{O2} range 1 – 2.25 Pa, has been calculated. In Figure 52 *a* and *c* for TaTO vacuum annealed films (red squares) and undoped TiO_2 (blue circles) are reported as a function of their measured charge carrier concentration ((a) and (c)), as well as their oxygen deposition pressure ((b) and (d)), in which also the parameters referred to the air annealing process are reported (empty red square and blue circle for TaTO 1.25 Pa and TiO_2 respectively).

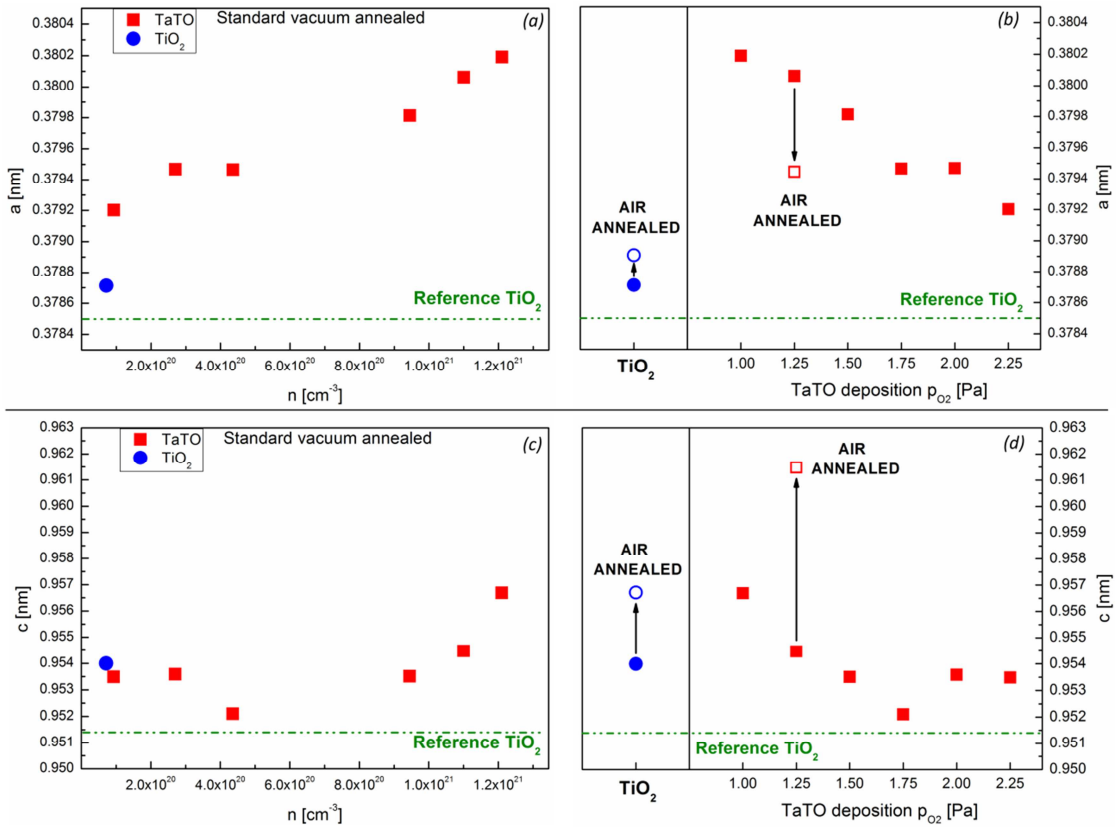

Figure 52 Anatase cell parameters (*a* in (a) and (b), and *b* in (c) and (d)) evaluated for TiO_2 (blue circles) and TaTO (red squares) annealed with a standard cycle in vacuum (filled) and air (TiO_2 and 1.25 Pa TaTO, empty). The samples parameters are plotted as a function of *n* ((a) and (b)) as well as the p_{O2} ((b) and (d), reproduced from [116]). The green dotted lines represents the reference values of cell parameters for a nominally pure anatase TiO_2 [12].

A general comparison between doped and undoped vacuum annealed films shows a systematic larger value of the *a* parameter in TaTO, while *c* is found to be similar with respect to the measured TiO_2 film, except at large charge carrier density for which a small enlargement is recorded. This is reasonably explained by Ta incorporation in Ti sites, as the ionic size of Ta^{+5} (0.064 nm) is slightly larger than that of Ti^{+4} (0.061 nm) [133]. The recorded larger increase of *a* with respect to *c* due to doping incorporation in the anatase cell has been theoretically predicted by Kamisaka *et al.* [134] for Nb-doped TiO_2, which should result in a very similar effect due to the same ionic radius of Ta (Nb^{+5} atomic radius 0.064 nm).

Focusing on the TaTO series of samples, it is possible to notice that both *a* and *c* parameters are slightly decreasing (approaching the values for the vacuum annealed TiO_2 cell) with increasing p_{O2} (Figure 52 (b) and (d) respectively). A specular trend is identified when plotting the unit cell parameters as a function of the measured charge carrier density (Figure 52 (a) and (c)), as a result of the evidenced strict connection between *n* and p_{O2} (see Figure 26). These observations could be in first instance related to a slight decreasing amount of $V_O^{\bullet\bullet}$ when the p_{O2} is increased (with a consistent lowering of the charge carrier concentration). Nevertheless, when the crystallization process is performed in air, which is known to result in a highly insulating film (see Section 4.2.1), for TaTO (p_{O2} = 1.25 Pa, Figure 52 (b) and (d)) there is an increment in *c* coupled with a decrease in *a*, while for the nominally undoped TiO_2 crystallized in air a larger value of both the unit cell parameters is detected. This is highlighting *(i)* that the observed trend between the unit cell parameters and *n* for vacuum annealed TaTO deposited at different p_{O2} is not solely explainable by the presence of a different concentration of $V_O^{\bullet\bullet}$ among the films, and *(ii)* that the drastic change of the conductivity from vacuum to air annealed recorded for both TiO_2 and TaTO could be related to the formation of different point defects when the extrinsic dopant is present.

Moreover, regarding point *(ii)* the change of the unit cell parameters between the air annealed TaTO film and the vacuum annealed one is in line with the presence of a significant amount of $V_{Ti}^{''''}$ and / or O_i'' (discussed for TaTO and TNO respectively in [135] and [134]), which in both cases should theoretically result in a significant enlargement of the unit cell in the *c* direction while weakening the *a* component (see Figure 52 (d) and (b) respectively).

Finally, regarding point *(i)* we note that the possibility that the evidenced trend for the conducting TaTO films would be related to the reduction of the $Ta_{Ti}^{\bullet}$ concentration when increasing p_{O2}, is in contrast with the experimental data published by T. Hitosugi *et al.*, where it is shown that while increasing the Ta content in epitaxially grown TaTO films, a significant increase of *c* with an almost unchanged value of *a* is recorded [61].

The results of this structural investigation are not providing definitive evidences for the identification of the point defects involved in the control of the electrical properties of the material, but are clearly highlighting a complex defect chemistry ruled by a nonobvious interplay among extrinsic and intrinsic dopants (e.g. oxygen – titanium – tantalum).

5.2 Vibrational properties of doped anatase

Since the concentration of defects in the crystal lattice is large enough to result in a detectable variation of the anatase cell parameters, it is plausible to assume that the vibrational properties of the crystal could be affected as well. For this reason a large amount of TiO_2-based samples has been analyzed via Raman spectroscopy trying to correlate their anatase active modes with the electrical properties. In this framework, in Section 5.2.1 a brief introduction on the acquired knowledge on Raman spectroscopy of anatase TiO_2 is given, so to properly discuss the results obtained in this study (presented in Section 5.2.2).

5.2.1 Raman spectroscopy of TiO_2-based materials

The primitive triclinic unit cell of anatase titanium dioxide is composed by two TiO_2 units (6 atoms), resulting in 15 optical modes (Γ_{opt}) and 3 acoustic modes. The optical modes at the Γ point are classified for symmetry (space group D_{4h}^{19} - $I4_1/amd$):

$$\Gamma_{opt} = A_{1g} + A_{2u} + 2B_{1g} + B_{2u} + 3E_g + 2E_u$$

where A_{2u} and the 2 E_u are IR active modes, B_{2u} is a silent mode, and A_{1g}, the 2 B_{1g} and the 3 E_g are Raman active [136]. In Figure 53 a typical Raman spectra obtained for an air annealed TiO_2 film is reported, with the nominal positions of the 6 Raman active modes (dotted lines) in good agreement with the experimental evidence.

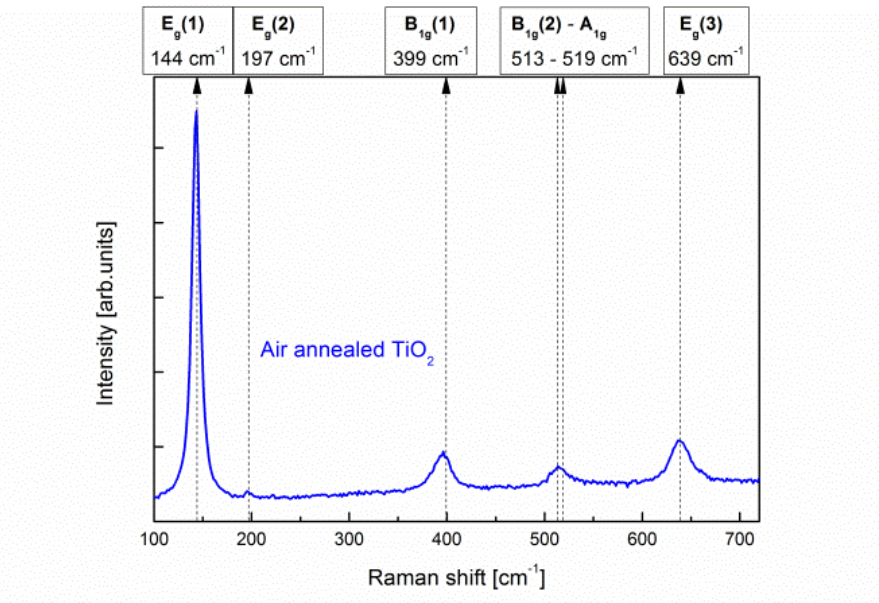

Figure 53 Raman spectra of an air annealed TiO_2 sample. The dotted line are referring to the nominal positions expected (according to reference [137]) for the Raman active modes of the anatase phase (reported on top).

The 3 E_g modes involve atom displacements perpendicular with respect to the *c*-axis, while the others are parallel. Most of the modes involve both Ti and O atom displacements. In particular, several literature works focused on the most intense $E_g(1)$ mode. Its peak frequency, width and shape have been shown to be affected by various factors:

- non-stoichiometry [138, 139];
- extrinsic doping [140, 141];
- disorder induced by minority phases [141];
- thin film thickness and substrate [142];
- high pressure induced by the surrounding atmosphere and temperature [143];
- phonon confinement effects in nanoparticles [118, 144, 145].

For what is concerning our study on polycrystalline TiO_2-based samples, due to the fact that they are all deposited on soda-lime glass substrates with a comparable thickness (which is for almost all of them around 150 nm), characterized by single phase atanase grains of several micrometers, and that the Raman spectroscopy has been always performed at room temperature in ambient pressure, we will just consider the non-stoichiometry and the presence of the extrinsic dopant for the determination of the $E_g(1)$ mode position and width.

Although there is a large amount of literature focusing on TiO_2, just a few works thoroughly studied the other Raman active modes. Among them, it is useful for the discussion of our results to mention an interesting investigation on the vibrational properties of the anatase phase on samples of TiO_2 with different oxygen isotopes (^{16}O, ^{17}O,^{18}O) [146, 147]. The Raman spectra acquired in that work for $Ti^{16}O_2$, $Ti^{17}O_2$ and $Ti^{18}O_2$ samples is reported in Figure 54.

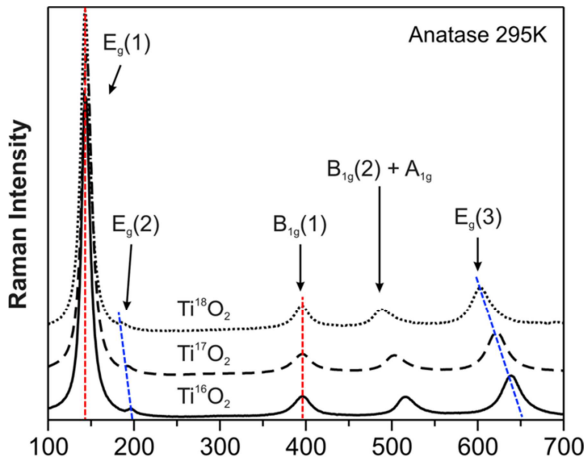

Figure 54 Raman spectra acquired at T= 295 K of anatase $Ti^{16}O_2$, $Ti^{17}O_2$ and $Ti^{18}O_2$. The dotted blue lines are evidencing the shifted Raman active modes, while the red ones are evidencing the almost unchanged peak positions. Picture taken from reference [147] and modified.

The significant blue shift evidenced for $E_g(2)$ and $E_g(3)$ (blue dotted lines in Figure 54) are highlighting the fundamental role played by oxygen in determining their position. Unfortunately, the peak A_{1g} which is predicted to be the only Raman active mode to be related to pure oxygen vibration (symmetry does not allow the movement of Ti atoms) is overlapped to $B_{1g}(2)$ and its exact determination and study is a complicated matter [146]. Nonetheless, other two interesting evidences are reported in the work: both $E_g(1)$ and $B_{1g}(1)$ modes show a negligible shift induced by the oxygen isotopes (red dotted lines in Figure 54). This behavior was consistent with theoretical calculations, which were predicting a displacement pattern with $E_g(1)$ and $B_{1g}(1)$ symmetry, so that the oxygen atoms should not vibrate at all [146]. Nonetheless, while the $B_{1g}(1)$ could be considered as a pure Ti-atoms vibration, $E_g(1)$ should be treated more carefully in light of the previous reports on the shift of this Raman active mode, which was experimentally showed to be connected to oxygen stoichiometry deviations [138, 139]. It is consequently reasonable to assume that oxygen could play a minor, but not negligible role for the $E_g(1)$ mode peak position.

5.2.2 Study on the vibrational properties of doped TiO_2

We now present the analysis and discussion of a large amount of Raman spectra acquired for our doped and undoped compact films. All the TiO_2-based thin films were analyzed by micro-Raman measurements (Renishaw In Via spectrometer with Ar+ laser, λ = 514.5 nm – power on sample 1 mW, so to avoid power-induced modifications). In order to correctly determine the Raman active modes position and width we performed lorentzian fits on the analyzed peaks.

a) Effect of the extrinsic dopant: since we are investigating the vibrational properties of doped and undoped TiO_2 thin films deposited and crystallized in different atmospheres, in first instance we try to highlight the role of Ta as a Ti substitutional in the anatase cell (i.e. extrinsic dopant). As it has been already discussed in Section 4.2.2 and 4.2.5, once found the optimal deposition p_{O2}, the vacuum annealed TaTO films show a charge carrier density in the same range of the nominal dopant concentration, coupled with a large electron mobility (whose highest value is dependent on the Ta atomic content, see Figure 35). These O-poor synthesis conditions, apart from the probable presence of a certain amount of V_O, should result in a low concentration of V_{Ti} in the anatase crystal (based on defect chemistry considerations presented in Section 2.3.2). As we just discussed in Section 5.2.1, the Raman active mode $B_{1g}(1)$ is thought to be ruled by pure Ti-atoms vibration, and consequently represents a good opportunity to study the effect of a different concentration of Ta_{Ti} in the crystal matrix of anatase.

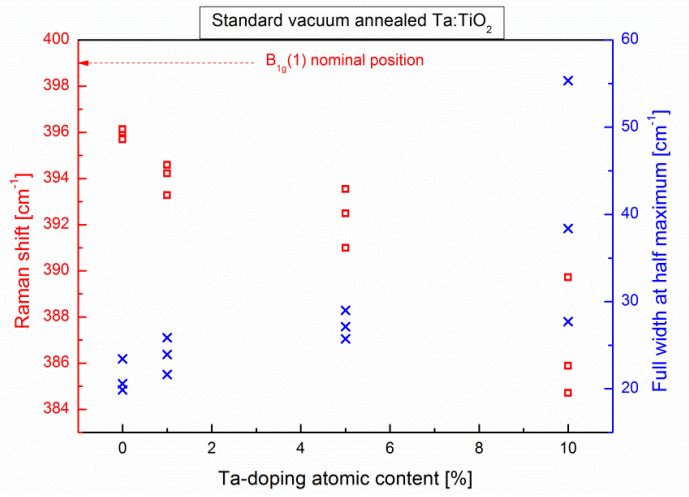

Figure 55 Peak position (red squares) and width (blue crosses) of the Raman active mode $B_{1g}(1)$ for standard vacuum annealed TaTO films deposited at optimal p_{O2} as a function of a different Ta-doping content.

According to Figure 55 it is possible to evidence a $B_{1g}(1)$ red shift ($-\Delta\nu$) as the nominal atomic content of Ta is increased: while the undoped TiO_2 samples are approaching the expected nominal position, the presence of Ta as Ti substitutional significantly alters the Ti-atoms vibration, leading to a maximum $-\Delta\nu > 10$ cm^{-1} for Ta = 10 at.% (red squares). Consistently with the inclusion of an increasing concentration of extrinsic dopant in the matrix (i.e. inducing crystalline disorder), the peak width evaluated at half maximum is shown to increase.

Nonetheless, an interesting feature appears for the overdoped TaTO composition (Ta = 10 at.%): just in presence of such a high extrinsic dopant concentration, an additional component is appearing at lower wavenumbers (~ 350 cm^{-1}) with respect to $B_{1g}(1)$. For this reason the determination of position and width of this Raman active mode in the case of overdoped samples always required a lorentzian fit with a double peak component (see Figure 56). To the best of our knowledge no Raman active modes in that particular region could be reasonably assigned to different TiO_2 polymorphs or Ta-O-Ti phase segregations. Since this characteristic feature is detected just in presence of a high Ta doping amount, and regardless of the employed atmosphere during the crystallization process (e.g. vacuum or air), it is possible to hypothesize the activation of a Ta-Ti vibration inside the anatase crystal, whose significant red shift with respect to the pure Ti-Ti vibration could be ascribed to the mass change between Ta and Ti.

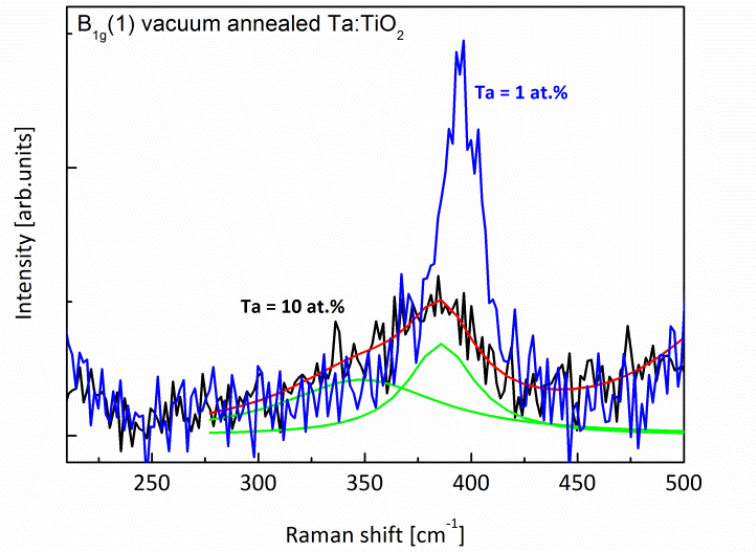

Figure 56 Typical Raman peaks $B_{1g}(1)$ obtained for standard vacuum annealed TaTO films with Ta = 1 at.% (blue line) and Ta = 10 at.% (black line). In the case of the overdoped sample, the peak has always to be fitted with a double component (green lines beneath the black spectra).

The analysis of the collected data on the peak $B_{1g}(1)$ is well in line with the presence of the Ta extrinsic dopant as a Ti substitutional in the anatase lattice (Ta_{Ti}).

The analysis on peak position and width for the TiO_2-based samples deposited at the best p_{O2} was performed also for the other Raman active modes. In particular in Figure 57 and Figure 58 the results for the Raman active modes $E_g(1)$ and $E_g(3)$ respectively are reported.

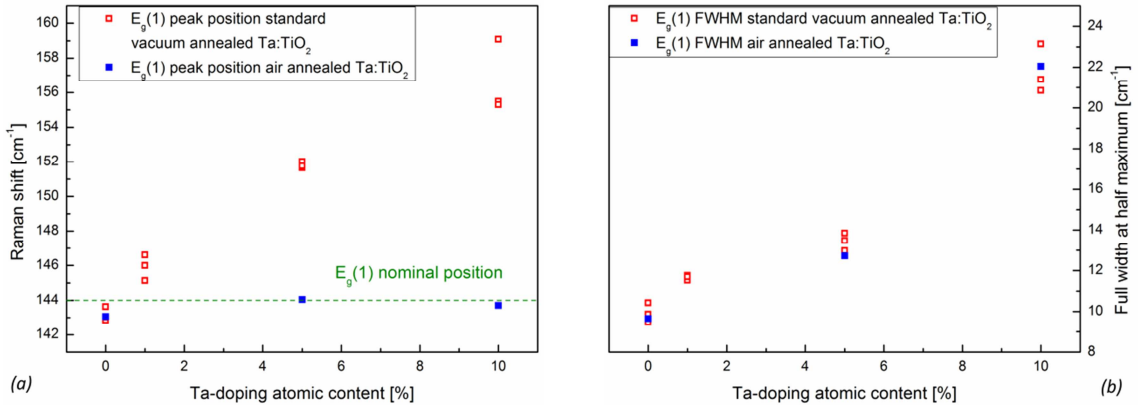

Figure 57 *(a)* Peak position and *(b)* width of the Raman active mode $E_g(1)$ for standard vacuum annealed (red squares) and air annealed (blue squares) TaTO films deposited at optimal p_{O2} as a function of a different Ta-doping content. The nominal position of $E_g(1)$ is represented as a dotted green line *(a)*.

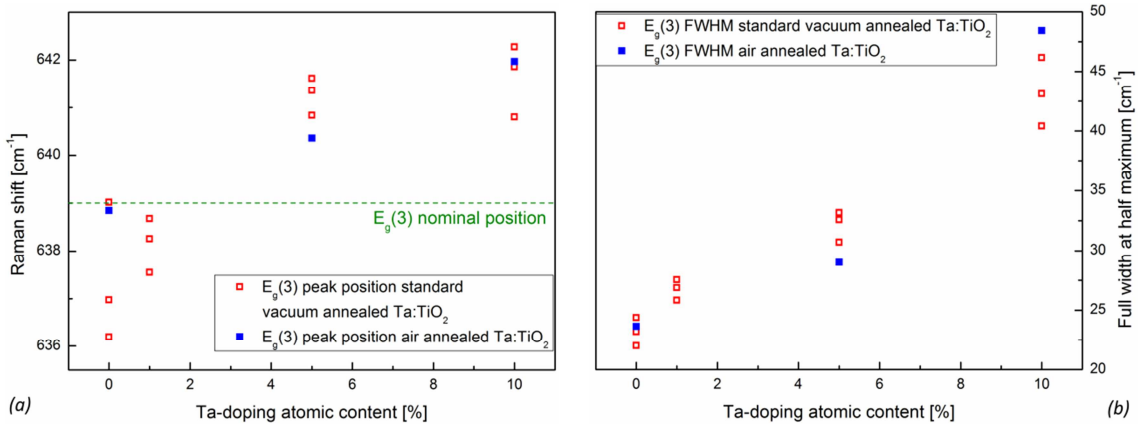

Figure 58 *(a)* Peak position and *(b)* width of the Raman active mode $E_g(3)$ for standard vacuum annealed (red squares) and air annealed (blue squares) TaTO films deposited at optimal p_{O2} as a function of a different Ta-doping content. The nominal position of $E_g(3)$ is represented as a dotted green line *(a)*.

Regarding the $E_g(1)$ mode, the peak position of the vacuum annealed films shows an increasing blue shift (maximum $+\Delta v$ ~ 15 cm^{-1}) while passing from the undoped to the overdoped composition (Figure 57 *(a)*). As previously evidenced in the case of $B_{1g}(1)$ (see blue squares in Figure 56), also in the case of the $E_g(1)$ mode the

FWHM is increasing together with the Ta content (red squares in Figure 57 *(b)*). Nonetheless, a peculiar feature appears for the $E_g(1)$ mode when comparing the vacuum to the air annealing treatment performed on twin samples: differently from the vacuum annealed films (red squares in Figure 57 *(a)*), the peak position of the air annealed ones is always approaching the nominal expected value without evidencing a trend as a function of the extrinsic dopant concentration (blue squares approaching the reference green line in Figure 57 *(a)*). However, the peak width of the air annealed films is following the very same trend of the vacuum annealed ones (Figure 57 *(b)*). It is thus possible to highlight that while the increasing amount of extrinsic dopant in the lattice is coherently leading to a higher structural disorder which is independent with respect to the employed annealing atmosphere (i.e. similar FWMH tendency for vacuum and air crystallized samples, see Figure 57 *(b)*), the position of the $E_g(1)$ peak is blue-shifting together with its nominal Ta concentration only when the TaTO films are crystallized in reducing atmosphere (red squares in Figure 57 *(a)*). This is a surprising result, since the significant peak shifts evidenced for the vacuum annealed samples with respect to the air annealed ones are clearly not accompanied by a higher structural disorder (i.e. it is shown to be just related to the amount of extrinsic dopant in the lattice).

The behavior of the $E_g(2)$ mode is found to be very similar to the one evidenced for $E_g(1)$ with respect to the peak position and the annealing atmosphere as a function of the different amount of Ta (not shown). Nonetheless, an exact determination of the peak width and position results more complicated with respect to the other modes due to its lower intensity (see Figure 53).

The $E_g(3)$ mode is showing a considerably smaller blue shift of the peak position (maximum $+\Delta\nu \sim 5$ cm^{-1}) with respect to $E_g(1)$. Nonetheless, even in this case it is possible to highlight the presence of a trend as a function of the nominal Ta atomic content (Figure 58 *(a)*). Moreover, also in this case the width of the peak is clearly related to the different amount of extrinsic dopant regardless of the crystallization atmosphere (Figure 58 *(b)*). Nevertheless, no significant difference in the peak position is recorded between the vacuum and air annealed films, which are in this case following the same trend (red and blue squares respectively in Figure 58 *(a)*). This represents another interesting indication: it should be reminded in fact that the $E_g(3)$ mode was found to be the most affected Raman active mode with respect to the presence of oxygen isotopes in the crystal (see Section 5.2.1), pointing to a probable high sensitivity

to the oxygen stoichiometry. Under this hypothesis, the lack of a significant difference for the $E_g(3)$ peak position of vacuum and air annealed TaTO samples would indicate a negligible variation of the oxygen stoichiometry. Nonetheless, it should be considered that the effect of the presence/absence of oxygen vacancies in the crystal lattice of the TiO_2-based films could result in a very different vibrational behavior with respect to the mass change of the O atoms (obtained via the substitution of ^{16}O with ^{17}O and ^{18}O isotopes).

In this framework, it would have been extremely interesting to study the behavior of the A_{1g} mode which is predicted to be related to pure oxygen-atoms vibration, but unfortunately its superposition with $B_{1g}(2)$ did not allow the deconvolution of the two separate contributions (see Section 5.2.1). For this reason these two peaks are not studied in this work.

It is worth to highlight that the red and blue shift discussed for the $B_{1g}(1)$ and E_g Raman active modes respectively, are consistent with what one would expect from the phonon-band dispersion relations of anatase TiO_2 calculated by density functional perturbation theory [136].

b) Oxygen deposition pressure – Raman shift relation: after the study of TaTO samples with different doping content, it is here presented a thorough investigation on optimally doped TaTO films (Ta = 5 at.%) deposited at different oxygen background pressure. It has been widely discussed how p_{O2} could be a fundamental parameter in controlling the formation of point defects in this material (see Section 5.1.2), giving rise to the possibility of finely controlling the electrical properties in vacuum annealed films (4.2.2). The Raman active modes of TaTO 150 nm thick films vacuum and air annealed were studied with respect to peak position and width (evaluated at half maximum) as a function of p_{O2}. In Figure 59 the results obtained for $E_g(1)$, $E_g(2)$ and $E_g(3)$ are reported. The absolute positions and width referred to the $B_{1g}(1)$ peaks are not presented since several vacuum annealed TaTO samples resulted in a drastic reduction of its intensity, leading eventually to the complete disappearing of this Raman active mode, while the remaining modes were not affected. This point is currently under investigation, and it will be not discussed in this work. Also the A_{1g} and $B_{1g}(2)$ modes are not shown since it was not possible to deconvolve their separate contributions.

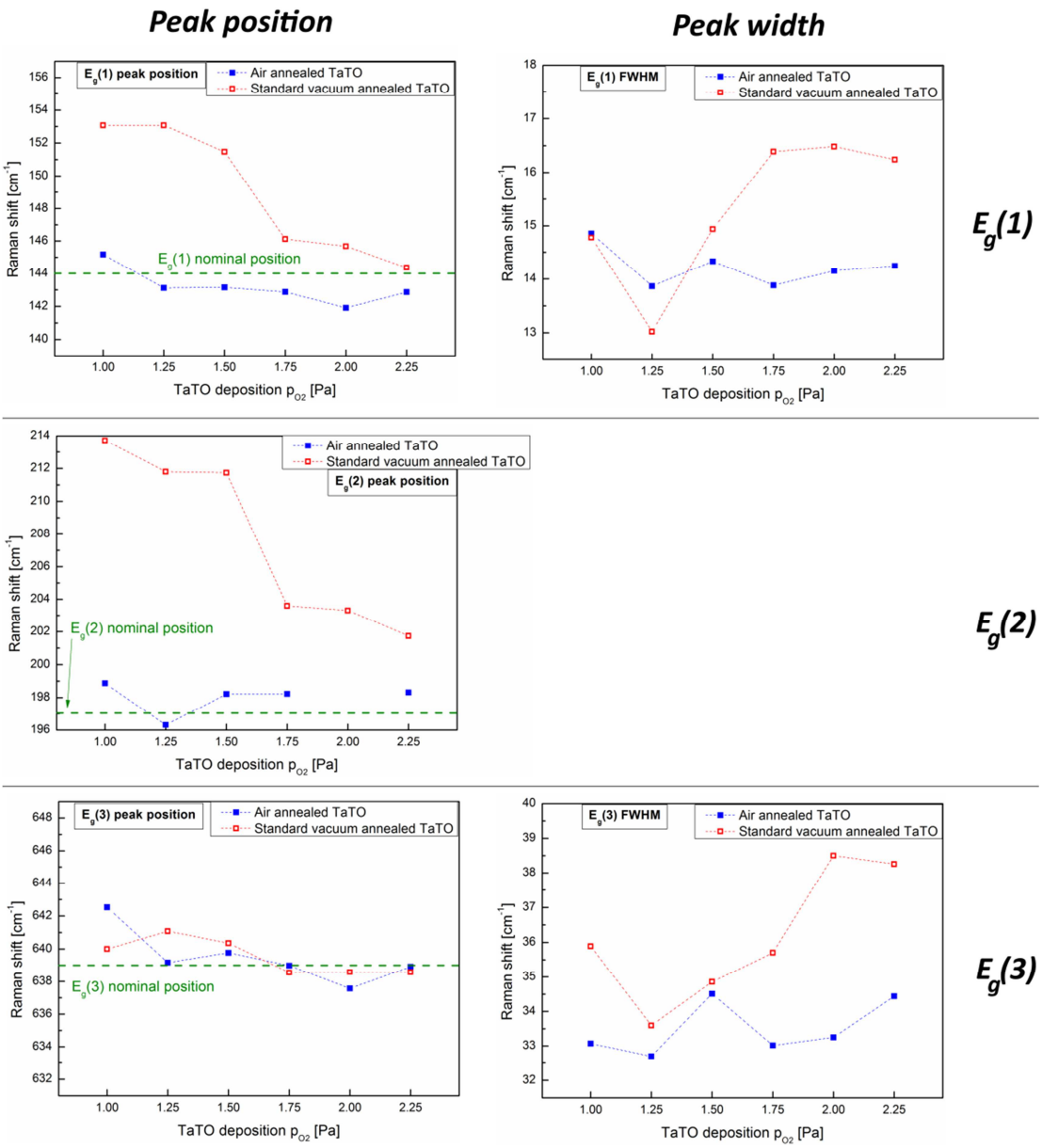

Figure 59 Peak position (left column) and width (right column) of $E_g(1)$ (first line), $E_g(2)$ (second line) and $E_g(3)$ (third line) Raman active modes for standard vacuum (red squares) and air (blue squares) annealed TaTO samples as a function of the deposition p_{O2}. In the case of $E_g(2)$ only the peak position is reported, due to the difficulties in determining the peak width (low intensity mode).

The position of the $E_g(2)$ mode is sensibly affected by the p_{O2} in the case of the vacuum annealed TaTO films (blue shift, maximum $+\Delta\nu \sim 12$ cm^{-1} in the analyzed set of samples), while the air annealed ones (blue squares) are approaching the nominal expected value (2nd row in Figure 59). This behavior is very similar to the one obtained for this Raman active mode while varying the Ta doping concentration. Nevertheless, for this peak, due to its very low intensity and proximity to the most intense $E_g(1)$ mode,

it has not been possible to reliably obtain the peak width, and for this reason is not reported in Figure 59.

$E_g(1)$ shows a very similar trend with respect to the $E_g(2)$ mode (Figure 59 1st row). In particular a significant blue shift is recorded in its peak position (maximum $+\Delta\nu \sim 9$ cm^{-1}); again in accordance with the data collected for TaTO samples with different doping amount the air annealing process results in no evident shift with respect to the nominal peak position. Nonetheless, it is noteworthy that in the case of a deposition $p_{O2} > 1.5$ Pa the $E_g(1)$ peak of the vacuum annealed TaTO films is considerably enlarged with respect to the corresponding air annealed ones. This is underling a very different behavior with respect to the TiO_2-based thin films deposited at optimal p_{O2} (which is around 1 - 1.25 Pa for all the doping compositions, see Section 4.2.5): in this case in fact it has been previously shown that the peak width is just determined by the Ta concentration and no variations were recorded as a function of a different annealing atmosphere (see Figure 57 *(b)*). This could be a definitive indication of a significant increment of defects in the anatase lattice while increasing the p_{O2} for vacuum annealed TaTO, i.e. leading to an increased local lattice disorder.

Also the analysis of the $E_g(3)$ Raman active mode (Figure 59 3rd row) is well in line with the above mentioned hypothesis: the peak width of the vacuum annealed TaTO films is shown to increase in a very similar way with respect to $E_g(1)$ for $p_{O2} > 1.5$ Pa, while no significant increment is recorded for the corresponding air annealed samples. Moreover it is worth to note that, as in the case of the optimally deposited samples with different Ta nominal concentration, the $E_g(3)$ peak position is not substantially affected by the oxygen deposition pressure or the annealing atmosphere: for all the analyzed samples it is approaching the nominal $E_g(3)$ position.

c) Charge carrier concentration – Raman shift relation: up to now the peak position and width of the Raman active modes for anatase TiO_2-based thin films have been just discussed as a function of synthesis conditions (e.g. p_{O2} and annealing atmosphere) and of a different extrinsic dopant concentration. Nonetheless, it has been widely discussed as these parameters are of paramount importance in determining the functional properties of this materials. A particular focus is now made on the connection between the electrical properties and the Raman shift.

As it has been previously discussed, in the case of $E_g(1)$ and $E_g(2)$ modes a blue shift is recorded just for vacuum annealed TaTO samples; this shift was shown to be

strictly related *(i)* to the nominal extrinsic dopant concentration (increasing $+\Delta v$ while Ta content is increased, see Figure 57 *(a)*), and *(ii)* to the oxygen partial pressure employed during the deposition process (at a fixed Ta nominal at.%, increasing $+\Delta v$ while p_{O2} is decreased, see Figure 59 1st and 2nd rows). At the same time, the corresponding air annealed TaTO $E_g(1)$ and $E_g(2)$ modes were shown to always approach the nominal peak position independently from both the extrinsic dopant concentration and the deposition p_{O2}.

In this framework, it is possible to underline a strong similarity with the charge carrier concentration recorded for the vacuum annealed TaTO thin films: in fact, *(i)* when the Ta concentration is increased *n* is found to proportionally increase (for samples deposited at the best p_{O2}, as previously evidenced in Figure 35), and *(ii)* when for a fixed nominal Ta content the p_{O2} is decreased *n* is found to systematically increase (as previously shown in Figure 26). Moreover, in the case of the air annealed samples it is plausible to assume that the resulting insulating character is strictly connected to a marked decrease of the charge carrier density (although the air annealed samples resulted to be too insulating to be measured with our experimental setup, see Section 4.2.1).

Based on the highlighted parallelism between the measured charge carrier density and the recorded $E_g(1) - E_g(2)$ peak shifts, a wide amount of conducting TiO_2-based samples has been analyzed via Raman spectroscopy as a function of:

- different extrinsic dopant concentration (0 – 1 – 5 – 10 at.%);
- different dopant (Ta and Nb – TaTO and TNO respectively); the 150 nm thick TNO films (fixed nominal Nb concentration = 5 at.%) were deposited via sputtering technique on unheated soda-lime glass substrates at a different p_{O2} and subsequently vacuum annealed by S. Nakao (Kanagawa Academy of Science and Technology – KAST, Kawasaki 213-0012, Japan) in the framework of a scientific collaboration with T. Hitosugi (Advanced Institute for Materials Research - AIMR, Sendai 980-8577, Japan);
- different p_{O2} during the room temperature deposition process;
- different annealing cycles (standard vacuum or H_2-based, fast vacuum, ultra-fast UFA in H_2 or N_2-based atmospheres – which will be presented in Chapter 6).

It was decided for this study to just consider the peak position of the most intense $E_g(1)$ mode, although a very similar characterization could be obtained also with $E_g(2)$. For all

these different samples, in Figure 60 the $E_g(1)$ peak position is plotted as a function of their correspondent experimentally measured charge carrier density.

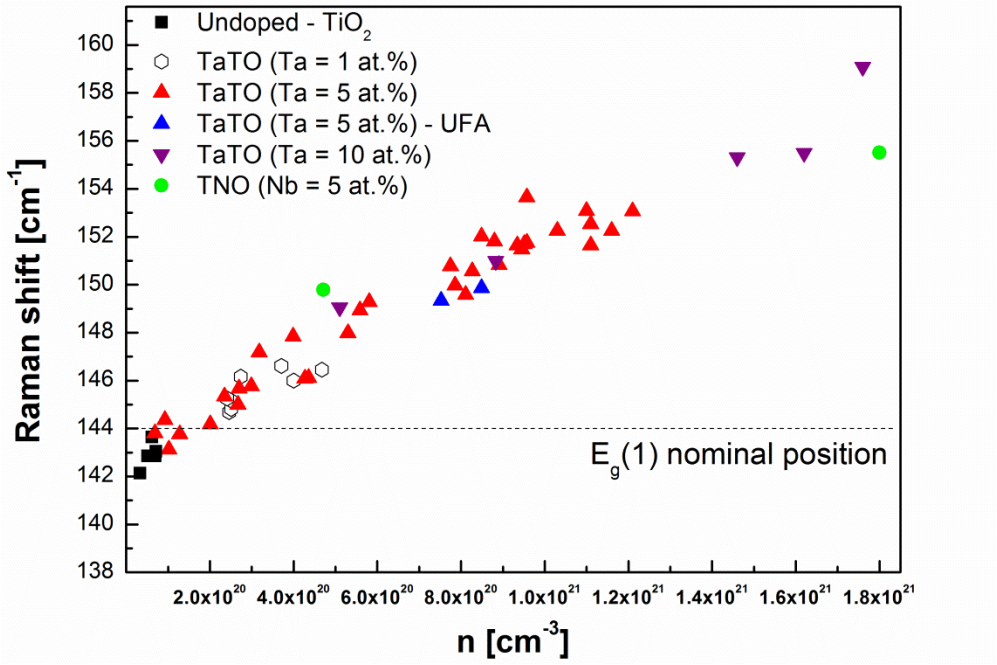

Figure 60 Raman peak position of the $E_g(1)$ anatase mode as a function of the correspondent charge carrier density measured for the thin films.

As it is possible to note from Figure 60 an extremely solid relation has been found between the $E_g(1)$ peak position and n. It is worth to highlight that the evidenced trend is:

- independent with respect to the extrinsic doping amount;
- independent with respect to the adopted extrinsic dopant (although just for two TNO samples it has been possible to obtain n);
- independent with respect to the performed annealing cycle and atmosphere (with the strict condition of obtaining measurable electrical properties);
- almost linear for $n \leq 10^{21}$ cm^{-3}, while it seems to flatten for higher charge carrier concentrations.

The full understanding of this experimental guess is still under debate. Nevertheless, it is clear that this robust trend is strictly connected to the defect chemistry of the material. In particular, due to the independent behavior with respect to the extrinsic dopant concentration, it can be proposed that the presence of other defects (e.g. oxygen and titanium stoichiometry) and their possible interplay/ordering in the anatase lattice is ruling this trend.

The results presented in this section will be soon submitted to a peer review journal.

5.3 Point defects investigation via positron annihilation spectroscopy

Up to now several experimental data regarding the optical, electrical, structural and vibrational properties have been discussed and linked together in light of a complicated role of the defect chemistry evidenced in TiO_2-based films. Nevertheless a precise determination of the point defects involved has not been possible. In order to collect more information on this issue, Positron Annihilation Spectroscopy (PAS) measurements performed in Coincidence Doppler Broadening (CDB) were made for TaTO as well as for TiO_2 films. It has to be remarked that the PAS experiments have been carried out by R. O. Ferragut (L-NESS, Dipartimento di Fisica, Politecnico di Milano, Italy). The interpretation of the results presented in this section should be considered as preliminary, and is still matter of internal debate.

5.3.1 Basic principles of PAS technique for point defect determination

The positron e^+ is the antiparticle of the electron. It has an electric charge of + 1 e (where e is the electron charge), a spin of ½ and the same mass as the electron. The annihilation event between e^- and e^+ is associated to the emission of 2 γ-rays of 511 keV. In the experimental setup used for the exploited CDB technique 2 high purity germanium detectors (HPGe) characterized by a high energetic resolution are facing each other while the analyzed sample is placed in the middle of them. Sample and HPGe detectors are maintained in a fixed position during the experiment and annihilation events are recorded in coincidence by them (see Figure 61).

The photon energy in the detector reference system depends on the relative motion between the center of mass of the $e^- - e^+$ annihilation event and the detector itself. The longitudinal component $p_L$of the electron-positron momentum along the direction of emission of one of the annihilation photons gives rise to the Doppler shift $\Delta E = p_L c/2$ in the photon energy recorded by the detectors. The main contribution to $p_L$comes from the electron motion, and for this reason the shape of the broadened

annihilation line spectrum provides direct information on the momentum distribution of the electrons encountered by the positron in the sample [148].

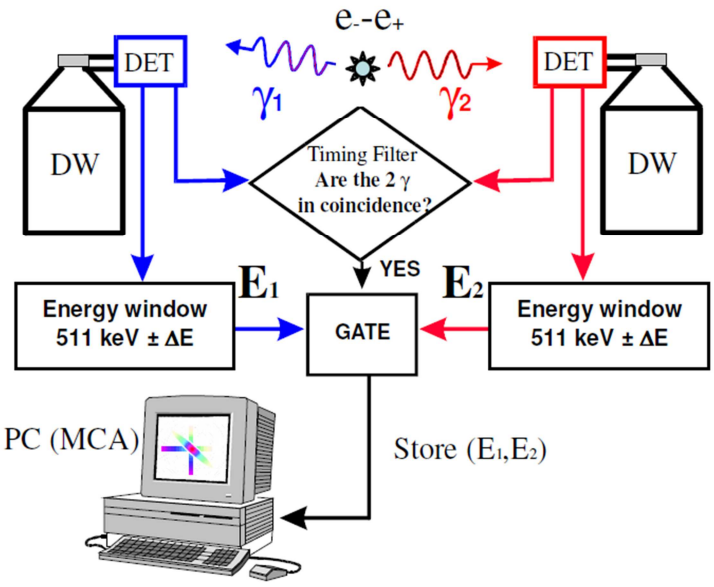

Figure 61 Schematic representation of the CDB setup [149].

When positrons are implanted in the material, they first reach the thermal equilibrium with the system (few picoseconds process). Once thermalized, they can diffuse in the crystal before the annihilation process takes place (~ 100 ps process); in a perfect crystal, the positrons can visit up to 10^7 atomic sites. Its diffusion process is ruled by the electrostatic repulsion with respect to the positive metal ions. For this reason, any open volume like a vacancy or a lattice irregularity (e.g. dislocation) could represent an effective trap for the positron during its diffusion process. The presence of vacancy-type defects in the material can thus induce the trapping of the positrons, and this can affect the energy distribution of the annihilation events recorded in CDB: in fact, inside the vacancy the probability associated to annihilation events with core electrons is sensibly reduced. Since valence electrons are characterized by an expectation value of the momentum p_L lower then the core ones, an increased concentration of effective positron traps results in a reduced broadening of the recorded energy distribution [148, 150].

The measured CDB spectra can be characterized by the two parameters *S* and *W*, which are presented and defined in Figure 62. As it is graphically shown, *S* is strongly related to annihilation events with valence electrons; according to the previous discussion, its values should be enhanced in presence of effective positron traps in the

crystal (Figure 62 *(a)* and *(b)*). Nonetheless, it is important to highlight that not all the vacancy-type defects are active as positron traps; in fact, in several systems they can be seen as a charged defects. In particular, in anatase TiO_2 oxygen vacancies are recognized as doubly positively charged defects ($V_O^{\bullet\bullet}$, see Section 2.3.2); this results in a repulsion effect with respect to the diffusing positron, that for this reason should not be trapped in presence of a monovacancy. Nevertheless, the presence of coupled vacancies or vacancy clusters (see Figure 62 *(c)*) could eventually result in the formation of an effective positron trap even for positively charged defects, leading in this case to the increment of the *S* parameter.

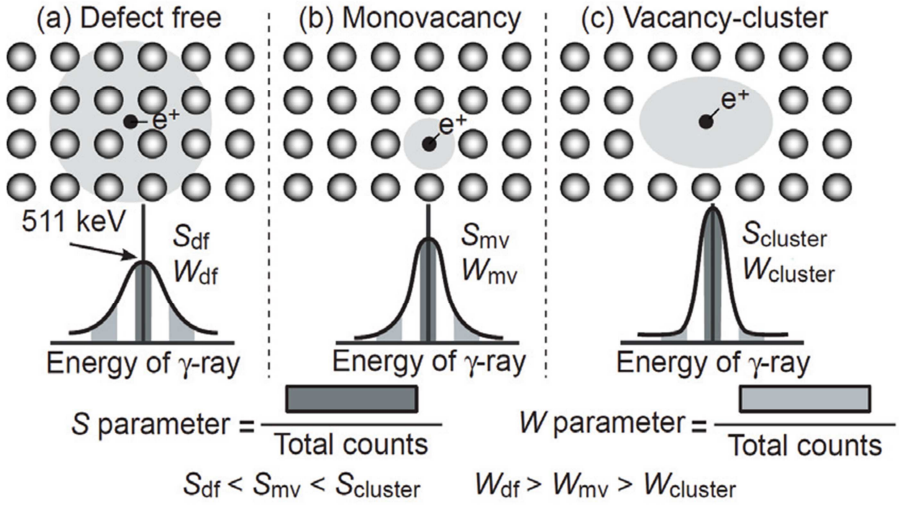

Figure 62 Representation of positrons in *(a)* free state, *(b)* trapped state by a single vacancy, *(c)* trapped state by a vacancy cluster, and their effect on the resultant PAS-CDB energy distributions. The *S* and *W* parameters are graphically and analytically defined. Picture taken from reference [151].

The annihilation events with core electron shells are usually associated with non-trapped positrons (Figure 62 *(a)*), and are characterized by the *W* parameter. The core-electrons region is usually identified for $|p_L| > 1$ atomic units (where a Doppler shift of 1 keV corresponds to a momentum value of $p_L = 0.54$ atomic units – a.u.). These momentum regions of the obtained energy distribution contain information on the chemical elements which were surrounding the annihilation events. As a result, since these events mostly happen for non-trapped positrons, important evidences on the first neighbor atoms with respect to the annihilation site can be collected [150].

Nonetheless, for studies aiming at a fine chemical analysis, reference samples for the constituting elements of the studied compound can be fundamental in the

determination of the core electron contributions even at low energy momentum; in this case it is necessary to report the data in terms of the relative difference with respect to the energy distribution collected for one of the sample references [148].

5.3.2 PAS-CDB on TiO_2-based films

Using a monoenergetic positron beam (obtained starting from a ^{22}Na atoms source), the energetic distribution of the annihilation events collected in coincidence by the two detectors can be collected for several implantation energies. Several Doppler broadening spectra have been acquired in the energetic window 0.1 – 17 keV for optimally doped TaTO (nominal Ta = 5 at.%) and TiO_2 samples on glass substrates and synthesized in several conditions. In this thesis work only results related to TaTO samples are presented, since the TiO_2 data are still under analysis. In particular the difference between a vacuum and an air annealed TaTO sample deposited at an optimal p_{O2} of 1.25 Pa will be here discussed.

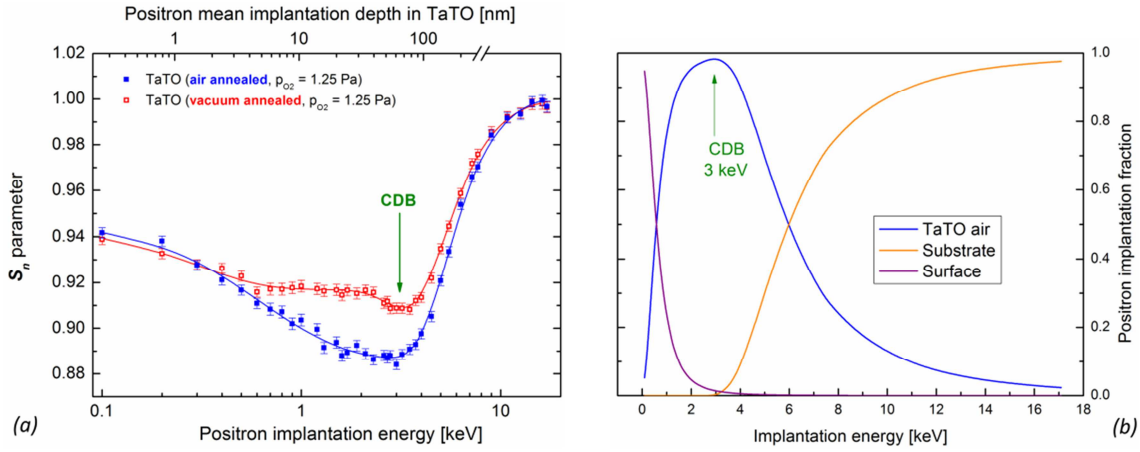

Figure 63 *(a)* *S* parameter normalized with respect to the *S* parameter of the glass substrate ($\boldsymbol{S_n = S/S_{Glass}}$) as a function of the positron implantation energy (bottom *x*-axis) and of the positron implantation depth (top *x*-axis) for air (blue) and vacuum (red) annealed TaTO (p_{O2} = 1.25 Pa) films. *(b)* Fraction of implanted positrons according the VEPFIT model for the air annealed TaTO film. The green arrows are representing the positron implantation energy chosen for this study.

In Figure 63 *(a)* the normalized $S_n = S/S_{Glass}$ parameters evaluated for vacuum and air annealed TaTO samples (p_{O2} = 1.25 Pa, red and blue dots respectively) are reported as a function of different positron implantation energies (which are corresponding to different positron implantation depths). The experimental data were treated with the VEPFIT model [152]. As it is possible to see from Figure 63 *(b)*, the

interpolation of this model allows to identify the fraction of the implanted positrons *(i)* at the thin film surface (purple line) and *(ii)* at the film/substrate interface (orange line); *(i)* and *(ii)* are both obviously characterized by a high amount of defects, resulting in the high S_n evidenced at the lowest and at the highest positron implantation energies for the analyzed TaTO samples (see Figure 63 *(a)*). Nonetheless, the third contribution *(iii)* can be assigned to the implanted positrons in the "bulk" of the thin film (black line). The contribution *(iii)* is consequently the most interesting for the study of the material, and the most indicated implantation energy for the CDB analysis is the one which is ensuring that the highest part of the annihilation events is happening inside the film, avoiding the presence of interface defects. For our experiments, a positron implantation energy of 3 keV is ensuring that more than 98% of the positrons are localized in the anatase crystal (chosen energy highlighted by green lines in Figure 63 *(a)* and *(b)*).

Moreover, the interpolation of this model allows to estimate the diffusion length of the positrons in the lattice, which in our case was found to be around 5 – 10 nm for both doped and undoped TiO_2. This is an important indication that the majority of the positron annihilation events should not result affected by the presence of grain boundaries (which were found to be around tens of micrometers in our samples, see Section 4.2.1). Under these conditions it is possible to safely state that the collected CDB distribution energies are representative of the material itself.

S_n parameter: we focus now on the annihilation events at a fixed positron implantation energy of 3 keV. For the TaTO samples deposited at an optimal p_{O2} of 1.25 Pa, the crystallization process performed in reducing atmosphere is associated to the presence of a higher amount of positron traps with respect to the oxygen-rich thermal treatment ($S_{n\text{-}vacuum} > S_{n\text{-}air}$, Figure 63 *(a)* in coincidence of the green arrow). In this framework it is useful to highlight that the higher amount of defects in the vacuum annealed TaTO cannot be in principle explained with the only presence of a higher amount of oxygen vacancies $V_O^{\bullet\bullet}$ with respect to the twin sample crystallized in air (see Section 5.3.1).

Core electrons contribution: as reference samples we employed a single crystal of anatase TiO_2 (Alfa Aesar - purity 99.8%, for which we will refer from now on as "pure TiO_2"), and metallic Ti and Ta foils (99.98 % purity) which were investigated with PAS-CDB in the same experimental setup.

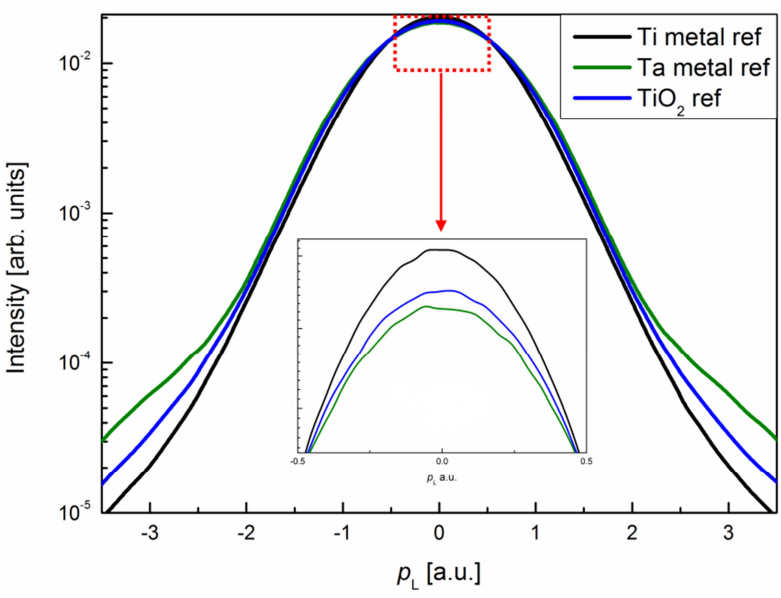

Figure 64 PAS-CDB energy distributions normalized to the same area for the employed reference samples. As indicated by the red highlighted region, the inset graph is representing a magnification at low momentum p_L.

In Figure 64 the corresponding energy distributions are reported. In particular it is useful for the discussion of the following results to highlight that:

- at high momentum ($|p_L| > 2\ a.u.$) the contribution of Ta electrons in the annihilation events is predominant with respect to the other references;
- at low energy momentum ($|p_L| < 0.5\ a.u.$) the contribution of Ti electrons in the annihilation events is predominant with respect to the other references.

In order to enhance the core electron contributions, the CDB distributions obtained for vacuum and air annealed TaTO samples are evaluated and reported in Figure 65 in terms of the relative difference with respect to the pure TiO_2 reference according to

$$\delta = \frac{\rho - \rho_{TiO_2}}{\rho_{TiO_2}} = \frac{\rho}{\rho_{TiO_2}} - 1$$

Comparing the data of the TaTO films (vacuum and air annealed reported in red and blue respectively in Figure 65) it is possible to highlight the following points:

a) at low momentum ($|p_L| > 0.5\ a.u.$) a larger Ti electrons contribution (see Figure 64) is evidenced in the relative distribution of the vacuum annealed film δ_{vacuum}, with respect to the air annealed δ_{air} one. This could be reasonably interpreted as a non-negligible reduction of Ti atoms in the lattice of the air annealed TaTO with respect to the vacuum annealed one, i.e. higher

concentration of titanium vacancies V_{Ti}'''' induced by the oxygen rich crystallization environment;

b) the momentum regions where the relative difference with respect to the pure TiO_2 reference δ is shown to increase ($|p_L| \sim 2\ a.u.$) can be attributed from literature to the annihilation events with oxygen 2p electrons [153-155]. It is noticeable that this contribution is significantly higher in the case of the air annealed TaTO sample. This can be rationally induced by the presence of a higher concentration of oxygen vacancies $V_O^{\bullet\bullet}$ in the vacuum annealed film with respect to the air annealed one.

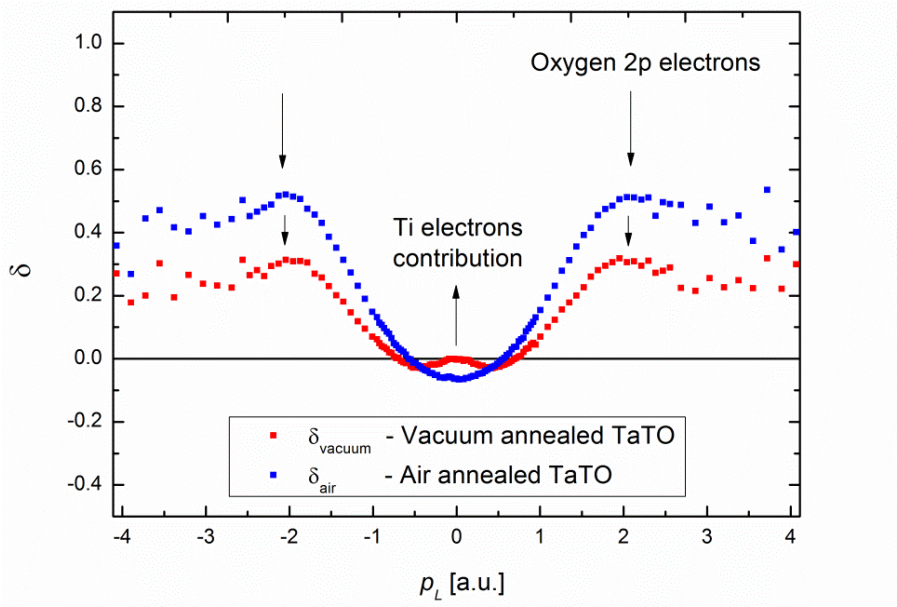

Figure 65 Relative differences of the momentum distribution for TaTO (p_{O2} = 1.25 Pa) films crystallized in vacuum (red $\boldsymbol{\delta_{vacuum}}$) and air (blue $\boldsymbol{\delta_{air}}$). The arrows are highlighting the detectable contributions.

Discussion: to sum up, the data referred to the core electron contributions are pointing to the presence of a higher concentration of intrinsic electron donors ($V_O^{\bullet\bullet}$) when TaTO is crystallized in reducing atmosphere, while the crystallization in oxygen-rich conditions should result in the formation of a higher concentration of electron killer defects (V_{Ti}''''). Nonetheless, the analysis of the S_n parameter is showing the presence of a significantly higher amount of effective positron traps in the vacuum annealed TaTO film with respect to the air annealed one. In first instance, this could be read as a controversial evidence with respect to the data acquired for the annihilation events with core electrons, since just V_{Ti}'''' should effectively act as an efficient positron trap site (see

Section 5.3.1). Nonetheless, it has been experimentally and theoretically found that in presence of oxygen vacancy clusters, or when complexes between the vacancy and different point defects are formed in the crystal, the positron trapping mechanism can be activated [150, 151, 156, 157].

It is here hypothesized that the highly conducting state of the vacuum annealed TaTO could be associated to an intimate coupling in the anatase crystal between the substitutional tantalum and the oxygen vacancies. The crystallization process performed in oxygen-containing atmospheres would consequently result in a partial/total disruption of this interplay, due to the resultant reduced amount of oxygen vacancies in the lattice. In this framework, it is important to mention that in 2009 Kamisaka *et al.* [134] proposed based on first principle calculations that the adjacency between oxygen vacancies and the substitutional extrinsic donor could be the key aspect for the high electron efficiency release in donor doped TiO_2 materials (see Section 2.3.3).

Nonetheless, in the air annealing process the formation of *p*-type defects like V_{Ti}'''' is favored (see Section 2.3.2), giving a probable contribution to the drastic reduction of the overall electron population in the conduction band.

Finally, based on a preliminary analysis of the linear combinations of the relative difference in the energy distributions of the metallic Ti and Ta references with respect to the pure TiO_2 reference ($\delta_{Ti-reference}$ and $\delta_{Ta-reference}$), it has been found that the difference between the TaTO films crystallized in vacuum and air atmospheres can be well described by the presence of oxygen vacancies decorating the Ta_{Ti} sites in the anatase lattice. Further analysis will focus on the validation of this hypothesis which is still under discussion, based also on the data acquired for undoped TiO_2 samples and TaTO deposited at different oxygen partial pressures.

6. Electrical properties control of TiO_2-based films via ultra-fast crystallization processes

Up to now it has been widely discussed that a thermal treatment performed in reducing atmosphere is a basic requirement in order to obtain transparent conducting TiO_2-based polycrystalline films (see Section 4.2.1). In this chapter experimental evidences proving the possibility to uncouple the TiO_2 functional properties with respect to the annealing environment via ultra-fast crystallization processes are shown.

In particular, in Section 6.2 is discussed how the accurate examination and control of the parameters involved in the annealing process allows to obtain for both TaTO and TiO_2 thin films the same transparency and low resistivity resulting from a standard vacuum annealing cycle (overall process time required ~ 180 minutes) in a thermal treatment which lasts just 5 minutes and is performed in a cheap nitrogen atmosphere at ambient pressure (20 ppm oxygen concentration). It is worth mentioning that a previous study on Nb-doped TiO_2 thin films reported on the possibility of obtaining good resistivity values ($\rho \sim 8 \times 10^{-4}$ Ωcm) upon annealing in a diluted atmosphere (0.5 atm) of highly pure nitrogen (purity 99.9998%, nominal oxygen concentration < 0.5 ppm) at 350 °C for 20 minutes [158]. The physicochemical mechanisms behind this result (e.g. possible role of oxygen incorporation during annealing) were however not discussed.

Here instead, a systematic investigation and discussion of electrical data collected *in situ* during ultra-fast annealing treatments performed in different nitrogen-oxygen mixtures also allowed to identify the key role played by the oxygen partial pressure and, in particular, in which way this could negatively affect the electrical properties of TiO_2-based thin films (Section 6.3.1).

Aimed experiments (e.g. secondary ion mass spectroscopy in depth profiles on TaTO films crystallized in ultra-fast treatments in presence of traceable ^{18}O) disclose the possibility to relate oxygen incorporation from the annealing environment to a decreased amount of conduction electrons in a tens of nanometers thick surface layer (Section 6.3.2).

The experimental data collected for the ultra-fast annealing cycles presented in this chapter are based on the realization of a dedicated furnace, whose design and building has been personally carried out by the author in collaboration with U. Klock at the Max Planck Institute for Solid State Research of Stuttgart. In Section 6.1 this experimental setup is briefly presented.

The most part of the results presented in this chapter are collected in a paper which has been recently accepted for publication in a peer review journal [159].

6.1 Ultra-fast annealing furnace and experiment design

The ultra-fast annealing processes have been carried out in a home-made furnace (Figure 66), designed so to permit precise and repeatable heating temperature ramps of 300 °C/min with the employment of 5 IR lamps* (RS components Ltd. UK, Heat lamp 500 W R7s 230 V) concentrically placed outside a tubular quarz chamber.

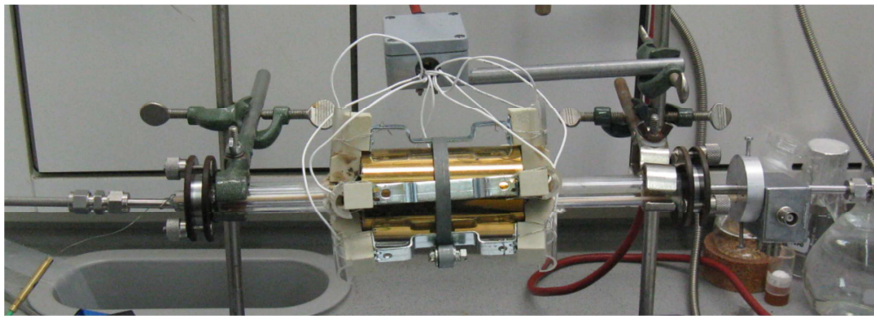

Figure 66 Picture of the home-made annealing furnace concived and employed for this study.

* Chosen so to avoid UV emission

The furnace allows also for fast cooling ramps (about 150 °C/min) by means of an external flux of cold N_2 gas. The temperature is measured using a *K*-type thermocouple (diameter 0.5 mm) placed on the sample holder at 0.5 mm from the substrate.

The design of the sample holder together with the anchoring mechanism of the film allows to *in-situ* record its electrical resistance via 2-point DC measurements (source / measure unit Keithley 2604B). The maximum applied current was 1 mA and the maximum compliance voltage 5 V. In order to reliably compare the acquired resistance measurements among different samples, the effect of different contact geometries has been minimized evaporating on top of the films Ti/Au (200/2000 Å) electrodes with 1 mm distance from each other (see Figure 67).

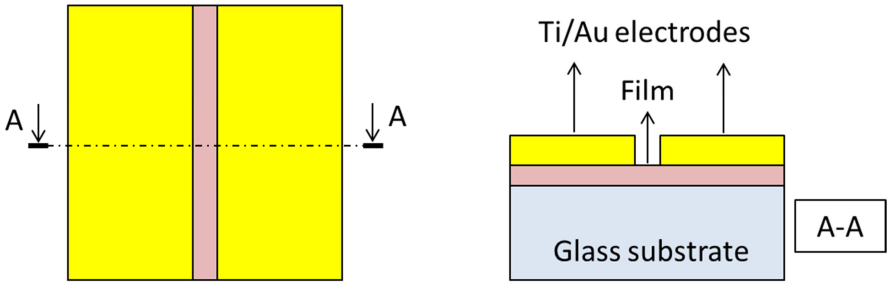

Figure 67 Schematic representation of a sample with metal-contacts deposited on top for the in-situ electrical measurements.

The experiments are carried out in a background gas at atmospheric pressure. The employment of a continuous flux (50 sccm for all the shown experiments) allows to precisely monitor the oxygen concentration of the chosen gas mixture with a Cambridge Sensotec RapidOX 2100ZF lambda sensor placed at the outlet (sensitivity from 10^{-20} ppm to 100% O_2).

6.2 Comparison between standard and ultra-fast thermal cycles for TiO_2-based thin films

Amorphous optimally doped TaTO (Ta = 5 at.%) and undoped TiO_2 150 nm thick films were obtained via room temperature PLD on soda-lime glass (10 × 10 × 1 mm^3) and Si (100) substrates in an oxygen background pressure of about 1 Pa (TaTO was deposited at p_{O2} = 1 Pa, while TiO_2 at 1.25 – 1.3 Pa).

6.2.1 Standard annealing processes

In line with what has been discussed in Section 4.2.1, a standard post deposition annealing process (i.e. T = 550 °C for 1 hour with heating and cooling ramps of 10 °C/min obtained with a resistive plate oven) performed in vacuum resulted in transparent and conducting polycrystalline anatase films:

	ρ [Ωcm]	n [cm^{-3}]	μ [$cm^2V^{-1}s^{-1}$]	T_{vis} [%]
TiO_2	6.93×10^{-3}	5.70×10^{19}	15.8	79.3
TaTO	6.77×10^{-4}	7.99×10^{20}	11.5	81.4

The TiO_2-based thin films were also annealed using the same standard process performed in 1 atm of pure nitrogen gas (grade 99.999%, nominal O_2 concentration < 3 ppm). As expected from previously reported data (see Section 4.2.1), the samples crystallized in N_2 were insulating since their resistance was too large to be measured with our experimental setup (maximum applicable curret of 0.1 μA, voltage compliance 10 V) and thus no value of the resistivity could be determined.

6.2.2 Ultra-fast annealing (UFA) process in nitrogen atmosphere

An abrupt drop in the electrical resistivity recorded for amorphous TiO_2-based films during the heat treatment was already proposed in some published works to be indicative of its crystallization [70, 160]. Based on these experimental observations, and taking advantage of the ability to *in-situ* measure the electrical properties in our home-made furnace, it was possible to identify an ultra-fast annealing cycle (UFA) which allows to obtain the completion of the above mentioned crystallization resistance drop in the lowest process time achievable with our experimental setup.

The UFA process consists of a heating temperature ramp of 300 °C/min up to the peak temperature of 460 °C. The cycle is not employing any dwell time at this temperature, and the chamber is immediately cooled down with the fastest rate achievable with our setup (~ 150 °C/min). The overall time needed to fully accomplish the thermal treatment is about 5 minutes. Several UFA cycles were performed at ambient pressure under different oxygen/nitrogen mixtures (measured oxygen concentrations: 20 ppm, 1000 ppm and 21%). The 20 ppm gas was obtained by directly

employing nitrogen from the lab distribution line, while the 1000 ppm and 21% concentrations were obtained by properly mixing N_2 and O_2 from a 5.0 purity oxygen bottle.

In this section we just focus on the results obtained for TiO_2 and TaTO thin films for an UFA treatment performed in nitrogen atmosphere (20 ppm O_2).

In Figure 68 the *in-situ* measured electrical resistance (dots linked to left y-axis) and temperature (dashed lines linked to right y-axis) for doped (red) and undoped (black) TiO_2 samples are plotted as a function of time. The presence of Ta does not significantly affect the electrical resistance when the TiO_2-based samples are still in the amorphous state, meaning a non-activation of the dopant (in agreement to what has been discussed in Section 4.2.1).

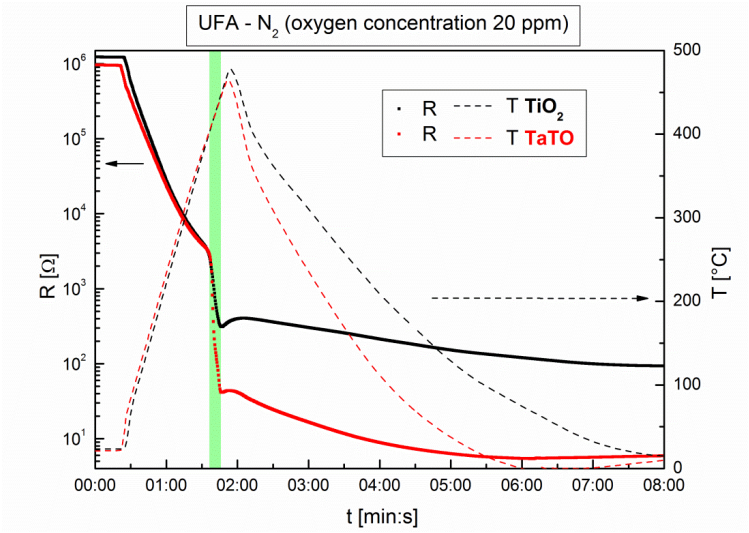

Figure 68 *In-situ* resistance measurements (dots, left y-axes) and corresponding temperature profiles (dashed lines, right y-axes) for TiO_2 (black) and TaTO (red) thin films crystallized in N_2 atmosphere with 20 ppm oxygen concentration. The green colored region is highlighting the time interval in which the abrupt resistance drop takes place. Picture taken from [159] and modified.

An abrupt and sharp decrease of the resistance upon reaching a temperature of about 400 °C is recorded, irrespective of the presence of the doping element. As already mentioned, this transition is likely to be connected to the crystallization of the amorphous film, the occurrence of which is highlighted in Figure 68 by the green area. A further indication in support of this hypothesis is related to the switch of the alectrical conduction behavior for both the film compositions: while for T < 400 °C they are both characterized by a semiconducting behavior ($dR/dT < 0$), after the abrupt resistance drop they both become metallic ($dR/dT > 0$). It is worth to highlight that the time and

temperature values (t_{start}, t_{end} and T_{start}, T_{end}) defining the zone where the resistance drop is taking place (green region in Figure 68) are independent with respect to the presence of the dopant: the T_{start} and T_{end} of this process are at around 400 °C and 450 °C respectively (t_{start} - t_{end} = 10 s) for both samples. This proves that the large amount of Ta (5 at.%) is probably not affecting the crystallization kinetic of TiO_2.

The obtained final value of resistance at room temperature ($R_{T=25°C}$) for TaTO is one order of magnitude lower than for TiO_2 (6 Ω and 96 Ω, respectively). It is important to note that the resistance difference between the doped and undoped film is of the same order of magnitude of the one obtained upon standard annealing treatment in vacuum (see Section 6.2.1). Interestingly, it was also found for TaTO that an UFA process performed in reducing atmosphere (Ar/H_2 mixture, H_2 at 2% - measured oxygen concentration < 10^{-20} ppm) resulted in the same $R_{T=25°C}$ as the one performed in nitrogen (not shown).

Based on these observations we performed the UFA treatment in N_2 atmosphere on twin TiO_2-based amorphous samples without electrodes evaporated on top, with the aim of properly comparing *ex-situ* the obtained optical and electrical properties (i.e. ρ, n and μ via 4-point measurements) with respect to the samples crystallized with a standard vacuum annealing process. An UFA cycle on a TaTO film without electrodes in a hydrogen-containing atmosphere was also performed.

In the table below we report the final room temperature electrical properties obtained for TaTO and TiO_2 after UFA. For a better comparison among the obtained results, we also report the data of the standard annealed samples (already shown in Section 6.2.1).

	Annealing treatment	$\boldsymbol{\rho}$ [Ωcm]	$\boldsymbol{n}$ [cm^{-3}]	$\boldsymbol{\mu}$ [$cm^2V^{-1}s^{-1}$]
TaTO	**Standard-Vacuum**	6.77×10^{-4}	7.99×10^{20}	11.5
	Standard – N_2	not measurable	not measurable	not measurable
	UFA – Ar/H_2	7.65×10^{-4}	7.46×10^{20}	11.0
	UFA – N_2 20 ppm	6.85×10^{-4}	8.30×10^{20}	11.0
TiO_2	**Standard Vacuum**	6.93×10^{-3}	5.70×10^{19}	15.8
	Standard – N_2	not measurable	not measurable	not measurable
	UFA – N_2 20 ppm	9.04×10^{-3}	4.77×10^{19}	14.5

Notably, the TaTO sample UFA treated in reducing atmosphere (Ar/H_2, oxygen concentration < 10^{-20} ppm) and the one in N_2 atmosphere (20 ppm O_2) both show almost identical electrical properties with respect to those obtained with a standard vacuum annealing treatment. In the case of undoped TiO_2, UFA performed in N_2 - 20 ppm resulted in a slight higher resistivity, although the overall electrical properties are highly comparable. It is worth to note that the electron mobility values obtained for the 5-minutes-lasting UFA cycle are very similar to the ones obtained with a 180-minutes-lasting standard vacuum treatment.

Surprisingly, although a standard treatment performed in a purer N_2 atmosphere (O_2 < 3ppm) is leading to highly insulating films, no degradation of the charge carrier density is observed for the UFA treatment performed in N_2 with 20 ppm O_2 concentration.

"Extended" UFA-like treatments were performed in order to investigate the effect on the resistance of a longer exposure (10 min) to the 20 ppm O_2 – nitrogen atmosphere at the peak temperature (460 °C).

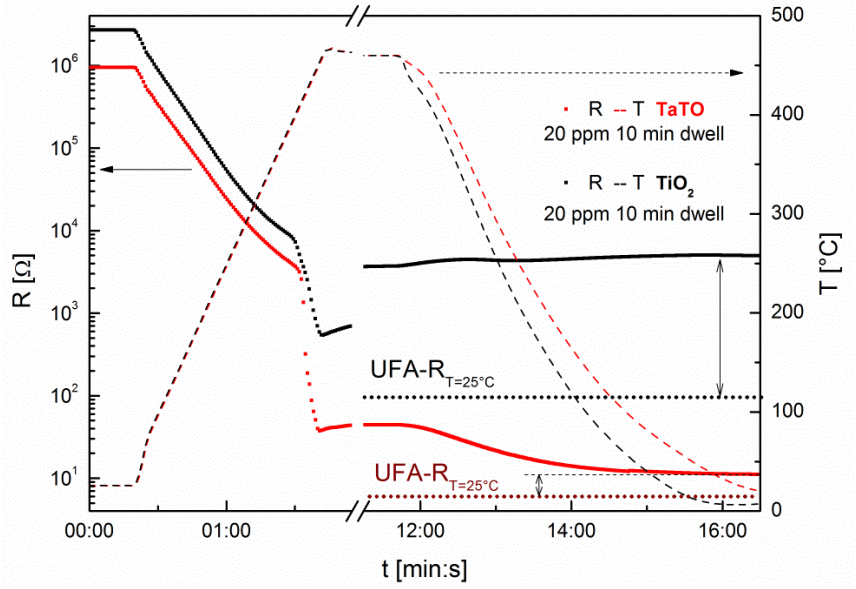

Figure 69 In-situ resistance measurements (dots, left y-axes) and corresponding temperature cycles (dashed lines, right y-axes) for TaTO (red) and TiO_2 (black) thin films crystallized in N_2 (20 ppm O_2 concentration) with extended (10 minutes dwell at the peak T = 460°C) UFA-like cycles. The dotted horizontal lines reported after the axes brake (adopted in the dwell time laps for a clearer data presentation) are representing the resistance value obtained at room temperature ($R_{T=25°C}$) for TaTO (red) and TiO_2 (black) thin films crystallized in UFA cycles performed in the same N_2 atmosphere without employing dwell time (complete acquired curves reported in Figure 68). Picture taken from [159] and modified.

The results of this experiment are reported in Figure 69, and clearly demonstrate the detrimental effect on the electrical conductivity of a longer exposure to this N_2-based atmosphere: the obtained resistance is increased of a factor 2 for TaTO ($R_{T=25°C}$ = 11 Ω) and of a factor 50 for TiO_2 ($R_{T=25°C}$ = 4965 Ω) with respect to the one resulting from the UFA treatment performed in the very same atmosphere. These results highlights the fundamental importance of the process time employed in the thermal cycles.

Moreover, an XRD[†] and optical investigation of standard and UFA treated samples has been performed, with the aim of highlighting the presence of any possible difference among the thin films crystallized with these two different thermal cycles. The results are shown in Figure 70.

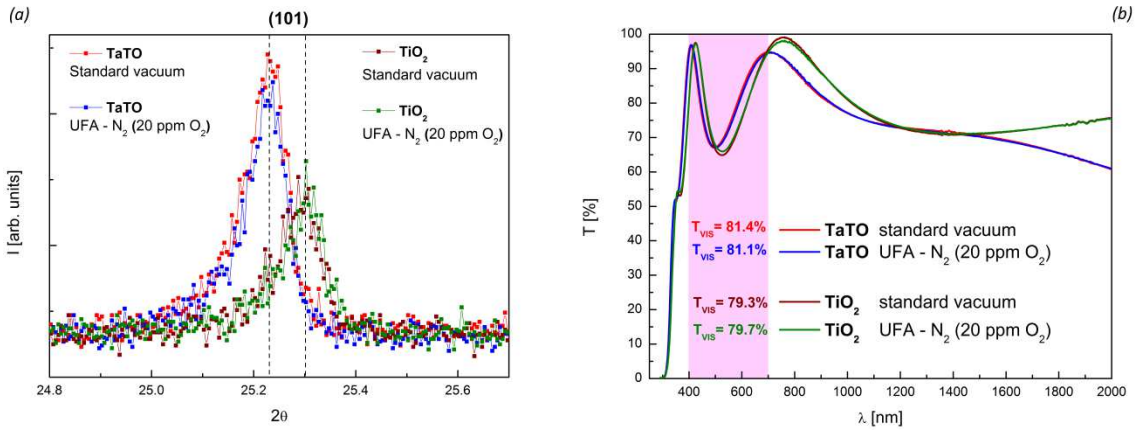

Figure 70 *(a)* XRD acquisition for the (101) anatase peak in grazing incident angle (ω = 5°) of TaTO and TiO_2 films annealed with a standard vacuum (red and purple colored lines for TaTO and TiO_2 respectively) and an UFA treatment in N_2 with 20 ppm of oxygen (blue and green colored lines for TaTO and TiO_2 respectively). *(b)* the total transmittance spectra for the same samples are reported (colors in agreement with *(a)*); the pink shaded part of the graph shows the visible region of the spectrum (λ = 400 – 700 nm) and the mean transmittance obtained for the samples (T_{vis}) is reported within it. Pictures reproduced from [159].

In Figure 70 *(a)* we report a comparison between the most intense (101) XRD anatase peaks for TiO_2 and TaTO samples treated with the two different thermal cycles: no significant difference is detectable regarding the crystallinity quality of the films when annealed with the standard vacuum annealing or the N_2-UFA treatment. The intensity variation between doped and undoped samples is in line with previously

[†] XRD measurements performed by D. Chrastina (L-NESS, Dipartimento di Fisica, Politecnico di Milano, Italy).

discussed results (see Section 4.2.1), as well as the absence of other TiO_2 polymorphs (e.g. rutile) or any other segregated phase (e.g. metallic Ta or Ta_2O_5) from the analysis of the complete θ-2θ scans (not shown). In this framework, it is worth to underline that the presence of N_2 in the annealing atmosphere (in both UFA and standard cycles) does not significantly hinder the crystallization process, since the anatase phase was formed in all cases.

Moreover, consistently with the collected data from both XRD and electrical measurements, also the optical properties of TaTO and TiO_2 are shown to be independent with respect to the employed thermal cycle (see Figure 70 *(b)*). In fact, the superimposed transmittance curves for doped and undoped samples clearly support the equivalence of the two thermal cycles; in particular, the T_{vis} of TiO_2 and TaTO films (all reported inside the pink shaded region of Figure 70 *(b)*) respectively reaches and exceeds 80%.

Finally, it is noteworthy how fast the crystallization process in UFA-treated TiO_2-based thin films is taking place. We attribute this capability to the characteristic "explosive crystallization" of TiO_2 (discussed also in Section 4.2.1), related to the latent heat released during the formation of the crystalline structure, which is large enough to result in a runaway process that continues until the amorphous material is completely consumed [127, 161]. As a matter of fact, we have already shown (by optical microscopy) the presence of macrometric-sized grains in our TiO_2-based samples annealed with the standard cycle (see Section 4.2.1 and 4.2.2). Consistently, also in this study the lateral size distribution of the anatase grains for both TiO_2 and TaTO films was found to be on the order of tens of micrometers even in the case of the N_2-based UFA treatments. Nonetheless, as it is possible to note from Figure 71, for the standard treatment a larger average size of crystallites is detected.

Quite remarkably, it is thus possible to conclude that despite the significantly lower temperature (460 °C Vs 550 °C) and shorter duration (5 min Vs 180 min), the UFA treatment performed in low purity N_2 at atmospheric pressure can be considered a valid (and industrially scalable) alternative to the standard vacuum annealing treatment for the obtainment of TiO_2-based TCOs.

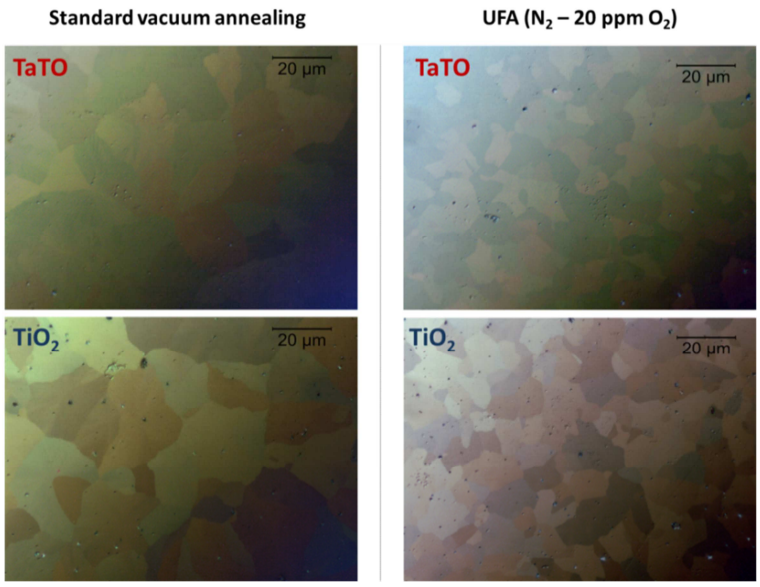

Figure 71 Surface images captured using polarized light through optical microscope of TaTO (1st row) and TiO_2 (2nd row) thin films crystallized with a standard vacuum (left side) and UFA performed in N_2-based atmosphere (right side). Picture reproduced from [159].

6.3 Role of oxygen in the UFA crystallization environment

Apart from the high potential from an applicative point of view, the results collected and discussed in the previous section represent a definitive indication that the UFA cycle, due to its lower temperatures involved with respect to the standard treatment and the very fast process time, allows to inhibit the interaction of the material with the crystallization atmosphere. In other words, the ultra-fast treatment from one side permits to obtain a full crystallization of the TiO_2-based films, while on the other prevents the material to move in the direction of the thermodynamic equilibrium, which in the case of N_2-based atmosphere would lead to the formation of insulating films (see Section 6.2.2 and 6.2.1).

The thorough investigation conducted so far in this thesis work on the material properties control, strongly suggests that the oxygen incorporation should be strictly involved in the loss of conductivity of TiO_2-based materials. Consequently, even if in the case of the N_2-based atmospheres we are dealing with impurities in the order of some parts per million (O_2 < 3ppm and equal to 20 ppm in the case of the standard treatment and the UFA respectively), it is likely that the oxygen exchange (or the ability to inhibit this process) is dictating the resulting electrical properties.

6.3.1 *Effect of different oxygen concentrations in the UFA atmosphere*

In general, the oxygen exchange mechanism with the surrounding atmosphere depends on *(i)* oxygen partial pressure, *(ii)* temperature, and *(iii)* process duration. As a matter of fact, for the N_2-based atmosphere the points *(ii)* and *(iii)* were already demonstrated to affect the electrical properties of TiO_2-based films by comparing UFA with the standard annealing treatment and with the "extended" UFA-like cycle respectively. We now focus on the point *(i)*, maintaining the same UFA temperature cycle, but *in-situ* monitoring the effect of an increasing oxygen content on the electrical properties of TaTO and TiO_2 films.

The acquired data for UFA crystallizations performed in a N_2-based atmosphere containing 20 ppm (red), 1000 ppm (orange) and 21% (blue) oxygen concentration are plotted in Figure 72 and Figure 73 for TaTO and TiO_2 samples respectively.

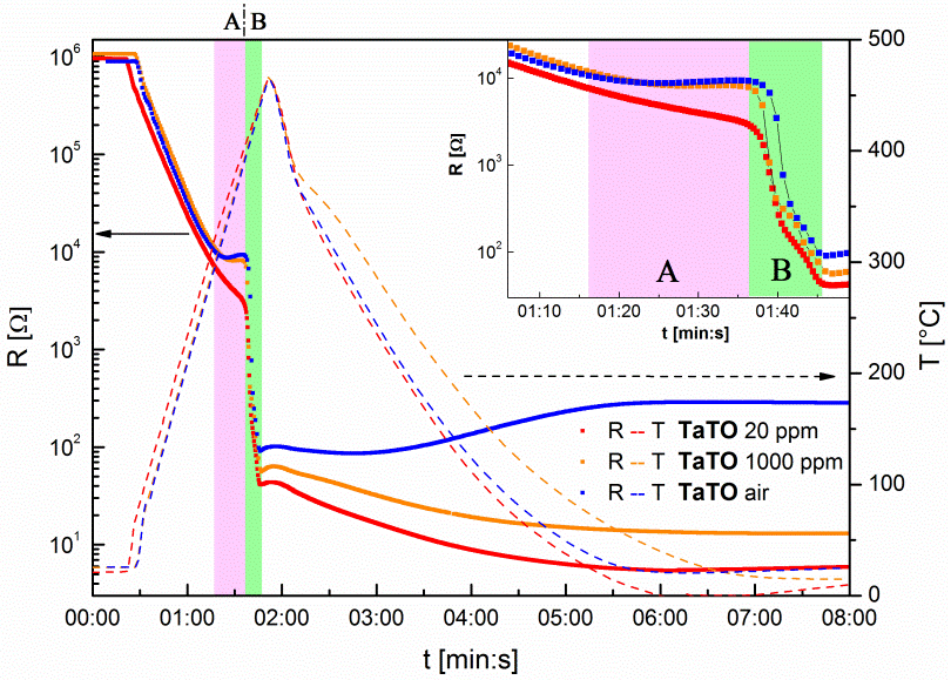

Figure 72 In-situ resistance measurements (dots, left y-axes) and corresponding temperature profiles (dashed lines, right y-axes) for TaTO thin films crystallized in N_2-based atmospheres with different oxygen concentrations: 20 ppm (red, already presented in Figure 68), 1000 ppm (orange) and 21% (synthetic air, blue) atmospheres. The regions A and B (pink and green colored respectively) represent the time intervals in which the resistance of the thin films starts to be affected by the presence of different p_{O2} (A) and the time intervals in which the abrupt resistance drop takes place (B). In the inset is reported a magnification of the resistance behavior in the regions A and B. Picture reproduced from [159].

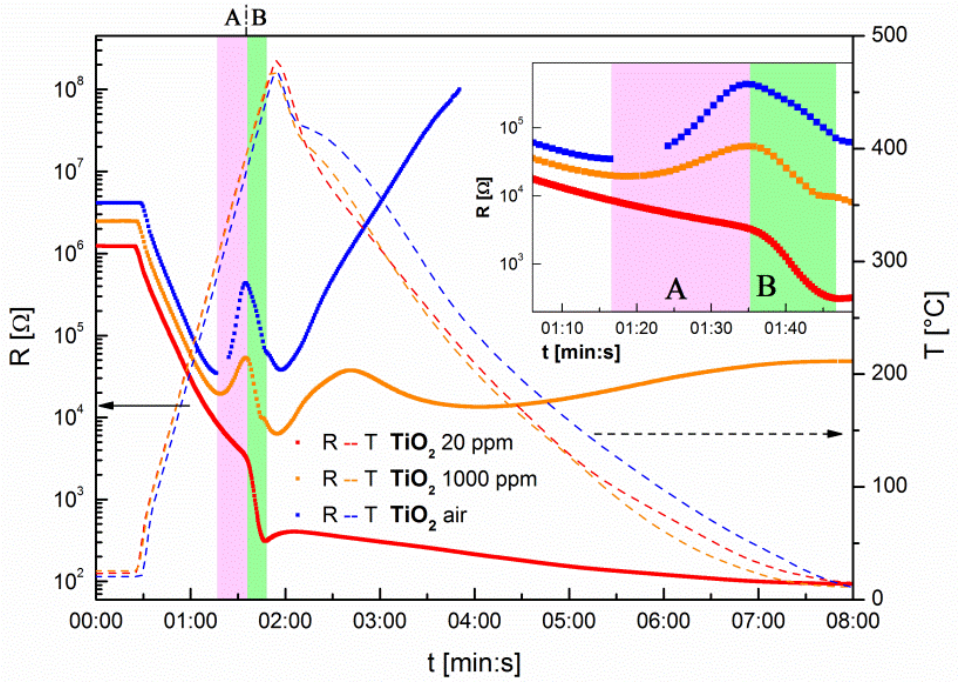

Figure 73 In-situ resistance measurements (dots, left y-axes) and corresponding temperature profiles (dashed lines, right y-axes) for TiO_2 thin films crystallized in N_2-based atmospheres with different oxygen concentrations: 20 ppm (red, already reported in Figure 68), 1000 ppm (orange) and 21% (synthetic air, blue) atmospheres. The regions A and B (pink and green colored respectively) represent the time intervals in which the resistance of the thin films starts to be affected by the presence of different p_{O2} (A) and the time intervals, in which the abrupt resistance drop takes place (B). In the inset is reported a magnification of the of the resistance behavior in the regions A and B. There are no resistance points for an electrical resistance higher than 1×10^8 Ω (blue dots) since this is the upper limit measurable with our experimental setup. Picture reproduced from [159].

Irrespectively of the presence of the dopant or of different oxygen concentrations in the annealing atmospheres, all the performed UFA treatments show the already discussed (see Section 6.2.2) abrupt and sharp decrease of the resistance once a temperature of ~ 400 °C is reached. The delimiting time region of this process is highlighted by a green area, called region-B in Figure 72 and Figure 73. As discussed in the case of TiO_2 and TaTO UFA crystallized in 20 ppm O_2 (red curves in Figure 72 and Figure 73, previously shown in direct comparison in Figure 68), we notice that even at higher p_{O2} the time duration of this process is always the same for all the samples (t_{start} - t_{end} ~ 10 s), and consequently also the characteristic temperature window (T_{start} = 400 °C and T_{end} = 450 °C). Interestingly, the order of magnitude of the resistance drop is found to be just dependent on the presence of the dopant in the film, since for all the tested

UFA background atmospheres is estimated to be on the order of a factor 10 for TiO_2, and 100 for TaTO[‡].

While moving from 20 ppm to higher oxygen concentrations, the resistance behavior during the heating cycle is considerably changed, as well as the resultant $R_{T=25°C}$. In the case of TaTO, UFA performed in presence of N_2 with 1000 ppm O_2 (orange curves in Figure 72) results in a more than doubled room temperature resistance with respect to the 20 ppm sample (13 Ω with respect to 6 Ω respectively). Nonetheless the film maintained a metallic behavior during the cooling process (see Figure 72 for *t* > 2 min). In contrast, the crystallization of the TiO_2 sample in the same 1000 ppm atmosphere (orange curves in Figure 73) resulted in a semiconducting behavior in the cooling region, with a $R_{T=25°C}$ orders of magnitude higher than the corresponding cycle performed in 20 ppm (4.2×10^4 Ω Vs 96 Ω). The effect of a further increase of the oxygen concentration is shown for the UFA cycle performed in artificial air atmosphere (N_2 with 21% O_2, blue curves in Figure 72 and Figure 73). In this case a significant and more detrimental effect for the electrical properties with respect to UFA in 1000 ppm is recorded for both doped and undoped samples: they both resulted in a semiconducting behavior, and the resistance at room temperature is increased up to 278 Ω for TaTO, while for TiO_2 was too high to be measurable with our experimental setup ($R_{T=25°C} > 10^8$ Ω).

Nonetheless, an intriguing evidence is connected to the region-A, highlighted in pink in Figure 72 and Figure 73, and representing the resistance behavior recorded just before the abrupt resistance drop highlighted in region-B: in particular, we found that the increasing loss of conductivity with increasing oxygen concentration is always associated by a different resistance behavior recorded in this region-A. Starting from the beginning of the heating cycle, when the temperature is increased in N_2 - 20 ppm O_2 (red curves in Figure 72 and Figure 73) the resistance behavior of both TaTO and TiO_2 could be defined as an almost-monotonic decrease until the region-B begins. On the other hand, for UFA performed in presence of higher oxygen concentrations (1000 ppm and 21%, orange and blue curves respectively in Figure 72 and Figure 73), a resistance increase is recorded in the region-A. Interestingly, this effect is more evident and severe in presence of a higher oxygen concentration. Although this evidenced trend is valid for

[‡] Note that here the temperature dependence of the electrical resistance (dR/dT) is not taken into account ($\Delta T \sim 50\ °C$).

both doped and undoped samples, the recorded resistance bump in region-A is considerably more pronounced for TiO_2 films. Moreover, it is interesting to note that, as it has been observed for the region-B, the time interval (and consequently the ΔT) associated to this phenomenon is again independent with respect to the presence of the dopant (t_{start} - t_{end} ~ 20 s; T_{start} ~ 300 °C, T_{end} ~ 400 °C).

As in the case of UFA crystallized samples at 20 ppm (see Section 6.2.2), we also performed the ultra-fast crystallization of TiO_2 and TaTO films without electrodes in presence of 1000 ppm and 21% O_2 in order to evaluate *ex-situ* their resistivity via 4-point probe technique. For the TaTO samples a notable increase of the resistivity was recorded with respect to the 20 ppm N_2 atmosphere: ρ was around 3.39×10^{-3} Ωcm and 2.31×10^{-2} Ωcm for 1000 ppm and 21% respectively. On the other hand, in the case of TiO_2 samples crystallized in the same atmospheres, the resistivity could not be measured even in the case of the 1000 ppm concentration.

Nonetheless, it is noteworthy that all the acquired data for both TaTO and TiO_2 samples without electrodes UFA treated in 1000 ppm and 21% oxygen concentration have to be considered as only indicative due to a diode-like *I-V* characteristic recorded between the electrical probes and the sample, which actually invalidates the 4-point measurement method (courtesy by A. Ballabio, L-NESS, Dipartimento di Fisica, Politecnico di Milano, Italy). On the contrary, the equivalent samples crystallized under the same UFA conditions with the evaporated Ti/Au electrodes on top exhibit an ohmic behavior between the electrode pads.

Discussion: the collected data for UFA treatments at $O_2 \geq 1000$ ppm are consistent with oxygen penetration in the thin film, probably occurring in the very first stages of the crystallization process (region-A in Figure 72 and Figure 73, before the sharp drop of the resistance highlighted by the region-B). In fact, the different variation of *R* with *T* recorded in the region-A starts at a temperature of ~ 300 °C; this is compatible with several studies performed on amorphous undoped and Nb-doped TiO_2 thin films, which already pointed out that the crystallization process can start with a sluggish rate at temperatures around 300 °C, while at higher temperatures it would be faster (i.e. T ≥ 400 °C), resulting in the abrupt drop of the resistance recorded in region-B of Figure 72 and Figure 73 [70, 74, 127, 160-164]. Moreover, it has been previously noticed that the order of magnitude of this sharp resistance decrease seems to be almost independent with respect to the different oxygen concentration in the annealing

environment for both TiO_2 and TaTO, basically demonstrating that this phenomena should be mainly related to the electron mobility increase in the film. To sum up, we propose that the UFA crystallization process could be rationalized as follows:

- in the so-called region-A (between 300 °C and 400 °C) the first anatase crystal seeds are formed and start their growth with a slow kinetics (because of the still rather low temperature) embedded in the amorphous matrix. In this stage of the process the predicted oxygen exchange with the surrounding atmosphere is favored, and it is thought to increase as the oxygen concentration is increased in the annealing chamber;
- for temperature values between 400 °C and 450 °C (region-B), the growth of the anatase seeds is faster and the crystal grains are starting to merge one with each other (resulting in a fast increase of the electron mobility), finally leading (at the end of the resistance drop) to the complete consumption of the amorphous material. While the crystallization is rapidly evolving, the exchange processes with the surrounding atmosphere seem to be blocked (or very limited) regardless of the presence of a different oxygen concentration in the UFA chamber, meaning that the region-A is basically ruling the charge carrier concentration obtainable for the UFA crystallized thin films at rather high oxygen concentrations (> 20 ppm).

We now focus on the very similar charge carrier density obtained for the standard vacuum annealing process and for the UFA performed in both reducing conditions (10^{-20} ppm O_2) and N_2 atmosphere with 20 ppm O_2 (see Section 6.2.2). The experimental findings suggest that the stoichiometry of the TiO_2-based films is basically solely determined by the p_{O2} employed during the room temperature PLD deposition process (i.e. no exchange with the annealing environment). Consequently, the strict requirement of a reducing atmosphere during a standard annealing cycle for the obtainment of highly conducting TiO_2-based films would be just dictated by the necessity to prevent oxygen incorporation during the long exposure to high temperatures, and not for the formation of further oxygen vacancies (or at least not in a sufficient concentration to effectively change the population of mobile electrons). We notice that this hypothesis is consistent with the demonstrated ability of tuning the charge carrier density of standard vacuum annealed TaTO thin films by just slightly changing the p_{O2} during the room temperature PLD process (see Section 4.2.2).

The experimental evidences also highlight that the inferred oxygen incorporation affects more severely the electrical properties of the undoped films. This can be rationalized in terms of defect chemistry (see Section 2.3.2). Given that the proper p_{O2} employed during the deposition process is thought to ensure the "right" film stoichiometry, without any oxygen exchange during the UFA crystallization cycle the presence of 5 at.% of extrinsic dopant in TaTO results in a charge carrier concentration in the order of 10^{21} cm^{-3}, compared to about 10^{19} cm^{-3} obtainable for the TiO_2 sample deposited in the best conditions. At sufficiently high p_{O2} (i.e. O_2 concentration $\geq$ 1000 ppm) the oxygen is thought to be incorporated from the thin film surface, eventually leading to the filling of the $V_O^{\bullet\bullet}$[§] and to the formation of several oxygen-related electron-killer defects (e.g. V_{Ti}'''', O_i''). Thus, the lower amount of *n* in TiO_2 with respect to TaTO before the oxygen incorporation mechanism, results in its more pronounced increment of the electrical resistance.

Finally, it has been reported that TiO_2-based samples UFA crystallized in a nitrogen-based atmosphere with O_2 concentration higher than 20 ppm both show a non-ohmic behavior when measuring the resistance directly from the film surface. On the other hand, the ohmic contact is guaranteed when the *I*/*V* measurements are performed between Ti/Au electrodes previously evaporated on the top of the samples. This evidence is again consistent with oxygen penetration (and associated formation of an insulating layer) limited to the topmost uncovered surface of the thin films, while the metal contacts would act as capping layers, avoiding the oxygen penetration beneath them.

6.3.2 Oxygen incorporation during UFA crystallizations

In order to collect definitive evidences of the oxygen incorporation hypothesized in the previous section, we performed UFA treatments on TaTO samples under nitrogen containing different ^{18}O concentrations. The employment of oxygen isotopes allows to trace the possible oxygen penetration in the film via depth profiling the $^{16}O/^{18}O$ ratio with Secondary Ion Mass Spectrometry, using a commercial TOF-SIMS IV (experiment performed by T. Acartürk at the Max Planck Institute for Solid State Research of

[§] Note that under the adopted synthesis conditions $V_O^{\bullet\bullet}$ should be the only donor defect in undoped TiO_2, see Section 2.3.2.

Stuttgart). The secondary ions were generated by short pulses of a 25 keV Ga ion beam. Removal of material for depth profiling was carried out using a second ion beam from a Cs source operated at 500 eV. The correlation between the secondary ion extraction and depth was established using a Dektak 8 profilometer at the end of the measurement.

N_2-based atmospheres with two different ^{18}O concentrations were employed for this study: 80 ppm and 1000 ppm. Note that the mixture of N_2 with 80 ppm of ^{18}O was used as it was the lowest ^{18}O concentration obtainable with our experimental setup. In Figure 74 *(a)* the *in-situ* electrical measurements acquired for the TaTO films during the UFA cycles in ^{18}O atmospheres are reported (purple and orange for 80 ppm and 1000 ppm respectively); the UFA cycle for the TaTO sample crystallized in 20 ppm O_2 nitrogen-based atmosphere (red) is reported as a reference.

It is possible to observe that, in line with the experimental data previously discussed for TaTO 1000 ppm O_2 UFA (see orange curves in Figure 72), the corresponding concentration of ^{18}O isotopes results in a very similar resistance behavior (orange curves in Figure 74 *(a)*). Consistently, the resulting $R_{T=25°C}$ increases with respect to the UFA treatment in 20 ppm (10 Ω and 6 Ω respectively). Nonetheless, it is possible to note that the increase of oxygen concentration up to 80 ppm (^{18}O isotopic mixture, purple curves in Figure 74 *(a)*) is already enough to slightly affect the obtained room temperature resistance of the TaTO film ($R_{T=25°C}$ = 7 Ω). Also in this case, we confirm the direct connection between the different $R_{T=25°C}$ obtained for oxygen concentrations > 20 ppm and the resistance changes recorded in region-A.

The TOF-SIMS results shown in Figure 74 *(b)* for both the TaTO samples annealed in ^{18}O atmosphere confirm the hypothesis of oxygen incorporation in the samples: this is well described in both the films by an exponential decay of the $^{18}O/^{16}O$ ratio as a function of depth (see the fitting dotted lines in Figure 74 *(b)*). Comparing the 1000 ppm with the 80 ppm ^{18}O profiles it is evident that UFA treatments performed under higher concentrations of oxygen lead to *(i)* deeper ^{18}O penetration and *(ii)* larger ^{18}O concentration in proximity of the TaTO film surface.

It should be pointed out that while entering in the thin film the ^{18}O can move further in depth the forming ^{16}O ions, meaning that an exact determination of the oxidation depth cannot be determined. Nonetheless, it is possible to safely estimate that penetration from the film free surface should be limited to the first tens of nanometers of the thin films (Figure 74 *(b)*).

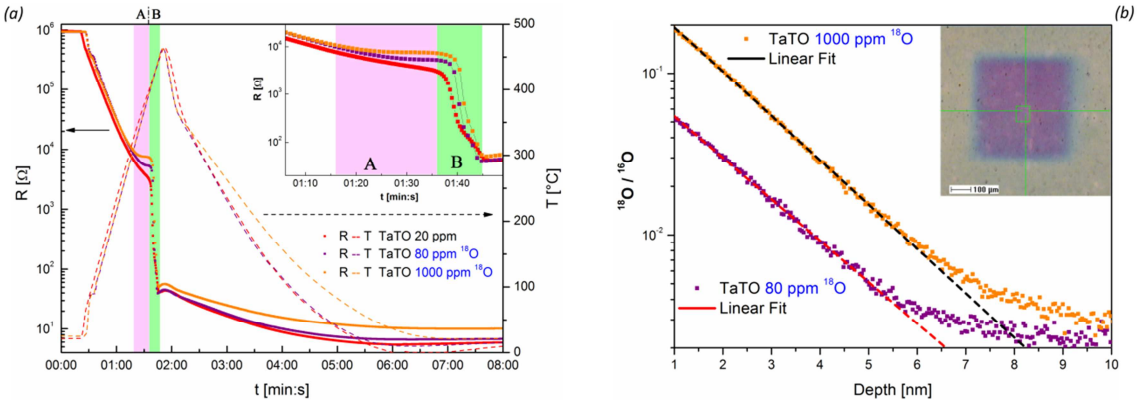

Figure 74 *(a)* In-situ resistance measurements (dots, left y-axes) and corresponding temperature cycles (dashed lines, right y-axes) for TaTO thin films crystallized in N_2-based atmospheres with different ^{18}O concentrations: 80 ppm (purple) and 1000 ppm (orange). TaTO thin film crystallized in N_2-based atmosphere with 20 ppm of oxygen (red) is reported as reference (already present in Figure 68 and Figure 72). The regions A and B (pink and green colored respectively) represent the time intervals in which the resistivity of the thin films starts to be affected by the presence of different oxygen concentrations (A) and in which the abrupt resistance drop takes place (B). In the inset a magnification of the resistance behavior in the regions A and B is reported. *(b)* Depth profile of the $^{18}O/^{16}O$ ratio traced via TOF-SIMS; the colors of the dotted profiles are consistent with those used in *(a);* in the inset is reported an optical microscope acquisition of the analyzed area of a TaTO thin film. Pictures reproduced from [159].

Based on our previous observations, this top-most layer is characterized by a significantly higher resistance due to the severe reduction of the charge carrier density dictated by the oxygen incorporation in the anatase lattice. Nonetheless, the electrical properties of the thin film beneath this superficial layer should be unaffected.

The presence of the insulating top layer corresponding to superficial oxygen penetration was investigated by removing the first tens of nm of an UFA-treated TaTO film in 1000 ppm O_2 by bombardment by Ar ions at 0.2 kV accelerating voltage. The sputtering process was performed at room temperature (total pressure during treatment 5.7×10^{-2} Pa). The correlation between sputtering process time and the removed material was calibrated by SEM images (10 nm removal every 30 min, see Figure 75 *(a)*) and independently confirmed by transmittance measurements (i.e. interspace from interference fringes, not shown). Moreover, cross sectional SEM images acquired for the sample before and after the sputtering processes showed an excellent homogeneity of the removed thickness (Figure 75 *(a)*). Atomic force microscopy (AFM performed in tapping/noncontact mode with a Thermomicroscopes Autoprobe CP II using Veeco RTESPA

tips) topographic images show that the R_{ms} is just slightly increased after the removal of 30 nm (from ~ 2 nm to ~ 2.6 nm, Figure 75 *(b)*).

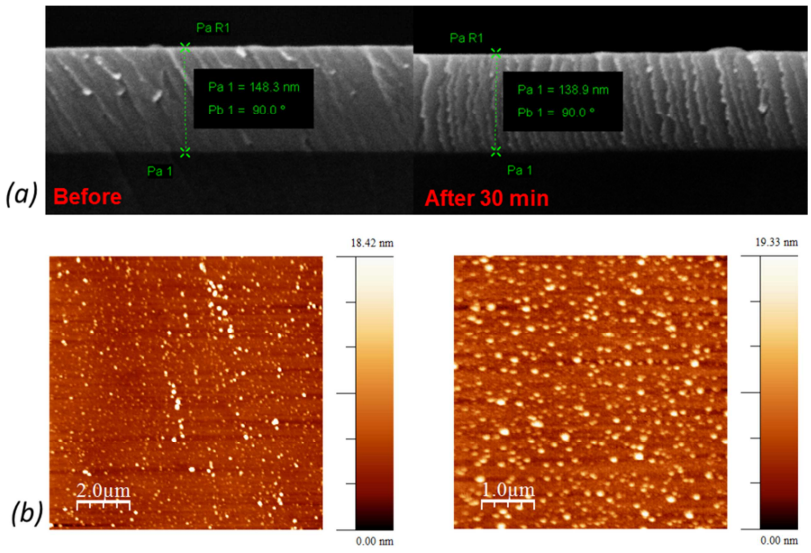

Figure 75 *(a)* SEM cross sectional acquisition of UFA crystallized TaTO sample in 1000 ppm O_2 atmosphere before (left) and after (right) the sputtering removal of 10 nm. In *(b)* are reported the AFM images acquired for the surface of the same sample before (left) and after (rigth) the sputtering removal of 30 nm.

The removal of the top 10 nm of the thin film lead to the recovery of ohmic contact characteristic; the subsequent sputter of the surface results in the conservation of a constant sheet resistance value, and after 30 nm removal the remaining 120 nm thick TaTO film is shown to totally recover the charge carrier density with respect to the same film annealed in UFA 20 ppm ($\rho = 8.76 \times 10^{-4}$ Ωcm, $n = 8.53 \times 10^{20}$ cm^{-3}).

These experiment thus nicely confirms the presence of a thin surface layer characterized by a higher oxygen concentration and resistivity, whose thickness can be controlled by tuning the oxygen concentration in the UFA atmosphere.

Nonetheless, all the experimental evidences shown and discussed in this chapter, as well as in the overall thesis work, are suggesting that the presence of an oxygen incorporation profile should be accompanied by a considerable and coherent (in terms of amount of incorporated oxygen-magnitude of the obtained effect) decrease of the charge carrier density in the TiO_2-based thin films, leading to the detrimental effect on their conductivity.

We note that the obtainment of a TCO with a top layer characterized by a graded, decreasing charge carrier profile as a function of the vicinity to the surface

(whose thickness can be easily and precisely tuned with the UFA process atmosphere) could be exploited as a TCO + selective layer architecture for DSSC or perovskite-based solar cell devices (see Section 2.1). It should be highlighted that this double layer structure can be obtained from a single deposition + annealing process (lasting just 5 minutes in a cheap nitrogen-based atmosphere).

7. Conclusions and perspectives

The evolution of new generation solar cell devices requires the discovery and optimization of novel and more performing solutions in terms of materials and cell architectures (e.g. from dye sensitized to perovskite-based solar cells), but also a perfect match among the several material interfaces which constitute the device. In this framework, the thorough study focused on the control and understanding of the optical and electrical properties of Ta-doped TiO_2 (TaTO) thin films discussed in this thesis work is of particular relevance.

TiO_2 (non-extrinsically doped) is one of the most employed materials in several photovoltaic device architectures; in particular, it represents an efficient and selective bridge for the separation and transport of the photogenerated electrons throughout the anode side of the device. A well suited energy level alignment *(i)* with the photoactive material (which actively generates the electron-hole couples) in the form of an high surface area porous layer (photoanode), and *(ii)* with the front electrode in the form of a compact and continuous film (selective layer) is the basic requirement for the best functioning of the device. Since all the anode side of the cell has to be characterized by a high transmittance to the visible light, the electrode has to combine both transparency and conductivity. For this reason a material in the class of Transparent Conductive Oxides (TCOs) is usually employed. Nonetheless, the most performing TCOs can result in an unfavorable matching of the energy levels with respect to TiO_2, eventually causing a considerable reduction in the overall performances of the photovoltaic device. In 2005, Nb- and Ta-doped TiO_2 (TNO and TaTO respectively) has been proposed as a new class of TCOs. In fact, because of the proven ability to substitute a certain amount

of Ti atoms in the anatase TiO_2 cell with a dopant, it is possible to promote a large amount of electrons in the conduction band, resulting in low electrical resistivity while maintaining a good transmittance. This discovery could potentially open the way to an all TiO_2-based photoelectrode which could be especially advantageous for dye sensitized as well as perovskite-based solar cells not only for a better alignement of the energy levels throughout the device interfaces, but also for the stability and durability of the cell due to the intrinsically high chemical stability of TiO_2-based materials.

Nonetheless, TiO_2-based TCOs still suffer of a considerably lack of knowledge with respect to the most employed TCOs. In particular, between the two possible dopants, Ta is thought to have definitive advantages over Nb for transparent conductive electrode applications. Nevertheless, so far TaTO has been considerably less investigated then TNO especially in the case of thin films obtained on cheap substrates, which is a basic condition to be effectively considered as a suitable candidate for future application (not only in solar cell devices). For this reason in this thesis work I deeply investigated the structure – property relationship of TaTO polycrystalline films deposited on glass. Several open points related to TiO_2-based materials were faced in this study, like for example the strict necessity of a reducing atmosphere in order to obtain highly conducting films.

The synthesis of the investigated TaTO and TiO_2 polycrystalline films was accomplished by room temperature Pulsed Laser Deposition (PLD) on soda-lime glass substrates followed by a thermal annealing treatment in order to crystallize the initially amorphous films in the anatase phase. Taking advantage of the high control and versatility of the PLD technique, I developed the ability to finely control the morphology of the samples by tuning the oxygen background pressure (p_{O2}) during the laser ablation process. In particular, compact (p_{O2} = 1 – 2.5 Pa) as well as hierarchically grown – nano-tree shaped porous films (p_{O2} = 10 – 15 Pa) were obtained with several extrinsic doping concentrations (Ta = 0, 1, 5, 10 at.%).

The best functional properties (resistivity of ~ 5 x 10^{-4} Ωcm for a 150 nm thick film, with a mean transmittance in the visible range exceeding 80%) were obtained for compact TaTO samples (Ta = 5 at.%) deposited at p_{O2} = 1 Pa and subsequently crystallized with a so-called “standard” vacuum annealing at 550°C (ramp 10°C/min, 1 hour dwell, p < 4×10^{-5} Pa). Notably, the possibility to finely tune the electrical properties of TaTO compact thin films after standard vacuum annealing processes was

independently achieved for *(i)* different extrinsic dopant concentrations, and *(ii)* different oxygen partial pressures during the room temperature deposition process while maintaining a fixed Ta-doping level. Noteworthy, the recorded resistivity variations were found to be mainly connected with the charge carrier density, which in both cases could be tuned in a wide range ($n \sim 10^{19} - 10^{21}$ cm^{-3}). It should be highlighted that while for *(i)* this evidence could be reasonably explained with a different amount of substitutional tantalum ($Ta_{Ti}^{\bullet}$) in the lattice, for *(ii)* the observed behavior (given the fixed concentration of $Ta_{Ti}^{\bullet}$) should be ruled by the presence / absence of oxygen vacancies ($V_O^{\bullet\bullet}$) coupled with the formation of *p*-type "electron-killer" defects like titanium vacancies and/or oxygen interstitials ($V_{Ti}^{''''}$, O_i''). The formation of different defects and the presence of a possible interplay among them was found to be strictly related to the oxygen partial pressure during deposition and/or the subsequent annealing process. In the case of the post-deposition thermal treatment it was found that even the presence of some parts per million of oxygen in the annealing atmosphere resulted in the obtainment of insulating films. Moreover, the collected experimental evidences point towards the presence of a different defect chemistry between the donor doped and the undoped TiO_2.

Since it is plausible to assume that the charged defects, which are obviously ruling the functional properties in both the doped and undoped material, should be present in a significant concentration in the anatase cell, a thorough study of the structure – property relationships was done with XRD as well as Raman spectroscopy. A significant trend between the anatase unit cell parameters and the synthesis conditions was found for vacuum annealed TaTO thin films with a fixed doping concentration (Ta = 5 at.%) deposited at slightly different p_{O2}. Moreover, a deep investigation of the position and width of Raman active modes was made on a large amount of TiO_2-based samples, and confirmed that even the vibrational properties of the thin films were strongly affected by *(i)* the presence of dopant in the anatase lattice, and *(ii)* by the different synthesis conditions. In particular, it is noteworthy to mention the solid relationship that was found between the shift of the most intense anatase Raman active mode $E_g(1)$ and the corresponding charge carrier density, independently with respect to the presence of a different extrinsic doping amount (Ta = 0, 1, 5, 10 at.%) or the employed dopant (e.g. Ta or Nb).

Further studies (e.g. Raman spectroscopy at different temperatures or excitation wavelengths, first principle calculations) should be addressed in order to fully understand the physical mechanisms behind these interesting experimental findings.

Furthermore, with the aim of shedding light on the point defects involved in the electrical / structural trends which were previously identified, a Positron Annihilation Spectroscopy study in Coincidence Doppler Broadening (PAS-CDB) was presented. The collected experimental evidences showed that the electrically insulating character in TaTO should be associated to a higher amount of V_{Ti}'''' and a lower amount of $V_O^{\bullet\bullet}$ with respect to the corresponding conducting film. Interestingly, an indication of a strong relationship between the extrinsic dopant and the oxygen vacancies is found and preliminary discussed. The future examination of the collected data for TiO_2 films could provide important evidences of an hypothesized different defect chemistry between the doped and undoped material.

Nonetheless, a possible step further in the direction of a full understanding of the defect chemistry of TiO_2-based materials could be related to the employement of other complementary experimental techniques, like life-time PAS and Extended X-Ray Absorption Fine Structure (EXAFS), whose results combined with the already acquired data in CDB could be fundamental in the univocal determination of the point defects.

Taking advantage of the acquired knowledge on the physical mechanisms behind the functional properties of TiO_2-based films, we also demonstrated the possibility to fully crystallize TiO_2-based films exploiting ultra-fast annealing treatments (UFA) at 460 °C (heating rate 300 °C/min), by monitoring the crystallization threshold of the films via *in-situ* resistance measurements. This process not only reduces the total time (5 minutes vs. 180 minutes for the conventional vacuum heating cycle at 550 °C) and temperature necessary to obtain high quality polycrystalline films, but gives also the possibility to decouple the electrical properties from the influence of the annealing atmosphere during fast crystallization. Remarkably, UFA performed in N_2 (20 ppm of oxygen) yields the same conductivity and transparency of a standard annealing carried out in vacuum (for both doped and undoped TiO_2). Furthermore, complementary experiments (UFA in presence of different oxygen concentrations, Secondary Ion Mass Spectrometry) were performed and permitted to experimentally demonstrate the detrimental role of oxygen incorporation on the charge carrier density for TiO_2-based films and the possibility to obtain a surface layer characterized by lower

n (and thus a gradient of *n* in the film). Taking advantage of the obtained results for ultra-fast annealed TaTO films, it would be possible to obtain a TCO + selective layer from an UFA crystallization of a single homogeneous thin film.

A study on the electrical properties of vertically oriented nanotree-like shaped porous films was also conducted. This high surface area films can be employed as photoanodes, and the possibility to increase the electron conductivity along the vertical direction of these nanostructures is an highly desirable property. Nonetheless, the electrical measurement of these films required unconventional contactless techniques. Experiments employing a synchrotron light source permitted to find that, similarly to what has been found for the compact films, the incorporation of different concentrations of Ta in the anatase matrix resulted in an increased and tunable conductivity of the nanotrees.

It should be noted that this nanotree-shaped TiO_2-based porous structures could be very interesting also in the field of electrochemical or solar water splitting processes, and a future study addressing the possible advantages of controlling dopant and morphology for this application could be appealing.

Finally, combining the acquired knowledge on the synthesis and control of the functional properties of TaTO films in both compact and porous morphologies it was possible to obtain multi-layer structures with the aim of realizing an all TiO_2-based TCO + selective layer + photoanode. This novel solution is currently under testing in new generation photovoltaic devices in the framework of an established collaboration with the research group of A. Abbotto (università Milano Bicocca). These combined structures could be fundamental not only for a mere efficiency improvement of the device, but also for the investigation of the still debated physical mechanisms behind the superior performances of novel perovskite-based solar cell devices.

Bibliography

1. Hagfeldt, A., et al., *Dye-Sensitized Solar Cells.* Chemical Reviews, 2010. **110**(11): p. 6595-6663.
2. Green, M.A., A. Ho-Baillie, and H.J. Snaith, *The emergence of perovskite solar cells.* Nature Photonics, 2014. **8**(7): p. 506-514.
3. Kirchartz, T., et al., *Classification of solar cells according to mechanisms of charge separation and charge collection.* Physical Chemistry Chemical Physics, 2015. **17**(6): p. 4007-4014.
4. Concina, I. and A. Vomiero, *Metal Oxide Semiconductors for Dye- and Quantum-Dot-Sensitized Solar Cells.* Small, 2015. **11**(15): p. 1744-1774.
5. Snaith, H.J. and M. Grätzel, *The Role of a "Schottky Barrier" at an Electron-Collection Electrode in Solid-State Dye-Sensitized Solar Cells.* Advanced Materials, 2006. **18**(14): p. 1910-1914.
6. Furubayashi, Y., et al., *A transparent metal: Nb-doped anatase TiO_2.* Applied Physics Letters, 2005. **86**(25): p. 252101.
7. Hitosugi, T., et al., *Properties of TiO_2-based transparent conducting oxides.* Physica Status Solidi a-Applications and Materials Science, 2010. **207**(7): p. 1529-1537.
8. Ghosh, R., et al., *Increasing Photocurrents in Dye Sensitized Solar Cells with Tantalum-Doped Titanium Oxide Photoanodes Obtained by Laser Ablation.* Acs Applied Materials & Interfaces, 2012. **4**(9): p. 4566-4570.
9. Carotta, M.C., et al., *Nanostructured pure and Nb-doped TiO_2 as thick film gas sensors for environmental monitoring.* Sensors and Actuators B: Chemical, 1999. **58**(1–3): p. 310-317.
10. Das, C., et al., *Nb doped TiO_2 nanotubes for enhanced photoelectrochemical water-splitting.* Nanoscale, 2011. **3**(8): p. 3094-3096.
11. Sauvage, F., et al., *Hierarchical TiO_2 Photoanode for Dye-Sensitized Solar Cells.* Nano Letters, 2010. **10**(7): p. 2562-2567.

12. Hanaor, D.A.H. and C.C. Sorrell, *Review of the anatase to rutile phase transformation.* Journal of Materials Science, 2011. **46**(4): p. 855-874.

13. Landmann, M., E. Rauls, and W.G. Schmidt, *The electronic structure and optical response of rutile, anatase and brookite TiO_2.* Journal of Physics: Condensed Matter, 2012. **24**(19): p. 195503.

14. Weng, Z., et al., *Nanostructured TiO_2 for energy conversion and storage.* RSC Advances, 2013. **3**(47): p. 24758-24775.

15. Luttrell, T., et al., *Why is anatase a better photocatalyst than rutile? - Model studies on epitaxial TiO_2 films.* Scientific Reports, 2014. **4**.

16. Fujishima, A. and K. Honda, *Electrochemical Photolysis of Water at a Semiconductor Electrode.* Nature, 1972. **238**(5358): p. 37-38.

17. Chen, X., L. Liu, and F. Huang, *Black titanium dioxide (TiO_2) nanomaterials.* Chemical Society Reviews, 2015. **44**(7): p. 1861-1885.

18. Kasuga, T., et al., *Formation of Titanium Oxide Nanotube.* Langmuir, 1998. **14**(12): p. 3160-3163.

19. Di Fonzo, F., et al., *Hierarchically organized nanostructured TiO_2 for photocatalysis applications.* Nanotechnology, 2009. **20**(1): p. 015604.

20. Bruce, P.G., B. Scrosati, and J.-M. Tarascon, *Nanomaterials for Rechargeable Lithium Batteries.* Angewandte Chemie International Edition, 2008. **47**(16): p. 2930-2946.

21. Liu, Y., et al., *A TiO_2-nanotube-array-based photocatalytic fuel cell using refractory organic compounds as substrates for electricity generation.* Chemical Communications, 2011. **47**(37): p. 10314-10316.

22. O'Regan, B. and M. Gratzel, *A low-cost, high-efficiency solar cell based on dye-sensitized colloidal TiO_2 films.* Nature, 1991. **353**(6346): p. 737-740.

23. Kojima, A., et al., *Organometal Halide Perovskites as Visible-Light Sensitizers for Photovoltaic Cells.* Journal of the American Chemical Society, 2009. **131**(17): p. 6050-6051.

24. Pekkola, R., *Electronic Structure of Solid-State Dye-Sensitized Solar Cells: Synchrotron Induced Photoelectron Spectroscopy on Nanocrystalline TiO_2, Newly Developed Dyes and Spiro-MeOTAD*, 2014, TU Darmstadt.

25. Snaith, H.J. and L. Schmidt-Mende, *Advances in Liquid-Electrolyte and Solid-State Dye-Sensitized Solar Cells.* Advanced Materials, 2007. **19**(20): p. 3187-3200.

26. Gong, J.W., J. Liang, and K. Sumathy, *Review on dye-sensitized solar cells (DSSCs): Fundamental concepts and novel materials.* Renewable & Sustainable Energy Reviews, 2012. **16**(8): p. 5848-5860.

27. Burschka, J., et al., *Tris(2-(1H-pyrazol-1-yl)pyridine)cobalt(III) as p-Type Dopant for Organic Semiconductors and Its Application in Highly Efficient Solid-State Dye-Sensitized Solar Cells.* Journal of the American Chemical Society, 2011. **133**(45): p. 18042-18045.

28. Kim, H.-S., et al., *Lead Iodide Perovskite Sensitized All-Solid-State Submicron Thin Film Mesoscopic Solar Cell with Efficiency Exceeding 9%.* Scientific Reports, 2012. **2**.

29. Stranks, S.D. and H.J. Snaith, *Metal-halide perovskites for photovoltaic and light-emitting devices.* Nature Nanotechnology, 2015. **10**(5): p. 391-402.

30. Lotsch, B.V., *New Light on an Old Story: Perovskites Go Solar.* Angewandte Chemie International Edition, 2014. **53**(3): p. 635-637.

31. Snaith, H.J., *Perovskites: The Emergence of a New Era for Low-Cost, High-Efficiency Solar Cells.* The Journal of Physical Chemistry Letters, 2013. **4**(21): p. 3623-3630.

32. Kim, H.-S., S.H. Im, and N.-G. Park, *Organolead Halide Perovskite: New Horizons in Solar Cell Research.* The Journal of Physical Chemistry C, 2014. **118**(11): p. 5615-5625.

33. Lee, M.M., et al., *Efficient Hybrid Solar Cells Based on Meso-Superstructured Organometal Halide Perovskites.* Science, 2012. **338**(6107): p. 643-647.

34. Burschka, J., et al., *Sequential deposition as a route to high-performance perovskite-sensitized solar cells.* Nature, 2013. **499**(7458): p. 316-319.

35. Ellmer, K., *Past achievements and future challenges in the development of optically transparent electrodes.* Nature Photonics, 2012. **6**(12): p. 809-817.

36. Klein, A., et al., *Transparent Conducting Oxides for Photovoltaics: Manipulation of Fermi Level, Work Function and Energy Band Alignment.* Materials, 2010. **3**(11): p. 4892.

37. Ritzau, K.-U., et al., *TCO work function related transport losses at the a-Si:H/TCO-contact in SHJ solar cells.* Solar Energy Materials and Solar Cells, 2014. **131**: p. 9-13.

38. Zhang, Z. and J.T. Yates, *Band Bending in Semiconductors: Chemical and Physical Consequences at Surfaces and Interfaces.* Chemical Reviews, 2012. **112**(10): p. 5520-5551.

39. Ashcroft, N.W. and N.D. Mermin, *Solid State Physics*, 1976: Holt, Rinehart and Winston.

40. Turrión, M., J. Bisquert, and P. Salvador, *Flatband Potential of F:SnO_2 in a TiO_2 Dye-Sensitized Solar Cell: An Interference Reflection Study.* The Journal of Physical Chemistry B, 2003. **107**(35): p. 9397-9403.

41. Rühle, S. and T. Dittrich, *Investigation of the Electric Field in TiO_2/FTO Junctions Used in Dye-Sensitized Solar Cells by Photocurrent Transients.* The Journal of Physical Chemistry B, 2005. **109**(19): p. 9522-9526.

42. Wang, J.T.-W., et al., *Low-Temperature Processed Electron Collection Layers of Graphene/TiO_2 Nanocomposites in Thin Film Perovskite Solar Cells.* Nano Letters, 2014. **14**(2): p. 724-730.

43. Zhou, H., et al., *Interface engineering of highly efficient perovskite solar cells.* Science, 2014. **345**(6196): p. 542-546.

44. Minami, T., *Present status of transparent conducting oxide thin-film development for Indium-Tin-Oxide (ITO) substitutes.* Thin Solid Films, 2008. **516**(17): p. 5822-5828.

45. Gondoni, P., et al., *Structural and functional properties of Al:ZnO thin films grown by Pulsed Laser Deposition at room temperature.* Thin Solid Films, 2012. **520**(14): p. 4707-4711.

46. Gondoni, P., et al., *Morphology-driven electrical and optical properties in graded hierarchical transparent conducting Al:ZnO.* MRS Online Proceedings Library, 2014. **1699**.

47. Gondoni, P., et al., *Enhancing light harvesting by hierarchical functionally graded transparent conducting Al-doped ZnO nano- and mesoarchitectures.* Solar Energy Materials and Solar Cells, 2014. **128**(0): p. 248-253.

48. Hosono, H., M. Yasukawa, and H. Kawazoe, *Novel oxide amorphous semiconductors: transparent conducting amorphous oxides.* Journal of Non-Crystalline Solids, 1996. **203**: p. 334-344.

49. Nomura, K., et al., *Room-temperature fabrication of transparent flexible thin-film transistors using amorphous oxide semiconductors.* Nature, 2004. **432**(7016): p. 488-492.

50. Hosono, H., *Transparent Amorphous Oxide Semiconductors for Flexible Electronics*, in *Handbook of Transparent Conductors*, D.S. Ginley, Editor 2011, Springer US. p. 459-487.

51. Hautier, G., et al., *Identification and design principles of low hole effective mass p-type transparent conducting oxides.* Nature Communications, 2013. **4**.

52. Van de Walle, C.G., *Hydrogen as a Cause of Doping in Zinc Oxide.* Physical Review Letters, 2000. **85**(5): p. 1012-1015.

53. Robertson, J. and B. Falabretti, *Electronic Structure of Transparent Conducting Oxides*, in *Handbook of Transparent Conductors*, D.S. Ginley, Editor 2011, Springer US. p. 27-50.

54. Sernelius, B.E., et al., *Band-gap tailoring of ZnO by means of heavy Al doping.* Physical Review B, 1988. **37**(17): p. 10244-10248.

55. Burstein, E., *Anomalous Optical Absorption Limit in InSb.* Physical Review, 1954. **93**(3): p. 632-633.

56. Jain, A., P. Sagar, and R.M. Mehra, *Band gap widening and narrowing in moderately and heavily doped n-ZnO films.* Solid-State Electronics, 2006. **50**(7–8): p. 1420-1424.

57. Abdolahzadeh Ziabari, A. and S.M. Rozati, *Carrier transport and bandgap shift in n-type degenerate ZnO thin films: The effect of band edge nonparabolicity.* Physica B: Condensed Matter, 2012. **407**(23): p. 4512-4517.

58. Coutts, T.J., D.L. Young, and X. Li, *Characterization of Transparent Conducting Oxides.* MRS Bulletin, 2000. **25**(08): p. 58-65.

59. Kohan, A.F., et al., *First-principles study of native point defects in ZnO.* Physical Review B, 2000. **61**(22): p. 15019-15027.

60. Mryasov, O.N. and A.J. Freeman, *Electronic band structure of indium tin oxide and criteria for transparent conducting behavior.* Physical Review B, 2001. **64**(23): p. 233111.

61. Hitosugi, T., et al., *Ta-doped anatase TiO_2 epitaxial film as transparent conducting oxide.* Japanese Journal of Applied Physics Part 2-Letters & Express Letters, 2005. **44**(33-36): p. L1063-L1065.

62. Tachikawa, T., et al., *Metal-to-insulator transition in anatase TiO_2 thin films induced by growth rate modulation.* Applied Physics Letters, 2012. **101**(2): p. 022104.

63. Murakami, M., et al., *Anatase TiO_2 thin films grown on lattice-matched $LaAlO_3$ substrate by laser molecular-beam epitaxy.* Applied Physics Letters, 2001. **78**(18): p. 2664-2666.

64. Guillén, C., J. Montero, and J. Herrero, *Anatase and rutile TiO_2 thin films prepared by reactive DC sputtering at high deposition rates on glass and flexible polyimide substrates.* Journal of Materials Science, 2014. **49**(14): p. 5035-5042.

65. Schuisky, M., et al., *Atomic Layer Chemical Vapor Deposition of TiO_2 Low Temperature Epitaxy of Rutile and Anatase.* Journal of the Electrochemical Society, 2000. **147**(9): p. 3319-3325.

66. Wang, Z., U. Helmersson, and P.-O. Käll, *Optical properties of anatase TiO_2 thin films prepared by aqueous sol–gel process at low temperature.* Thin Solid Films, 2002. **405**(1–2): p. 50-54.

67. Conde-Gallardo, A., et al., *TiO_2 anatase thin films deposited by spray pyrolysis of an aerosol of titanium diisopropoxide.* Thin Solid Films, 2005. **473**(1): p. 68-73.

68. Gillispie, M.A., et al., *rf magnetron sputter deposition of transparent conducting Nb-doped TiO_2 films on $SrTiO_3$.* Journal of Applied Physics, 2007. **101**(3): p. 033125.

69. Hitosugi, T., et al., *Fabrication of TiO_2-based transparent conducting oxide films on glass by pulsed laser deposition.* Japanese Journal of Applied Physics Part 2-Letters & Express Letters, 2007. **46**(1-3): p. L86-L88.

70. Hitosugi, T., et al., *Fabrication of highly conductive $Ti_{1-x}Nb_xO_2$ polycrystalline films on glass substrates via crystallization of amorphous phase grown by pulsed laser deposition.* Applied Physics Letters, 2007. **90**(21): p. 212106.

71. Yamada, N., et al., *Fabrication of low resistivity Nb-doped TIO_2 transparent conductive polycrystalline films on glass by reactive sputtering.* Japanese Journal of Applied Physics, Part 1: Regular Papers and Short Notes and Review Papers, 2007. **46**(8 A): p. 5275-5277.

72. Dabney, M.S., et al., *Pulsed laser deposited Nb doped TiO_2 as a transparent conducting oxide.* Thin Solid Films, 2008. **516**(12): p. 4133-4138.

73. Hitosugi, T., et al., *Transparent conducting properties of anatase $Ti_{0.94}Nb_{0.06}O_2$ polycrystalline films on glass substrate.* Thin Solid Films, 2008. **516**(17): p. 5750-5753.

74. Hoang, N.L.H., et al., *Low-temperature fabrication of transparent conducting anatase Nb-doped TiO_2 films by sputtering.* Applied Physics Express, 2008. **1**(11): p. 1150011-1150013.

75. Yamada, N., et al., *Structural, electrical and optical properties of sputter-deposited Nb-doped TiO_2 (TNO) polycrystalline films.* Thin Solid Films, 2008. **516**(17): p. 5754-5757.

76. Tonooka, K., T.-W. Chiu, and N. Kikuchi, *Preparation of transparent conductive TiO_2:Nb thin films by pulsed laser deposition.* Applied Surface Science, 2009. **255**(24): p. 9695-9698.

77. Yamada, N., et al., *Direct growth of transparent conducting Nb-doped anatase TiO_2 polycrystalline films on glass.* Journal of Applied Physics, 2009. **105**(12): p. 123702.

78. Neubert, M., et al., *Overcoming challenges to the formation of high-quality polycrystalline TiO_2:Ta transparent conducting films by magnetron sputtering.* Journal of Applied Physics, 2013. **114**(8): p. 083707.

79. Wu, B.B., F.M. Pan, and Y.E. Yang, *Annealing Effect of Pulsed Laser Deposited Transparent Conductive Ta-Doped Titanium Oxide Films.* Chinese Physics Letters, 2011. **28**(11): p. 118102.

80. Morgan, B.J. and G.W. Watson, *Intrinsic n-type Defect Formation in TiO_2: A Comparison of Rutile and Anatase from GGA+U Calculations.* The Journal of Physical Chemistry C, 2010. **114**(5): p. 2321-2328.

81. Tang, H., et al., *Electrical and optical properties of TiO_2 anatase thin films.* Journal of Applied Physics, 1994. **75**(4): p. 2042-2047.

82. Kröger, F.A. and H.J. Vink, *Relations between the concentrations of imperfections in solids.* Journal of Physics and Chemistry of Solids, 1958. **5**(3): p. 208-223.

83. Nowotny, J., et al., *Defect Chemistry and Electrical Properties of Titanium Dioxide. 1. Defect Diagrams.* The Journal of Physical Chemistry C, 2007. **112**(2): p. 590-601.

84. Knauth, P. and H.L. Tuller, *Electrical and defect thermodynamic properties of nanocrystalline titanium dioxide.* Journal of Applied Physics, 1999. **85**(2): p. 897-902.

85. Weibel, A., R. Bouchet, and P. Knauth, *Electrical properties and defect chemistry of anatase (TiO_2).* Solid State Ionics, 2006. **177**(3–4): p. 229-236.

86. Janotti, A., et al., *Hybrid functional studies of the oxygen vacancy in TiO_2.* Physical Review B, 2010. **81**(8): p. 085212.

87. Deák, P., B. Aradi, and T. Frauenheim, *Quantitative theory of the oxygen vacancy and carrier self-trapping in bulk TiO_2.* Physical Review B, 2012. **86**(19): p. 195206.

88. Setvin, M., et al., *Direct View at Excess Electrons in TiO_2 Rutile and Anatase.* Physical Review Letters, 2014. **113**(8): p. 086402.

89. Wang, S., et al., *Titanium-Defected Undoped Anatase TiO_2 with p-Type Conductivity, Room-Temperature Ferromagnetism, and Remarkable*

Photocatalytic Performance. Journal of the American Chemical Society, 2015. **137**(8): p. 2975-2983.

90. Zhang, S.X., et al., *Niobium doped TiO_2: Intrinsic transparent metallic anatase versus highly resistive rutile phase.* Journal of Applied Physics, 2007. **102**(1): p. 013701.

91. Nowotny, M.K., et al., *Defect Chemistry of Titanium Dioxide. Application of Defect Engineering in Processing of TiO_2-Based Photocatalysts.* The Journal of Physical Chemistry C, 2008. **112**(14): p. 5275-5300.

92. Barman, A.R., et al., *Multifunctional $Ti_{1-x}Ta_xO_2$: Ta doping or alloying?* Applied Physics Letters, 2011. **98**(7): p. 072111.

93. Hitosugi, T., et al., *Electronic band structure of transparent conductor: Nb-doped anatase TiO_2.* Applied Physics Express, 2008. **1**(11): p. 1112031-1112033.

94. Morris, D., et al., *Photoemission and STM study of the electronic structure of Nb-doped TiO_2.* Physical Review B, 2000. **61**(20): p. 13445-13457.

95. Deák, P., B. Aradi, and T. Frauenheim, *Polaronic effects in TiO_2 calculated by the HSE06 hybrid functional: Dopant passivation by carrier self-trapping.* Physical Review B, 2011. **83**(15): p. 155207.

96. Yamamoto, T. and T. Ohno, *Screened hybrid density functional study on Nb- and Ta-doped TiO_2.* Physical Review B, 2012. **85**(3): p. 033104.

97. Huy, H.A., et al., *Comparison of Nb- and Ta-doping of anatase TiO_2 for transparent conductor applications.* Journal of Applied Physics, 2012. **112**(1): p. 016103.

98. Osorio-Guillén, J., S. Lany, and A. Zunger, *Atomic Control of Conductivity Versus Ferromagnetism in Wide-Gap Oxides Via Selective Doping: V, Nb, Ta in Anatase TiO_2.* Physical Review Letters, 2008. **100**(3): p. 036601.

99. Rusydi, A., et al., *Cationic-vacancy-induced room-temperature ferromagnetism in transparent, conducting anatase $Ti_{1-x}Ta_xO_2$ (x~0.05) thin films.* Philosophical Transactions of the Royal Society A: Mathematical, Physical and Engineering Sciences, 2012. **370**(1977): p. 4927-4943.

100. Gondoni, P., et al., *Structure-dependent optical and electrical transport properties of nanostructured Al-doped ZnO.* Nanotechnology, 2012. **23**(36): p. 365706.

101. Huy, H.A., et al., *Calculation of carrier-concentration-dependent effective mass in Nb-doped anatase crystals of TiO_2.* Physical Review B, 2011. **83**(15): p. 155201.

102. Yamada, N., et al., *Enhanced Carrier Transport in Uniaxially (001)-Oriented Anatase $Ti_{0.94}Nb_{0.06}O_2$ Films Grown on Nanosheet Seed Layers.* Applied Physics Express, 2011. **4**(4): p. 045801.

103. Liu, X., X. Wu, and K. Scott, *Study of niobium and tantalum doped titania-supported Pt electrocatalysts for methanol oxidation and oxygen reduction reactions.* Catalysis Science & Technology, 2014. **4**(11): p. 3891-3898.

104. Lee, S., et al., *Nb-Doped TiO_2: A New Compact Layer Material for TiO_2 Dye-Sensitized Solar Cells.* The Journal of Physical Chemistry C, 2009. **113**(16): p. 6878-6882.

105. Yin, X., et al., *Performance enhancement of perovskite-sensitized mesoscopic solar cells using Nb-doped TiO_2 compact layer.* Nano Research, 2015. **8**(6): p. 1997-2003.

106. Chandiran, A.K., et al., *Doping a TiO_2 Photoanode with Nb^{5+} to Enhance Transparency and Charge Collection Efficiency in Dye-Sensitized Solar Cells.* Journal of Physical Chemistry C, 2010. **114**(37): p. 15849-15856.

107. Lü, X., et al., *Improved-Performance Dye-Sensitized Solar Cells Using Nb-Doped TiO_2 Electrodes: Efficient Electron Injection and Transfer.* Advanced Functional Materials, 2010. **20**(3): p. 509-515.

108. Hara, Y., et al., *Controlled Seeding of Laser Deposited Ta:TiO_2 Nanobrushes and Their Performance as Photoanode for Dye Sensitized Solar Cells.* Acs Applied Materials & Interfaces, 2013. **5**(24): p. 13140-13145.

109. Eason, R., *Pulsed laser deposition of thin films: applications-led growth of functional materials*, 2007: Wiley-Interscience.

110. Casari, C.S. and A. Li Bassi, *Pulsed Laser Deposition of Nanostructured Oxides: From Clusters to Functional Films* in *Advances in Laser and Optics Research*, W.T. Arkin, Editor 2012, Nova Science Publishers. p. 65-100.

111. Willmott, P.R. and J.R. Huber, *Pulsed laser vaporization and deposition.* Reviews of Modern Physics, 2000. **72**(1): p. 315-328.

112. Passoni, L., et al., *Hyperbranched quasi-1d nanostructures for solid-state dye-sensitized solar cells.* ACS Nano, 2013. **7**(11): p. 10023-10031.

113. Vold, M.J., *A numerical approach to the problem of sediment volume.* Journal of Colloid Science, 1959. **14**(2): p. 168-174.

114. Sutherland, D.N., *Comments on Vold's simulation of floc formation.* Journal of Colloid and Interface Science, 1966. **22**(3): p. 300-302.

115. Gerosa, M. and C.E. Bottani, *Multiple light scattering and near-field effects in a fractal treelike ensemble of dielectric nanoparticles.* Physical Review B, 2013. **87**(19): p. 195312.

116. Mazzolini, P., et al., *Tuning of Electrical and Optical Properties of Highly Conducting and Transparent Ta-Doped TiO_2 Polycrystalline Films.* The Journal of Physical Chemistry C, 2015. **119**(13): p. 6988-6997.

117. Balachandran, U. and N.G. Eror, *Raman spectra of titanium dioxide.* Journal of Solid State Chemistry, 1982. **42**(3): p. 276-282.

118. Li Bassi, A., et al., *Raman spectroscopy characterization of titania nanoparticles produced by flame pyrolysis: The influence of size and stoichiometry.* Journal of Applied Physics, 2005. **98**(7): p. 074305.

119. Gondoni, P., *Nanostructured Transparent Conducting Oxides for Advanced Photovoltaic Applications*, 2014, Politecnico di Milano.

120. Van der Pauw, L.J., *A method of measuring specific resistivity and Hall effect of discs of arbitrary shape.* Philips Research Reports, 1958. **13**: p. 1-9.

121. Tauc, J., *Optical properties and electronic structure of amorphous Ge and Si.* Materials Research Bulletin, 1968. **3**(1): p. 37-46.

122. Wooten, F., *Optical properties in solids,* 1972, New York, NY: Academic Press.

123. Buchholz, D.B., et al., *Control and Characterization of the Structural, Electrical, and Optical Properties of Amorphous Zinc−Indium−Tin Oxide Thin Films.* Acs Applied Materials & Interfaces, 2009. **1**(10): p. 2147-2153.

124. Oliver, P.M., et al., *Atomistic simulation of the surface structure of the TiO_2 polymorphs rutileand anatase.* Journal of Materials Chemistry, 1997. **7**(3): p. 563-568.

125. Yang, C., et al., *c-axis-oriented growth of anatase TiO_2 thin films on glass substrate with $SrTiO_3$/TiN template.* Journal of Crystal Growth, 2013. **376**(0): p. 66-69.

126. Dy, E., et al., *Electronic Conductivity and Stability of Doped Titania ($Ti_{1-X}M_XO_2$, M = Nb, Ru, and Ta)—A Density Functional Theory-Based Comparison.* The Journal of Physical Chemistry C, 2010. **114**(31): p. 13162-13167.

127. Pore, V., et al., *Explosive Crystallization in Atomic Layer Deposited Mixed Titanium Oxides.* Crystal Growth & Design, 2009. **9**(7): p. 2974-2978.

128. Brudnik, A., et al., *Plasma-emission-controlled d.c. magnetron sputtering of TiO_{2-x} thin films.* Thin Solid Films, 1991. **199**(1): p. 45-58.

129. Poelman, H., et al., *Effect of the oxygen deficiency of ceramic TiO_{2-x} targets on the deposition of TiO_2 thin films by DC magnetron sputtering.* Surface and Interface Analysis, 2004. **36**(8): p. 1167-1170.

130. Gondoni, P., et al., *Tuning electrical properties of hierarchically assembled Al-doped ZnO nanoforests by room temperature Pulsed Laser Deposition.* Thin Solid Films, 2015. **594**: p. 12-17.

131. Jabeen, F., et al., *Contactless monitoring of the diameter-dependent conductivity of GaAs nanowires.* Nano Research, 2010. **3**(10): p. 706-713.

132. Chrastina, D., *Private communication,* 14/02/2014.

133. Shannon, R., *Revised effective ionic radii and systematic studies of interatomic distances in halides and chalcogenides.* Acta Crystallographica Section A, 1976. **32**(5): p. 751-767.

134. Kamisaka, H., et al., *Density functional theory based first-principle calculation of Nb-doped anatase TiO_2 and its interactions with oxygen vacancies and interstitial oxygen.* Journal of Chemical Physics, 2009. **131**(3): p. 034702.

135. Qi, D.C., et al., *Cationic vacancies and anomalous spectral-weight transfer in $Ti_{1-x}Ta_xO_2$ thin films studied via polarization-dependent near-edge x-ray absorption fine structure spectroscopy.* Physical Review B, 2013. **87**(24): p. 245201.

136. Mikami, M., et al., *Lattice dynamics and dielectric properties of TiO_2 anatase: A first-principles study.* Physical Review B, 2002. **66**(15): p. 155213.

137. Ohsaka, T., F. Izumi, and Y. Fujiki, *Raman spectrum of anatase, TiO_2.* Journal of Raman Spectroscopy, 1978. **7**(6): p. 321-324.

138. Parker, J.C. and R.W. Siegel, *Calibration of the Raman spectrum to the oxygen stoichiometry of nanophase TiO_2.* Applied Physics Letters, 1990. **57**(9): p. 943-945.

139. Mazza, T., et al., *Raman spectroscopy characterization of TiO_2 rutile nanocrystals.* Physical Review B, 2007. **75**(4): p. 045416.

140. Ruiz, A.M., et al., *Insights into the Structural and Chemical Modifications of Nb Additive on TiO_2 Nanoparticles.* Chemistry of Materials, 2004. **16**(5): p. 862-871.

141. Ščepanovica, M., et al., *Characterization of La-doped TiO_2 nanopowders by Raman spectroscopy.* Acta Physica Polonica A, 2009. **115**(4): p. 771 - 774.

142. Alhomoudi, I.A. and G. Newaz, *Residual stresses and Raman shift relation in anatase TiO_2 thin film.* Thin Solid Films, 2009. **517**(15): p. 4372-4378.

143. Hearne, G.R., et al., *Effect of grain size on structural transitions in anatase TiO_2: A Raman spectroscopy study at high pressure.* Physical Review B, 2004. **70**(13): p. 134102.

144. Bersani, D., P.P. Lottici, and X.-Z. Ding, *Phonon confinement effects in the Raman scattering by TiO_2 nanocrystals.* Applied Physics Letters, 1998. **72**(1): p. 73-75.

145. Barborini, E., et al., *Engineering the nanocrystalline structure of TiO_2 films by aerodynamically filtered cluster deposition.* Applied Physics Letters, 2002. **81**(16): p. 3052-3054.

146. Kavan, L., et al., *Oxygen-isotope labeled titania: $Ti^{18}O_2$.* Physical Chemistry Chemical Physics, 2011. **13**(24): p. 11583-11586.

147. Frank, O., et al., *Raman spectra of titanium dioxide (anatase, rutile) with identified oxygen isotopes (16, 17, 18).* Physical Chemistry Chemical Physics, 2012. **14**(42): p. 14567-14572.

148. Dupasquier, A., G. Kögel, and A. Somoza, *Studies of light alloys by positron annihilation techniques.* Acta Materialia, 2004. **52**(16): p. 4707-4726.

149. Ferragut, R.O., *Personal communication.* 06/10/2014.

150. Tuomisto, F. and I. Makkonen, *Defect identification in semiconductors with positron annihilation: Experiment and theory.* Reviews of Modern Physics, 2013. **85**(4): p. 1583-1631.

151. Uedono, A., et al. *Defect characterization of crystalline metal oxides and high-k films by means of positron annihilation*. in *Solid-State and Integrated Circuit Technology (ICSICT), 2010 10th IEEE International Conference on*. 2010.

152. Veen, A.v., et al., *Analysis of positron profiling data by means of ''VEPFIT''.* AIP Conference Proceedings, 1991. **218**(1): p. 171-198.

153. Sreetama, D., et al., *Defects and the optical absorption in nanocrystalline ZnO.* Journal of Physics: Condensed Matter, 2007. **19**(23): p. 236218.

154. Qin, X.B., et al., *Vacancy identification in Co^+ doped rutile TiO_2 crystal with positron annihilation spectroscopy.* Journal of Physics: Conference Series, 2011. **262**(1): p. 012051.

155. Ferragut, R., et al., *Defect Characterization in SiGe/SOI Epitaxial Semiconductors by Positron Annihilation.* Nanoscale Research Letters, 2010. **5**(12): p. 1942-1947.

156. Uedono, A., et al., *Vacancy-type defects in $BaTiO_3$ / $SrTiO_3$ structures probed by monoenergetic positron beams.* Journal of Applied Physics, 2002. **91**(8): p. 5307-5312.

157. Ferragut, R., et al., *Study of defects in an electroresistive $Au/La_{2/3}Sr_{1/3}MnO_3/SrTiO_3(001)$ heterostructure by positron annihilation.* Journal of Applied Physics, 2011. **110**(5): p. 053511.

158. Okazaki, S., et al., *Fabrication of Nb-Doped TiO_2 Transparent Conducting Films by Postdeposition Annealing under Nitrogen Atmosphere.* Japanese Journal of Applied Physics, 2012. **51**(11R): p. 118003.

159. Mazzolini, P., et al., *Controlling the Electrical Properties of Undoped and Ta-doped TiO_2 Polycrystalline Films via Ultra-Fast Annealing Treatments.* Advanced Electronic Materials, 2015, forthcoming.

160. Leichtweiss, T., et al., *Amorphous and highly nonstoichiometric titania (TiO_x) thin films close to metal-like conductivity.* Journal of Materials Chemistry A, 2014. **2**(18): p. 6631-6640.

161. Yang, C., et al., *Metal-induced solid-phase crystallization of amorphous TiO_2 thin films.* Applied Physics Letters, 2012. **101**(5): p. 052101.

162. Park, J.H., et al., *Highly Transparent, Low Resistance, and Cost-Efficient $Nb:TiO_2/Ag/Nb:TiO_2$ Multilayer Electrode Prepared at Room Temperature Using Black $Nb:TiO_2$ Target.* Electrochemical and Solid State Letters, 2010. **13**(5): p. J53-J56.

163. Hoang, N.L.H., et al., *Crystallization Kinetics of Amorphous Sputtered Nb-Doped TiO_2 Thin Films.* Applied Physics Express, 2011. **4**(10): p. 105601.

164. Park, J.-H., et al., *Indium-free, acid-resistant anatase Nb-doped TiO_2 electrodes activated by rapid-thermal annealing for cost-effective organic photovoltaics.* Solar Energy Materials and Solar Cells, 2011. **95**(8): p. 2178-2185.